

Mathematical and computational modeling of metallic biomaterials biodegradation

Mojtaba Barzegari

June 2023

Contents

| | |
|---|-----------|
| 1 General introduction | 4 |
| 1.1 Biodegradable metals | 4 |
| 1.2 Magnesium as a biodegradable material | 6 |
| 1.3 Chemistry of biodegradation of magnesium | 8 |
| 1.4 Computational modeling of biodegradation | 12 |
| 2 Aims and objectives | 15 |
| 2.1 General aim | 15 |
| 2.2 Specific objectives | 16 |
| 2.3 Thesis outline | 18 |
| 3 Developing the core computational model | 20 |
| 3.1 Introduction | 20 |
| 3.1.1 Magnesium biodegradation | 20 |
| 3.1.2 Computational modeling of Mg degradation | 21 |
| 3.2 Background theory | 23 |
| 3.2.1 Biodegradation as a reaction-diffusion system | 23 |
| 3.2.2 Moving boundary - Stefan problems | 24 |
| 3.2.3 Level-set method | 24 |
| 3.3 Materials and methods | 25 |
| 3.3.1 Underlying chemistry | 25 |
| 3.3.2 Mathematical modeling | 26 |
| 3.3.3 Interface movement formulation | 28 |
| 3.3.4 Boundary conditions | 28 |
| 3.3.5 Implementation | 29 |
| 3.3.6 Experimental setup | 31 |
| 3.3.7 Parameter estimation | 31 |
| 3.3.8 Simulation setup | 33 |
| 3.3.9 Case study | 35 |
| 3.4 Results | 35 |
| 3.4.1 Optimization results | 35 |

| | | |
|----------|---|-----------|
| 3.4.2 | Degradation prediction | 36 |
| 3.4.3 | Example application | 37 |
| 3.5 | Discussion | 38 |
| 3.6 | Conclusions | 43 |
| 4 | Extending the model: adding fluid flow and convection | 44 |
| 4.1 | Introduction | 44 |
| 4.2 | Methods | 46 |
| 4.2.1 | Navier-Stokes equations | 46 |
| 4.2.2 | Weak formulation of the Navier-Stokes equations | 47 |
| 4.2.3 | Stokes equations | 48 |
| 4.2.4 | Implementation | 49 |
| 4.2.5 | Preconditioning and parallelizing the computation | 51 |
| 4.2.6 | Considering the degrading object | 52 |
| 4.2.7 | Simulation setup | 53 |
| 4.3 | Results | 55 |
| 4.4 | Discussion | 57 |
| 4.5 | Conclusion | 60 |
| 5 | Extending the model: simulating local pH evolution | 64 |
| 5.1 | Introduction | 64 |
| 5.2 | Methods | 67 |
| 5.2.1 | Experimental setup | 67 |
| 5.2.2 | Computational model construction | 68 |
| 5.2.3 | Simulation setup | 73 |
| 5.3 | Results | 74 |
| 5.3.1 | Thermodynamics-based simulation | 74 |
| 5.3.2 | Biodegradation simulations | 74 |
| 5.4 | Discussion | 75 |
| 5.5 | Conclusion | 78 |
| 6 | Computational modeling of the neotissue growth process | 84 |
| 6.1 | Introduction | 84 |
| 6.2 | Deriving the model | 86 |
| 6.2.1 | General equation of interface motion | 86 |
| 6.2.2 | Phase-field formulation | 87 |
| 6.2.3 | Level-set formulation | 88 |
| 6.3 | Dimensionless forms for various cases | 88 |
| 6.3.1 | Stationary interface | 88 |
| 6.3.2 | Evolution under constant normal speed | 89 |
| 6.3.3 | Curvature-driven interface evolution | 90 |

| | | |
|----------|---|------------|
| 6.4 | Adapting the formulation for curvature-driven tissue growth | 90 |
| 6.5 | Numerical implementation | 92 |
| 6.5.1 | Phase-field model | 92 |
| 6.5.2 | Level-set model | 93 |
| 6.6 | Simulation setup | 94 |
| 6.7 | Results and discussion | 95 |
| 6.8 | Challenges in coupling tissue growth and biodegradation models | 102 |
| 6.9 | Conclusion | 105 |
| 7 | Model parallelization for high-performance computing | 106 |
| 7.1 | Introduction | 106 |
| 7.2 | Background theory and model description | 109 |
| 7.2.1 | Chemistry of degradation | 110 |
| 7.2.2 | Reaction-diffusion equation | 110 |
| 7.2.3 | Level-set method | 112 |
| 7.3 | Methodology of model implementation | 113 |
| 7.3.1 | Finite element discretization | 114 |
| 7.3.2 | Implementation and parallelization | 118 |
| 7.3.3 | Level-set issues | 121 |
| 7.3.4 | Simulation setup | 122 |
| 7.3.5 | Performance analysis | 123 |
| 7.3.6 | Compute environment | 125 |
| 7.4 | Results | 125 |
| 7.4.1 | Numerical simulation results | 125 |
| 7.4.2 | Weak and strong scaling results | 126 |
| 7.5 | Discussion | 127 |
| 7.6 | Conclusion | 131 |
| | Appendix 7.A Comparing different preconditioners and solvers . | 132 |

Chapter 1

General introduction

Biodegradable (bioabsorbable) implants provide temporary support for tissues, where the implants completely dissolve and are absorbed by the body during or after tissue healing, avoiding several drawbacks of permanent implants [1]. The application of biodegradable metallic biomaterials [2–4], including magnesium [5–7], zinc [8, 9], and iron [10], has become more prominent for over a decade in various biomedical engineering and tissue engineering disciplines. Among the mentioned materials, magnesium (Mg) is the most studied metal [11], the reason for which is its suitable mechanical and chemical properties for biomedical applications. Although poor corrosion resistance of Mg is a limiting factor for its application as light structural material, like in the transportation industry, it becomes an interesting characteristic when it comes to the biodegradable materials field for cardiovascular and orthopedic applications [12–14]. The first clinical usage of Mg was reported in 1878, but a renewed interest in it has grown significantly in the last 15–20 years [11]. From the clinical and biomedical perspective, two major concerns about using Mg in clinics are the release of hydrogen gas and surface alkalization due to Mg dissolution [15]. These issues are commonly addressed by alloying, biocompatible coating and surface modification [11]. This chapter includes an overview of biodegradable materials with a focus on Mg, the history of their usage in medical applications, a description of the chemistry of Mg biodegradation, and various computational models aiming to capture this chemistry.

1.1 Biodegradable metals

It has been a very long time since metals have started being employed as implant materials to support, reinforce, repair, or replace damaged tissues

and organs. Historically speaking, iron dental implants were discovered in the remains of a European who perished at the end of the first century AD or the start of the second century [16]. Moreover, gold has been used for the same application in China since ancient times. With more development in materials science and engineering, inert materials such as titanium alloys, cobalt alloys, and stainless steel are widely used nowadays in biomedical implants and devices. However, there are certain drawbacks to these materials in medical applications:

- The release of metallic ions from implants fabricated with these materials can lead to various side effects in the surrounding tissues such as inflammation.
- In some cases, such as for temporary fixation in cardiovascular and orthopedics applications, implant presence is unnecessary after the healing process. Moreover, removing the implant via a secondary surgery may not be a practical solution, causing suffering and pain to the patient again.
- The difference between the elastic modulus of these materials and the surrounding tissues can lead to various mechanical integrity issues. For instance, in the case of bone, this difference causes stress shielding effect, where the implant acts as a shield preventing the bone from receiving enough mechanical load needed for bone remodeling and growth. Additionally, this may cause further mechanical loosening of the implant and secondary bone fracture.

Biodegradable implants would be a great solution to the issues mentioned above. Implants fabricated from biodegradable materials gradually disappear and get absorbed by the body. With more attention to employing these materials in clinical applications, more research studies were conducted to investigate their various aspects. Initially, degradable polymers (such as polylactic acid) were used for this purpose, but later studies showed that they might stimulate the aseptic inflammation of surrounding tissues [1]. Besides, the mechanical properties of polymer materials are not acceptable in load-bearing applications. As a result, biodegradable metals gained more attention in orthopedics where Mg is the most suitable candidate due to its elastic modulus (41-45 GPa) being closest to that of natural bone (2-30 GPa) [17]. In addition to this, especially for bone healing applications, the released metallic ions during the degradation process contribute to the metabolism of the underlying biological process. For example, Mg is one of the most abundant ions found in the bone, and Mg cations have a beneficial impact on

the metabolism of enzymes in the bone regeneration process. Similarly, iron (Fe) plays a key role in oxygen transport in the body, and zinc (Zn) positively influences the physiological functions of bone healing and the formation of different transcriptional factors [18–22].

1.2 Magnesium as a biodegradable material

From the corrosion science perspective, Mg is an active material with a relatively low standard electrode potential of -2.37V , meaning that Mg and its alloys have high corrosion/degradation rate [1]. This property makes Mg and Mg-based alloys a biodegradable metal in biomedical applications, where the materials undergo corrosion in biological and physiological conditions and disappear during or after the damaged tissue is repaired.

From the biological perspective, Mg can contribute positively to the human body's metabolism to improve health. A normal adult body contains 20 – 28g of Mg, from which 27% is distributed in muscles, 65% in bone, and the rest in blood and other tissues [23]. Additionally, Mg contributes to more than 300 enzyme reactions in the body [24]. Extra Mg not needed by the body metabolism is transported via the circulatory system and excreted through the bladder, without causing any major side effect [17].

The first application of Mg for biomedical purposes was recorded in 1878 by Hues, who made artificial radial arteries from Mg and suggested that Mg can be beneficial for the treatment of ovariectomy and hemorrhoids [1]. Payr performed successful animal experiments using Mg tubular vascular connectors in 1900, after which the vessels were reformed, and vascular thickness returned to its normal range after 16 days of implantation [25]. This started a wide range of usage of Mg for cardiovascular applications, a recent example of which is the work by Ikeo et al. for designing V-shaped vascular clips made of Mg-Zn-Ca alloy [26]. In this work, the ductility of Mg was reported to be an added advantage for bearing large plastic deformations that these clips experience. In a relevant study, Erbel et al. implanted 71 stents made of Mg alloys in the coronary arteries of 63 patients. The results showed a similar efficiency and safety for Mg stents to that of other metallic stents [27]. Moreover, Mg stents degraded without any problem after four months. This type of study resulted in acquiring the CE mark for the next generation of Mg stents in Europe [28, 29].

The history of usage of Mg in orthopedics applications started very similarly to its vascular applications. In the study by Payr mentioned above, he also stated that Mg can improve the bone healing rate [25]. Six years later, in 1906, the first Mg-based implant was used by Lambotte for fixation

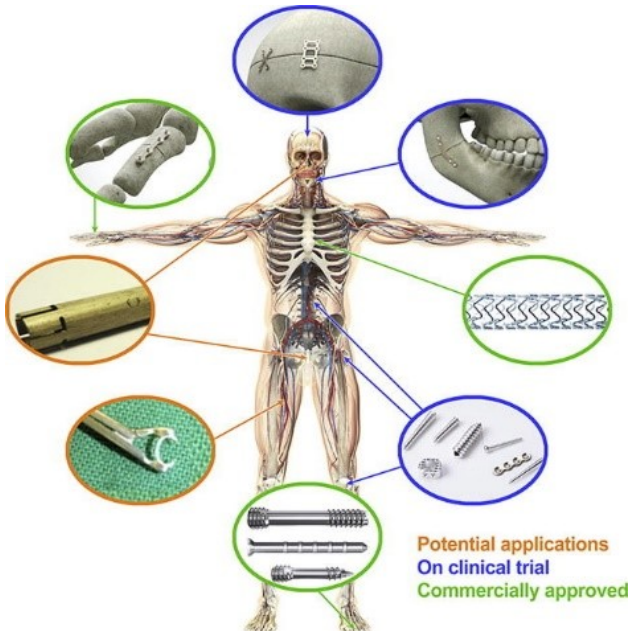


Figure 1.1: Various potential applications of Mg as a biodegradable metallic biomaterial for cardiovascular and orthopedic implants and devices [4].

of a fracture case [30, 31]. This study was followed by many other studies in the last century, the results of which confirmed that Mg could facilitate the bone healing process. However, these studies also demonstrated that the hydrogen gas released during the biodegradation of Mg could lead to inflammation. Furthermore, since Mg's rate of degradation is high, the tissues may not receive enough support before the implants vanish [25]. These issues made the Mg-based implants less common compared to inert metals for orthopedics applications. But, in recent decades, these implants gained more attention thanks to enormous research studies on the biodegradation of Mg to control its side effects and degradation behavior. In 2005, the possibility of using Mg for orthopedics implants was proposed by Witte et al. [32], a suggestion supported by the results of animal studies on femoral implants manufactured from Mg alloys (AZ31, AZ91, WE43, and LAE442). After this study, a wide variety of research works were conducted to investigate the efficiency of Mg-based implants for orthopedics applications [5, 33, 34]. Fig. 1.1 shows the current usage of Mg-based implants and medical devices divided into three categories: commercially approved, on clinical trials, and potential applications [4].

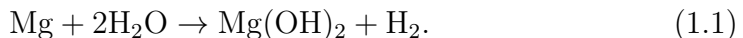
1.3 Chemistry of biodegradation of magnesium

The biodegradation behavior of Mg is investigated in corrosion tests, in which the selection of the corrosive media plays an important role since it affects the underlying chemical reactions [35]. By considering the main application of the biomaterial, which can be tissue engineering scaffolds, vascular stents, or orthopedic fixation devices, the corrosive media can be selected to be a representative of the service environment. The most basic form of the medium is a saline (NaCl) solution, in which the degradation rate is the highest possible [35]. More complex solutions can be used to mimic the behavior of the body environment by taking into account more body fluid components, the most popular of which are Ringer's solution, PBS (phosphate buffered saline), SBFs (simulated body fluids), HBSS (Hank's balanced salt solution), and Earle's balanced salt solution (EBSS) [35]. Adding more organic components to the solution will prepare it to simulate cell culture conditions. The common media for this purpose are MEM (Minimum Essential medium) and DMEM (Dulbecco's modified Eagle's medium) [35]. Fig. 1.2 summarizes various commonly used corrosive media for testing biodegradable metals along with their main components [35].

Various studies have already investigated the effect of different components in the aforementioned corrosive media on the degradation behavior of Mg materials [36–40]. In addition to the presented chemical components, it has been shown that synthetic pH buffers (such as Tris and HEPES) contribute to the biodegradation rate of Mg [36]. The investigations on the effect of different inorganic components, including carbonate, phosphate, sulfate and calcium, show these components' effective contribution to the degradation rate. However, the corrosion protection resulting from the mutual effect of carbonate, phosphate and calcium has been emphasized more [36, 39].

The most common solution for performing corrosion tests on Mg is saline (NaCl) solution, in which the material undergoes aggressive corrosion due to higher electrochemical activities [41, 42]. In a typical aqueous solution, the major corrosion reactions occurring can be written as detailed below [43, 44].

Main, hydrogen evolution reaction (HER):



Secondary, oxygen reduction reaction (ORR):



In this situation, the corrosion products forming on the corroded surface of Mg consist mainly of Mg(OH)_2 and MgO , and the pH in regions close to

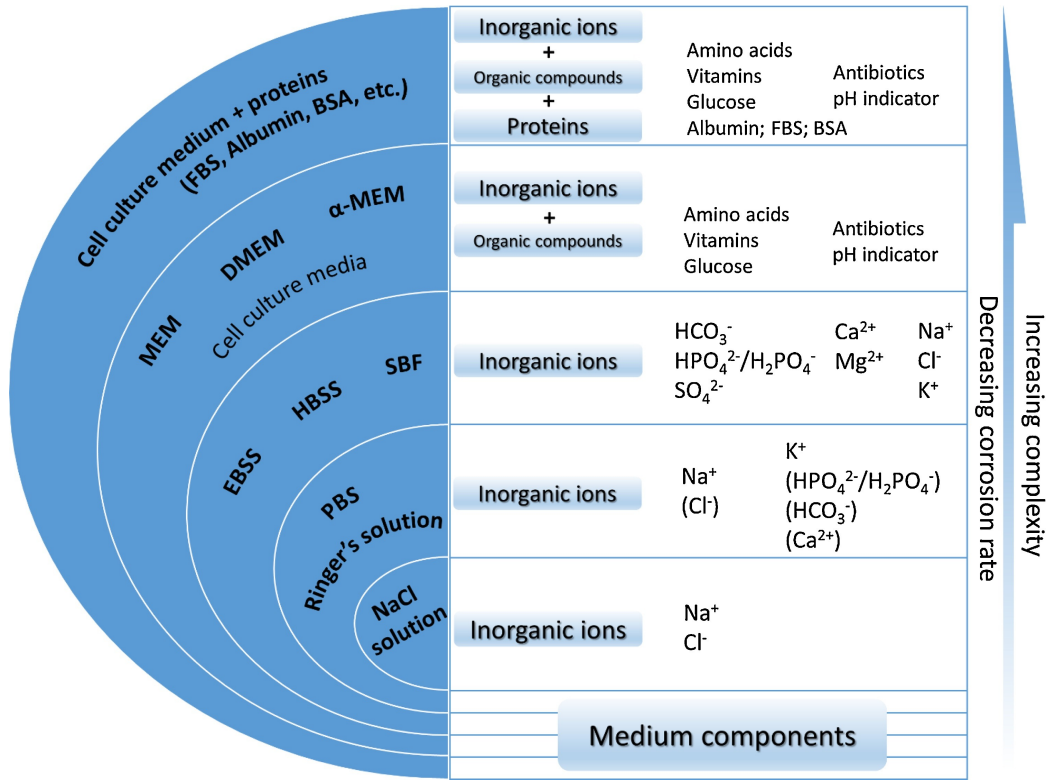
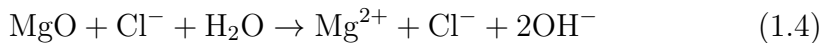
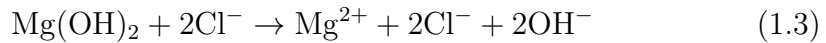


Figure 1.2: A schematic representation of commonly used corrosive media for testing biodegradable metals, sorted by their complexity from the chemical perspective from bottom to top [35].

this surface remains alkaline. In the presence of chloride ions in the saline medium, the formed corrosion product may be broken or bypassed, leading to an increased degradation rate.



The main advantage of using a saline solution for corrosion tests compared to more complex media is that the absence of inorganic ions like carbonate, phosphate, sulfate and calcium allows for investigating the corrosion behavior without concerning possible effect caused by the interaction of these chemical components. On the other hand, the main weakness of saline solution is that it cannot represent the complexity of real body fluid, and as a result, a more complex medium is required to investigate such conditions. To address this issue, more complex saline solutions, such as PBS, are widely used

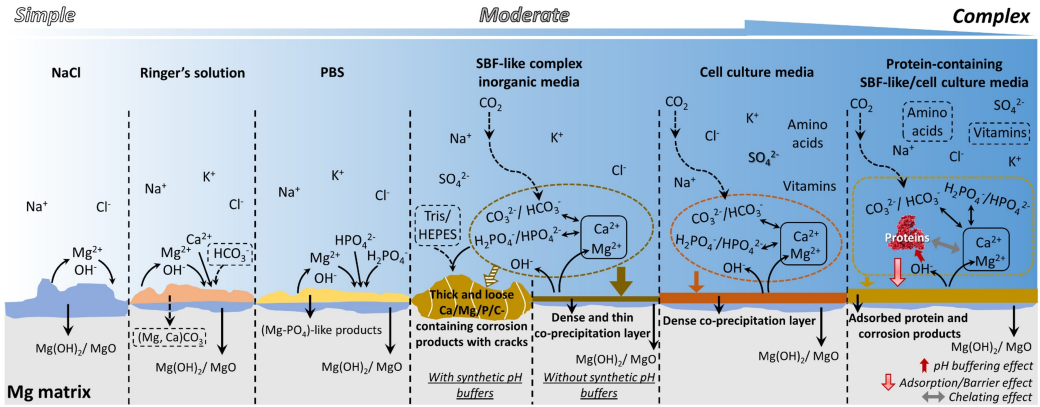


Figure 1.3: A schematic representation of Mg biodegradation behavior in commonly used solutions for corrosion tests of biodegradable metals [35].

for assessing the applicability of Mg alloys in more complex conditions from the chemical perspective [45, 46]. Despite the mentioned limitations, corrosion tests in saline solution are still contributing to understanding intrinsic degradation properties of Mg.

The term "simulated body fluid" is generally used to refer to solutions containing inorganic ions of human serum and interstitial fluid [35]. The commonly used corrosive media in this regard are SBF, HBSS, and EBSS, which all include the same inorganic components yet with a slight difference in their concentrations. A typical composition of these media is chloride, carbonate, phosphates, sulfate and calcium. The individual effect of these components on the rate of degradation of Mg has been extensively studied, where it has been observed that carbonate and phosphate slow down the rate whereas the effect of sulfate is negligible [38, 40]. The concentration of HCO_3^- affects the pH buffering capacity and the degradation rate of Mg simultaneously [47]. The effect of calcium ions is more complex because it does not contribute to Mg corrosion directly. Fig. 1.3 briefly summarizes the various reactions and formed precipitation compositions of the mentioned media for testing the degradation behavior of Mg [35].

There are various evaluation techniques for measuring the degradation rate of Mg, among which the weight loss, hydrogen evolution, potentiodynamic polarization, and electrochemical impedance spectroscopy are the commonly used ones. Generally speaking, the method used for evaluating the degradation rate can affect the reported behavior. For example, it has been shown that in HBSS, the measured corrosion rate of Mg is lower (slower) when evaluated using hydrogen evolution in comparison to the rate found by

direct weight loss measurements [48, 49], which can be due to the secondary dissolution of evolved hydrogen. Moreover, oxygen consumption due to secondary ORR can affect the volume of evolved gas, which is more significant for media with slower degradation rates such as HBSS and MEM [33]. Table 1.1 summarizes the advantages and shortcomings of widely used techniques for measuring degradation rate [35].

Discussing the degradation rate of Mg-based materials can be tricky because as mentioned before, the measurement method and the employed solution can influence the measured degradation rate [50]. However, certain studies have performed this quantitative measurement using different representative media for *in vivo* conditions, resulting in different reported values. The corrosion rate for pure Mg in EBSS was reported to be $0.39 \text{ mm.year}^{-1}$ [51], but in SBF and HBSS, the reported values are 1.39 [52] and $2.05 \text{ mm.year}^{-1}$ [53], respectively. Alloying Mg and adding Ca-P coating seems to decrease the degradation rate to $0.25 \text{ mm.year}^{-1}$ in HBSS [54] and $1.88 \text{ mm.year}^{-1}$ in SBF [55], although no direct correlation between alloying compounds and the degradation rate has been found yet [56].

Table 1.1: Summary of various common methods to assess the degradation rate of Mg [35]

| Test method | Advantages | Shortcomings |
|--|--|--|
| Weight loss | High reliability Direct measurement Easily controlled test environment | Non-continuous. Does not reveal varying corrosion rate throughout the immersion Low sensitivity at the initial stages |
| Hydrogen evolution | Continuous Can be automated Can be performed in closed eu-dimeters | Performed in open environment in most cases Might show underestimated values of corrosion rate due to secondary ORR and solubility of H_2 in aqueous media |
| Potentiodynamic polarization | Fast measurement | Non-continuous Open environment measurement in most cases Very often low correlation with long-term weight loss measurements |
| Electrochemical impedance spectroscopy | Continuous In situ investigation of protective properties of forming corrosion products | Performed in open environments in most cases |

1.4 Computational modeling of biodegradation¹

Besides experimental approaches to investigate the properties of biodegradable metallic implants and scaffolds, computational modeling of the biodegradation process and behavior can be used as an efficient tool to design the next generation of medical devices and implants [57]. In addition to traditional modeling approaches for mechanics of materials, it is possible to take advantage of well-developed principles of modeling transport phenomena and numerical simulations to investigate the biodegradation process computationally [58].

Computational models of the biodegradation process vary from a basic implementation of the process to comprehensive mathematical models that capture multiple aspects of the degradation phenomenon. In the category of simplified corrosion models, Gao et al. performed a quantitative study on the change of mechanics during the biodegradation of Mg alloys for cardiovascular applications [59]. Liu et al. developed a fluid dynamics model to characterize the effect of the induced wall shear stress (WSS) on the biodegradation mechanism of Mg stents [60]. They investigated the effect of blood flow velocity and dynamic environment on the degradation of cardiovascular stents. Boland et al. studied the mechanical performance of Mg stents for the treatment of coronary artery diseases using a computational model [61]. Gartzke et al. proposed a degradation model for the corrosion of Mg alloys coupled with mechanical analysis, allowing them to study the change of mechanical properties during the biodegradation process [62]. Another common category of studies in this regard is continuous damage (CD) simulations, in which geometrical discontinuities get translated into the reduction of materials. Despite the limitation of this technique for modeling biodegradation, such as more focus on the mechanical integrity rather than on the fundamental phenomena, it has been used for various relevant studies, such as Gastaldi et al. [63] and Shi et al. [64].

Among the relevant studies, mass transfer-related models were more successful in representing the biodegradation process mathematically. Indeed, the approach of constructing models based on the well-formulated transport phenomena equations and then solving the derived equations using appropri-

¹This section is partially based on a manuscript prepared to be submitted:
S. Mukherjee, S. Mandal, M. Barzegari, F. Perez-Boerema, B. Liang, E. Sadeghian Dekhord, L. Groeneveldt, L. Geris, “In silico design and optimization of mesoscopic and macroscopic properties of additively manufactured scaffolds: applications in skeletal tissue engineering.”

ate numerical schemes has been followed in recent years to study biodegradation. Ahmed et al. derived a set of mathematical equations to capture the chemical reactions occurring in Mg degradation [65], in which the detailed mathematical equations provided a proper insight into the effect of different chemical components on the biodegradation of Mg *in vitro*. Grogan et al. developed a model to correlate the mass flux of the metallic ions in the biodegradation interface to the velocity of the interface, used to simulate the degradation of complex geometries of Mg-based stents [66]. Similarly, Shen et al. developed a theoretical model to predict the degradation behavior of Mg alloys in orthopedic implants [67]. Their 3D model had a high agreement with *in vitro* corrosion test results.

One of the important applications of biodegradation models is to investigate the change of shape and morphology of the implants and medical devices over time. To this end, appropriate interface capturing methods should be used to track the corrosion interface during the biodegradation process. Bajger et al. developed a mathematical model to study the degradation of Mg implants by reaction-diffusion equations and level-set method (LSM), which enabled them to track the geometrical changes of the implant during degradation [68]. Similarly, Sanz-Herrera et al. developed a comprehensive computational model as a tool for Mg implant design [69]. They combined multiple diffusion-reaction equations to study the change of concentration of the chemical components that play an essential role in *in vitro* biodegradation of Mg implants. A summary of the studies mentioned above is represented in Table 1.2. The reader is encouraged to refer to [70] for a more complete list of recent published mechanistic and phenomenological models of the biodegradation process of Mg-based implants.

The approach taken by Bajger et al. was followed in the current thesis, in which an improved model was developed by considering more chemical components and phenomena, allowing us to perform a more accurate validation using *in vitro* data. Although the biodegradation models are getting more mature and more promising for simulating experimental situations, their integration into other models, such as mechanical stability analysis or neotissue growth, to construct fully-coupled models has remained a challenge. Solving this challenge will enable future models to replicate complex *in vivo* conditions more accurately *in silico*.

Table 1.2: Summary of the recently-developed computational models of the degradation process of Mg-based biomaterials and some of their key characteristics. FEM: Finite Element Method; CFD: Computational Fluid Dynamics; FVM: Finite Volume Method; MOL: Method of Lines; FSI: Fluid-Structure Interaction; ALE: Arbitrary Lagrangian-Eulerian.

| Biological system | Modeled device | Material | Basis of degradation | Software used | Modeling method | Ref |
|-------------------|---------------------|---|--|-------------------|------------------------------------|------|
| Artery | Vascular stent | Mg Alloy AZ31B | Surface corrosion | ABAQUS | FEM, UMAT | [59] |
| Artery | Vascular stent | Mg Alloy WE43 | Surface corrosion | ANSYS Fluent | CFD, FSI, FVM | [60] |
| Remodeling artery | Vascular stent | Mg Alloy AZ31 | Uniform and pitting corrosion | ABAQUS | FEM, USDFLD | [61] |
| Artery | Coronary stents | Mg alloys AZ31, AZ61, AZ80, ZK60 and ZM21 | Surface and stress corrosion | ABAQUS | CD, FEM | [63] |
| Bone | Orthopedic implants | Pure Mg | Surface corrosion by considering biphasic layers | MATLAB | Mass transfer, MOL | [65] |
| Artery | Vascular stent | Mg Alloy AZ31 | Surface corrosion | ABAQUS | Diffusion model, ALE, FEM | [66] |
| Bone | Orthopedic pins | Mg alloys Mg-1Ca and Mg-3Ge | Surface corrosion | ABAQUS | Diffusion model, FEM | [67] |
| Hip bone | Orthopedic implant | Pure Mg | Surface corrosion | In-house, FreeFEM | Reaction-diffusion model, LSM, FEM | [68] |
| Bone | Orthopedic screws | Mg alloy | Surface corrosion | In-house | Reaction-diffusion model, FEM | [69] |
| Bone | Porous scaffolds | Mg Alloy LAE442 | Surface corrosion | ABAQUS | FEM, UMAT | [62] |
| Artery | Vascular stent | Mg Alloy AZ31 | Surface corrosion | ABAQUS | CD, FEM, UMAT | [64] |

Chapter 2

Aims and objectives

This chapter is dedicated to the elaboration of the objectives of the current thesis. It starts with the general definition of the doctoral project aims. Hereafter, the specific objectives of the doctoral project are demonstrated. Then, the chapter illustrates the thesis's outline and structure.

2.1 General aim

The use of biodegradable metals has been gaining attention for various kinds of biomedical applications in recent decades, however, controlling their functionality and behavior inside the body has remained a challenge. Computational modeling of the materials' interaction with the body can help avoid part of the expensive experimental works required to characterize the degradation properties and can provide an integrated spatiotemporal view of the whole process.

One of the most challenging parts of performing such a modeling study is to capture the chemical interactions and the dynamics and kinetics of the reactions occurring on the material-environment interface. Taking advantage of mechanistic modeling principles of mass transfer coupled with free boundary and moving interface formulations seems to be a promising solution to this complex problem. By doing so, one can model the degradation process by a set of equations capturing the interaction of various chemical components while tracking the moving corrosion front, which changes the location where the dynamic is taking place.

In this study, we have developed a mathematical and computational model to predict the biodegradation behavior of biodegradable metallic biomaterials, focusing on Mg. This model enables us to investigate the chemical and, later on, biological phenomena occurring on the corrosion interface of

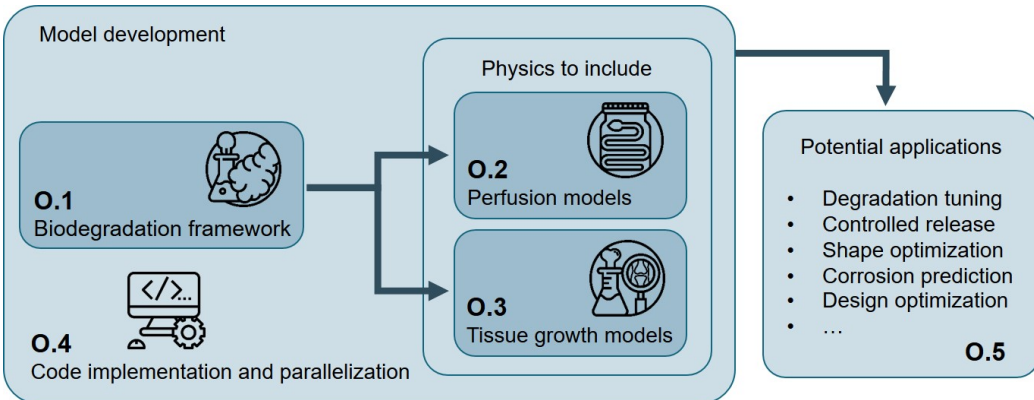


Figure 2.1: Schematic representation of the structure and outline of the current project, divided into five objectives.

these biomaterials. Additionally, coupling the model with other existing cell and tissue growth models leads to a multiphysics model combining the chemistry of biodegradation, the physics of the electrolytes and body fluids flow, and the biology of tissue growth/regeneration. Building such a model requires dealing with several challenges, one of which is to couple various functions used to track the moving boundary of different sub-problems. Moreover, adding the effect of convection imposed by the fluid flow increases the system's complexity. Elaborating these challenges from a mathematical point of view will facilitate future contributions to constructing such models.

2.2 Specific objectives

Despite the advantages of using biodegradable metals in implant design, their fast degradation and uncontrolled release remain a challenge in practical applications. A validated computational model of the degradation process can facilitate the tuning of biodegradation properties. In this doctoral project, a physicochemical model was developed by deriving a mathematical model of the chemistry of biodegradation of Mg and implementing its 3D computational model using the finite element method. To accomplish this, the project was divided into five main objectives, illustrated schematically in Fig. 2.1.

Objective 1 was with the development of the core biodegradation model. For this purpose, a physicochemical model of the biodegradation process of commercially-pure Mg was developed by constructing a mathematical model formulating the mass transfer phenomena and tracking the location of the implant's surface during degradation. For the mass transfer model, a set

of time-dependent reaction-diffusion-convection partial differential equations were derived from the chemistry of biodegradation of the Mg in saline (NaCl) and buffered (SBF) solutions, which usually includes the oxidation of the metallic part, reduction of water and oxygen, changes in local and global pH, and formation of a protective film on the surface of the scaffold which contributes to a slower rate of degradation. Besides these aspects, it was also crucial to consider the effect of different ions in the medium on the degradation rate. Additionally, investigating the structural changes of the scaffolds and implants in practical applications like the resorption of temporary fixation devices, requires tracking the movement of the corrosion surface. This was done by constructing an equation based on the level-set principle, which captured the movement of the medium-metal interface by defining an implicit surface. The derived equations were coupled and solved using the finite element method. The degradation data to validate the models were collected from immersion tests. The model parameters were calibrated using a Bayesian optimization algorithm, and the obtained parameters were used to simulate the pH changes in NaCl and SBF solutions.

Objective 2 was the coupling of corresponding equations of fluid flow (Navier-Stokes and Stokes equations) in the solution domain with the biodegradation model to capture the effect of convection on the degradation process. This was crucial in order to consider the conditions in perfusion bioreactors and hydrodynamics experiments. The main challenge for this step was the complexity of dealing with the finite element formulation of fluid flow equations and the difficulty of defining proper fluid boundary conditions on an implicit interface (the corrosion front).

The **third objective** was to couple the degradation model with the tissue growth models to simulate the response of the surrounding tissue during the biodegradation process. For doing this, a detailed tissue growth model was developed using two different interface tracking techniques, the phase-field and level-set methods, and the results and efficiency of both methods were compared. The mathematical coupling of the degradation and tissue growth models and validating their predictions remained a challenge in this objective.

The **fourth objective** was related to the optimization of the computational aspects of the thesis with all the codes developed in-house using open-source tools and libraries. Detailed work on the parallelization of the computational models of the three previous objectives was carried out to make the developed models run faster. As the required high accuracy on the moving interface increases computation time, parallelization was crucial for the computational models to decrease the execution time of the simulations. The parallel algorithm was implemented using a domain decomposition method. Besides this, the formed linear system of equations in each parti-

tion of the mesh was solved using Krylov methods by taking advantage of available highly efficient preconditioners and iterative solvers, and the scaling behavior with respect to the available computational resources was measured for different components of the models.

The **fifth objective** was the demonstration of the versatility of the developed model by using it as the biodegradation compartment in several multiphysics use-cases to demonstrate the ability of the model to be integrated into other modeling workflows for biomedical applications. In the performed studies, the biodegradation model was combined with structural mechanics and topology optimization codes to deliver a more comprehensive model of the underlying phenomena. The case studies presented in this thesis include mechanical loosening of mandibular bone plates, degradation of an optimized acetabular cup implant, and mechanical integrity of infilled structures.

2.3 Thesis outline

The objectives mentioned in Section 2.2 are tackled in the chapters ahead in the following order and structure:

Chapters 3 and 5 describe the development of the core biodegradation model of **Objective 1**. In **Chapter 3**, a basic biodegradation model is described, which is the base for combining the model with more physics in different applications. **Chapter 5** further develops the base model to include more advanced chemistry from the biodegradation of Mg in more complex electrolytes and conditions.

Chapter 4 describes the development of the fluid flow model used for the simulation of hydrodynamics conditions, which is related to **Objective 2** for coupling the biodegradation model with flow problems. The output coupled model is later used in **Chapter 5** for validating the biodegradation model in hydrodynamics conditions.

The work presented in **Chapter 6** is related to **Objective 3**, in which a tissue growth model is developed to be coupled with the biodegradation model. A simplified tissue growth model is also developed and used in **Chapter ??**, where the rate of bone healing is modeled during the degradation of a mandibular plate, leading to loss of mechanical strength.

Works related to **Objective 4** are presented in **Chapters 7, ??, and ??**, in which the details of software development and model parallelization are elaborated. **Chapter 7** discusses the steps and details of parallelization of the implemented biodegradation model, which can be generalized as a free boundary problem coupled with reaction-diffusion systems. As part of this objective, the developed biodegradation model was transformed into a

multifunctional 3D code called BioDeg, the details of which are described in **Chapter ??**. Additionally, the workflow and routines used to calibrate the models and estimate the unknown parameters are presented in **Chapter ??**, which were also published as educational materials. Furthermore, some parallel scaling behavior results and discussion of the biodegradation model are presented in **Chapter ??**.

In the end, **Chapters ??, ??, and ??** are related to **Objective 5**, dedicated to demonstrating some of the applications of the developed biodegradation model. **Chapter ??** presents the work done to combine the degradation model with the output of a surrogate model, in which the degradation behavior of a patient-specific porous acetabular implant was investigated. **Chapter ??** describes the coupling of the degradation model with a topology optimization code, in which the change of stiffness of some infilled structures was modeled during the degradation process. Lastly, in **Chapter ??**, the biodegradation model was used to predict the rate of mass loss for a mandibular plate, which was subsequently converted to a mechanical strength analysis model to examine how the plate characteristics react to degradation.

To facilitate the structure of the thesis, the chapters related to **Objectives one to three** are grouped in **Part 2** “Model Development”, the chapters related to **Objective 4** are presented in **Part 3** “Code Implementation and Software Development”, and the chapters related to **Objective 5** are presented in **Part 4** “Model Applications”.

Chapter 3

Developing the core computational model

This chapter is based on previously published content in *Corrosion Science*:

M. Barzegari, D. Mei, S. V. Lamaka, and L. Geris, “Computational modeling of degradation process of biodegradable magnesium biomaterials,” *Corrosion Science*, vol. 190, p. 109674, 2021.

Despite the advantages of using biodegradable metals in implant design, their uncontrolled degradation and release remain a challenge in practical applications. A validated computational model of the degradation process can facilitate tuning implant biodegradation properties. In this study, a mathematical model of the chemistry of magnesium biodegradation was developed and implemented in a 3D computational model. The parameters were calibrated by Bayesian optimization using dedicated experimental data. The model was validated by comparing the predicted and experimentally obtained pH change in saline and buffered solutions, showing maximum 5% of difference, demonstrating the model’s validity to be used for practical cases.

3.1 Introduction

3.1.1 Magnesium biodegradation

Due to their bio-friendly properties, biodegradable metallic biomaterials, including magnesium (Mg), iron (Fe), and zinc (Zn), are regaining attention in recent years [2]. These biomaterials find important applications in the design and manufacturing of supportive implants such as temporary devices in or-

thopedics and the cardiovascular field [5, 71]. In orthopedics, the biodegradable metallic biomaterials are used as fixation devices, providing adequate support in the early stages while being absorbed gradually during the bone healing process [72]. Implants fabricated using Mg and its alloys are being used for such a purpose [73] due to the similarity of the stiffness between natural bone and Mg, which helps to reduce the stress shielding induced by the implanted device. Additionally, Mg is reported to have a non-toxic contribution to the human body's metabolism and the bone healing process, which makes the release and absorption of metallic ions safe and biocompatible [74].

Accumulation of mechanistic understanding of Mg degradation achieved by experimental approaches over the years gradually provided a mechanistic understanding of the biodegradation process. Combining these insights with *in silico* modeling approaches enables researchers to study the biodegradation properties and behavior of the implant in a virtual environment prior to conducting any *in vitro* or *in vivo* tests. When fully validated, computational modeling can (in part) replace certain stages of costly and time-consuming experiments verifying the expected degradation behavior of the designed implants. Additionally, the developed models can be efficiently combined with existing computational models to examine other related phenomena such as tissue growth or mechanical integrity.

3.1.2 Computational modeling of Mg degradation

Previous contributions to the computational modeling of the degradation process include a wide range of different approaches, from the basic phenomenological implementations to comprehensive mechanistic models that take into account various aspects of the degradation and resorption process.

Continuous damage (CD) modeling has always been a common approach for corrosion simulation, but from a physicochemical point of view, it focuses on the mechanical integrity of the degradation and neglects the diffusion process. As a result, its application in the degradation modeling of biomaterials, which includes various fundamental phenomena such as mass transfer through diffusion and reaction, is relatively limited. Despite this issue, a CD model proposed by Gastaldi et al. showed a good performance for simulation of bioresorbable Mg-based medical devices [63], in which geometrical discontinuities were interpreted as the reduction of material.

Alternatively, mathematical modeling using transport phenomena equations has shown great flexibility in capturing different mechanisms involved in the biodegradation process. As an example, in Ahmed et al., a set of mathematical equations in cylindrical and spherical coordinates was derived to model the chemical reactions of Mg degradation [65]. Despite the simplic-

ity of their approach from the computational perspective, their model was able to demonstrate the contribution of various chemical components to the *in vitro* degradation of Mg. Similarly, Grogan et al. developed a mathematical model based on the Stefan problem formulation in 1D space to correlate the mass flux of metallic ions into the solution to the velocity of shrinkage of the material during degradation [66]. This was done by considering the mass diffusion and change of the concentration of Mg²⁺ ions, and then, employing an arbitrary Eulerian-Lagrangian (ALE) approach to extend the model to 3D on an adaptive mesh. A similar approach was taken by Shen et al. to develop a theoretical model of the degradation behavior of Mg-based orthopedic implants showing great consistency with *in vitro* test results [67].

An ultimate application of the computational modeling of the biodegradation process of biomaterials can be the prediction of how biodegradation affects the shape of the bulk material, medical device, or implant over time. One of the ways to achieve such a prediction is to capture the movement of the corrosion front mathematically using an appropriate method. The level set method (LSM) is a widely used example in this regard, which is an implicit mathematical way of representing the moving interfaces. This approach was used in Wilder et al. to study galvanic corrosion of metals [75]. They employed LSM on an adaptive mesh to track the moving corrosion interface, but their model lacked a thorough validation using experimental data. Gartzke et al. also worked on a simplified representation of the interface movement by developing a mechanochemical model of the biodegradation process, which helped them to study the effect of degradation on the mechanical properties [62]. They performed a basic qualitative validation on the predictions made by the model. Another similar study in this regard is the Sun et al. work [76], in which a detailed mathematical model was derived and validated to study the deposition of corrosion products on the surface of materials. This mathematical approach was also employed in the biomedical field by Bajger et al. to study the mass loss of Mg biomaterials during biodegradation [68]. They used LSM as well as a set of reaction-diffusion equations to track the change of geometry, which can be directly correlated to the loss of material. The derived equations were also able to capture the formation of the corrosion film that decreases the rate of degradation. Another comprehensive mathematical model was developed by Sanz-Herreraa et al. to investigate the role of multiple chemical components involved in the *in vitro* degradation of Mg implants [69]. One important drawback of this study was its 2D nature. Although the computational model was capable of studying the effect of multiple components, due to the high number of derived equations, it would be difficult to extend and use the same model for real 3D implants. Additionally, a 2D model cannot capture the full phe-

nomenon of corrosion, and as a result, the validation of the model will be more qualitative. It was shown in the study conducted by Gao et al. [59], where they compared the results of a multi-dimension model of the degradation of cardiovascular stents with those of a single-dimension model, that the number of considered dimensions had an important effect on the model predictions. In the end, it is worth mentioning that no dedicated experiments were performed in the aforementioned studies to validate the constructed mathematical and computational models.

The current study focuses on developing a physicochemical model of the biodegradation process of commercially-pure (CP) Mg biomaterials by continuing the work of Bajger et al. [68]. In this model, a set of partial differential equations (PDE) was derived according to the underlying chemistry of biodegradation, described as reaction-diffusion processes taking place at the interface of the biomaterial and its surrounding environment. The formation of a protective layer, effects of the ions in the solution, and the change in the pH due to the corrosion phenomenon were taken into account in the mathematical model. The corresponding computational model was implemented in a fully parallelized manner. Model calibration and validation were executed using data obtained from the immersion tests performed in saline (NaCl) and simulated body fluid (SBF) solutions.

3.2 Background theory

3.2.1 Biodegradation as a reaction-diffusion system

The biodegradation process can be considered as a reaction-diffusion system [77], in which the ions are released due to the chemical reactions on the surface, and the released ions diffuse through the surrounding solution and materials. These ions can interact with other ions and form new compounds [35]. As the reaction-diffusion systems have been studied in science and engineering for a couple of decades, the analogy with a reaction-diffusion system makes it convenient to construct a mathematical model of the biodegradation process based on the well-established transport phenomena equations [78]. From the mathematical perspective, a reaction-diffusion system is expressed by a set of parabolic PDEs that describe the conservation of contributing chemical species in the studied system.

3.2.2 Moving boundary - Stefan problems

Moving boundary problems, also called Stefan problems, are the general class of mathematical problems in which the boundary of the domain should also be calculated in addition to the solution of the other equations [79]. Coupling the reaction-diffusion system of biodegradation with a moving boundary problem constructs a mathematical model in which the change of the domain geometry due to the material loss can be correlated to the underlying reaction and diffusion processes of corrosion. As the geometry can be determined accurately, this approach provides a way to measure the mass loss directly by computing the change in the volume of the material. In such a system, the moving boundary is the material-solution interface (corrosion front).

For a 1D corrosion diffusion system, the position of the diffusion interface can be determined by [79]:

$$s(t) = s_0 + 2\alpha\sqrt{t}, \quad (3.1)$$

in which the $s(t)$ represents the position at any given time, and s_0 is the initial interface position. α coefficient can be calculated using:

$$\alpha = \frac{[Mg]_0 - [Mg]_{sat}}{[Mg]_{sol} - [Mg]_{sat}} \sqrt{\frac{D}{\pi}} \frac{\exp\left(\frac{-\alpha^2}{D}\right)}{\operatorname{erfc}\left(\frac{-\alpha}{\sqrt{D}}\right)} \quad (3.2)$$

where $[Mg]_{sol}$ is the concentration in the solid bulk (i.e. materials density) and $[Mg]_{sat}$ is the concentration at which the material is released to the medium. $[Mg]_0$ represents the initial concentration of the metallic ions in the medium, which is usually zero for most corrosion cases.

Eqs. 3.1 and 3.2 can be used to simply track the movement of the corrosion front, which is the employed method in studies like the Gorgan et al. work [66], but apparently, the real-world corrosion problems are 3D and much more complex than the described system.

As will be described later, Eq. 3.1 is used strictly for the first time step of the simulations in low diffusion regimes for calculating the initial velocity of the interface. Generally speaking, a more sophisticated approach, such as the level set method, is required for tracking the interface of complex 3D geometries.

3.2.3 Level-set method

In the current study, the corrosion front is tracked using an implicit function such that the zero iso-contour of the function represents the metal-solution

interface. As a common practice, this implicit function is expressed as a signed distance function that defines the distance of each point of space (the domain of interest) to the interface. Such a definition implies that the zero iso-contour of the function belongs to the interface. The level set method provides an equation to declare such an implicit function, $\phi = \phi(\mathbf{x}, t)$, $\mathbf{x} \in \Omega \subset \mathbb{R}^3$, which can be obtained by solving [80]:

$$\frac{\partial \phi}{\partial t} + \vec{V^E} \cdot \nabla \phi + V^N |\nabla \phi| = b\kappa |\nabla \phi| \quad (3.3)$$

in which $\vec{V^E}$ is the external velocity field, and V^N is the value of the normal interface velocity. The last term is related to the curvature-dependent interface movement and is omitted. As the effect of perfusion is neglected in the current study, the term containing the external velocity is also eliminated, resulting in the following simplified form of the level set equation:

$$\frac{\partial \phi}{\partial t} + V^N |\nabla \phi| = 0. \quad (3.4)$$

By having the normal velocity of the interface (V^N) at each point and solving Eq. 3.4, the interface can be captured at the zero iso-contour of the ϕ function.

3.3 Materials and methods

3.3.1 Underlying chemistry

The chemistry of biodegradation of Mg depends considerably on the surrounding solution and the presence of certain ions [35]. In NaCl solutions, the anodic and cathodic reactions as well as the formation and elimination of side corrosion products can be considered as follows [2]:



Reaction 3.6 is not fully correct from the chemical point of view. In fact, Mg surface is always covered by MgO layer, and Mg(OH)₂ forms on top of that either at atmospheric conditions or during the immersion. The integrity of this MgO layer is undermined by Cl⁻ ions, leading to an increase in degradation rate:



Although Cl^- formally does not participate in reaction 3.7, it reflects the dependence of Mg corrosion rate on Cl^- concentration. This effect on the rate of degradation has been widely expressed as the effect of Cl^- on the Mg(OH)_2 in the literature [2, 5]. In the developed model, this effect is used interchangeably by omitting the MgO component, so the protective film formed on the corrosion interface is assumed to contain Mg(OH)_2 only. Moreover, it has been shown recently that oxygen reduction reaction also takes place during corrosion of Mg [33, 81, 82]. However, this is a secondary reaction (complementing water reduction) contributing to 1-20% of the total cathodic current depending on the conditions. Hence, it is not taken into consideration in this model. Additionally, the involved chemical reactions are more complicated in SBF solutions due to the presence of further inorganic ions and the formation of a layered precipitate structure [35], but the effect of these ions is currently encapsulated in the reaction rates and the diffusion coefficients of the developed mathematical model. The summary of the considered chemistry to develop the mathematical model is depicted in Fig. 3.1.

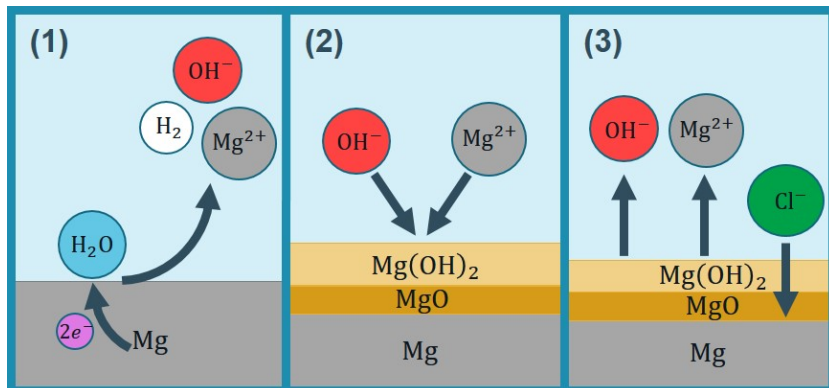


Figure 3.1: The chemistry of biodegradation of Mg considered in the current study: 1) Mg oxidation and water reduction processes accompanied by releasing Mg^{2+} and OH^- ions as well as H_2 gas, 2) formation of a partially protective precipitation layer, 3) dynamic solubility equilibrium and contribution of Cl^- .

3.3.2 Mathematical modeling

To keep track of the concentration changes of various contributing chemical components, we define four state variables for the concentration of Mg^{2+} ions, protective film (Mg(OH)_2), chloride (Cl^-) ions, and the hydroxide (OH^-)

ions:

$$\begin{aligned} C_{\text{Mg}} &= C_{\text{Mg}}(\mathbf{x}, t), & C_{\text{Film}} &= C_{\text{Film}}(\mathbf{x}, t) \\ C_{\text{Cl}} &= C_{\text{Cl}}(\mathbf{x}, t), & C_{\text{OH}} &= C_{\text{OH}}(\mathbf{x}, t) \quad \mathbf{x} \in \Omega \subset \mathbb{R}^3, \end{aligned} \quad (3.8)$$

which are indeed 4 scalar functions of space and time. Ω denotes the whole region of interest, including both the Mg bulk and its surrounding medium. By doing this, the value of pH at each point of Ω can be calculated as:

$$\text{pH} = 14 + \log_{10} C_{\text{OH}}, \quad (3.9)$$

where C_{OH} implies the activity of OH^- . By having the definition of the state variables in Eq. 3.8, the biodegradation of Mg described by Eqs. 3.5 and 3.6 can be represented as a set of reaction-diffusion PDEs:

$$\frac{\partial C_{\text{Mg}}}{\partial t} = \nabla \cdot (D_{\text{Mg}}^e \nabla C_{\text{Mg}}) - k_1 C_{\text{Mg}} \left(1 - \beta \frac{C_{\text{Film}}}{[\text{Film}]_{\max}} \right) + k_2 C_{\text{Film}} C_{\text{Cl}}^2 \quad (3.10)$$

$$\frac{\partial C_{\text{Film}}}{\partial t} = k_1 C_{\text{Mg}} \left(1 - \beta \frac{C_{\text{Film}}}{[\text{Film}]_{\max}} \right) - k_2 C_{\text{Film}} C_{\text{Cl}}^2 \quad (3.11)$$

$$\frac{\partial C_{\text{Cl}}}{\partial t} = \nabla \cdot (D_{\text{Cl}}^e \nabla C_{\text{Cl}}) \quad (3.12)$$

$$\frac{\partial C_{\text{OH}}}{\partial t} = \nabla \cdot (D_{\text{OH}}^e \nabla C_{\text{OH}}) + k_2 C_{\text{Film}} C_{\text{Cl}}^2 \quad (3.13)$$

in which the maximum concentration of the protective film can be calculated according to its porosity (ϵ) [68]:

$$[\text{Film}]_{\max} = \rho_{\text{Mg(OH)}_2} \times (1 - \epsilon). \quad (3.14)$$

D^e is the effective diffusion coefficient for each component. Due to the formation of the protective film, the diffusion coefficient is not constant and varies from the actual diffusion coefficient of the ions to a certain fraction of it. This fraction can be defined as ϵ/τ [83,84], in which ϵ and τ are the porosity and tortuosity of the protective film, respectively. The effective diffusion coefficient can be then calculated by interpolating the two aforementioned values:

$$D_i^e = D_i \left(\left(1 - \beta \frac{C_{\text{Film}}}{[\text{Film}]_{\max}} \right) + \beta \frac{C_{\text{Film}}}{[\text{Film}]_{\max}} \frac{\epsilon}{\tau} \right). \quad (3.15)$$

The β coefficient is called momentum here and controls the effect of the saturation term $(1 - \frac{C_{\text{Film}}}{[\text{Film}]_{\max}})$.

3.3.3 Interface movement formulation

In order to take advantage of the level set method for tracking the corrosion front, the velocity of the interface at each point should be determined. Then, by solving Eq. 3.4, the interface is obtained at the points with a zero value of the ϕ function. The interface velocity in mass transfer problems can be calculated using the Rankine–Hugoniot equation [85], and by considering the transportation of Mg²⁺ ions, it can be written as:

$$\{\mathbf{J}(x, t) - ([\text{Mg}]_{\text{sol}} - [\text{Mg}]_{\text{sat}}) \mathbf{V}(x, t)\} \cdot n = 0 \quad (3.16)$$

where \mathbf{J} is the mass flux at the interface. Rearranging Eq. 3.16 and inserting the value of the normal interface velocity into Eq. 3.4 yields:

$$\frac{\partial \phi}{\partial t} - \frac{D_{\text{Mg}}^e \nabla_n C_{\text{Mg}}}{[\text{Mg}]_{\text{sol}} - [\text{Mg}]_{\text{sat}}} |\nabla \phi| = 0, \quad (3.17)$$

which is the final form of the level set equation to be solved. In the case of simulations with a low diffusion rate, the interface moves slowly in the beginning, which results in a linear degradation, whereas based on the experimental results, the degradation rate is fast at the beginning and slows down eventually [36]. So, to mimic the same behavior in the low diffusion regimes, we took advantage of the theoretical Stefan formulation (Eqs. 3.1 and 3.2) to push the interface in the first time step. According to Eq. 3.1, the velocity of the interface can be calculated as $(2\alpha/\sqrt{t})$, but as we are dealing with a 3D model and not a 1D one, we pick a fraction (denoted by γ) of this ideal value to be used as the driving force of the interface at the beginning of the simulation. So, the normal velocity of the interface can be written in the general form as:

$$V^N(x, t) = \begin{cases} \gamma \frac{2\alpha}{\sqrt{t}} & t = 0 \\ \frac{D_{\text{Mg}}^e \nabla_n C_{\text{Mg}}}{[\text{Mg}]_{\text{sol}} - [\text{Mg}]_{\text{sat}}} & t > 0 \end{cases} \quad (3.18)$$

in which the α value should be calculated from Eq. 3.2. By selecting γ equal to zero, the Stefan formulation can be eliminated, and a value of 1 for γ restores the ideal 1D velocity definition.

3.3.4 Boundary conditions

The implementation of boundary conditions is relatively challenging and complex for the developed model as they should be imposed inside the domain of interest on virtual interfaces defined by mathematical expressions

(i.e. on the moving interface defined by the zero iso-contour of the level set equation). The penalty method was used to overcome this issue and define the desired boundary conditions on the moving corrosion front.

Fig. 3.2 demonstrates a schematic presentation of the boundary conditions and general considerations of each PDE of the biodegradation mathematical model. This figure is divided into 5 different parts, presenting the 5 PDEs of the model. The Mg block is depicted in the center, and the interface separates it from the surrounding medium. There is no specific boundary condition for the level set and film formation equations, but in comparison to the other 3 transport equations, it should be noted that diffusivity is not considered for Mg(OH)_2 , which is also reflected in Eq. 3.11. The level set function ϕ is defined in a way that is positive inside and negative outside the solid region. For the Mg^{2+} ions transport equation, a Dirichlet boundary condition is applied on the mathematical interface to make the concentration equal to the saturation concentration of Mg^{2+} ions, a value that was already used in Eq. 3.17. For the Cl^- and OH^- ions transport equations, a no-flux boundary condition is applied to the interface by making the diffusion coefficient equal to zero inside the Mg block, preventing ions to diffuse inside the solid material.

3.3.5 Implementation

To simulate the developed mathematical model, which is comprised of Eqs. 3.10, 3.11, 3.12, 3.13, and 3.17, a combination of finite difference and finite element methods was used, leading to discrete forms of these equations, which were subsequently solved using appropriate linear solvers.

To discretize the temporal terms of the aforementioned parabolic PDEs, a first-order backward Euler finite difference scheme was used, whereas the spatial terms were converted to a weak form using a standard first-order finite element scheme. Then, the open-source PDE solver FreeFEM [86] was used to implement the weak form and obtain a linear system of equations for each PDE. The obtained linear systems were solved in parallel using the HYPRE preconditioner [87] and the GMRES solver [88] via the open-source high-performance computing (HPC) toolkit PETSc [89]. Additionally, to increase the efficiency of the computation and decrease the simulation execution time, the computational mesh was decomposed and distributed among available computing resources using the interface of HPDDM package in FreeFEM [90]. The details of this implementation are presented in Chapter 7. A simple iterative solver based on the Newton method was also developed to solve Eq. 3.2 to obtain the value of α parameter if it was required in the simulations.

The computational mesh was generated using a set of first-order tetrahe-

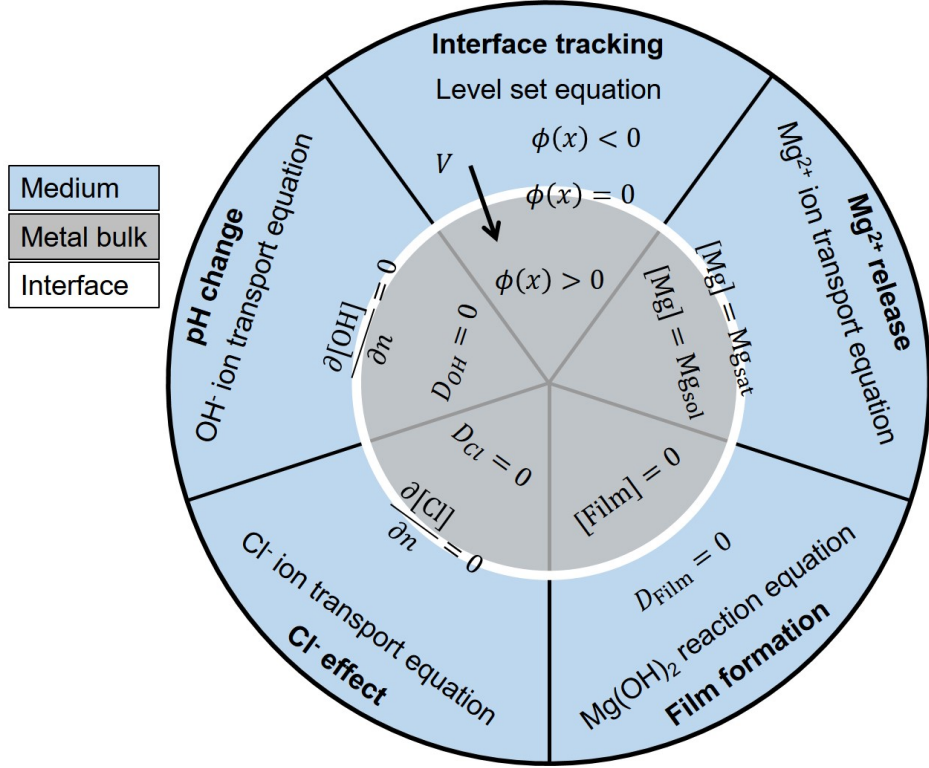


Figure 3.2: A schematic overview of the exposed boundary conditions and constraints required for the simulation of each equation of the developed mathematical model for Mg biodegradation.

dral elements and was adaptively refined on the metal-solution interface to increase the numerical accuracy of the simulation of the level set equation (Eq. 3.17). The Netgen mesh engine [91] in the SALOME platform [92] was used to generate the mesh.

Similar to the technique employed by Bajger et al. [68], the gradient of concentration of Mg²⁺ in Eq. 3.17 was calculated at a distance h in the normal direction from the interface, with h being the smallest element size of the mesh:

$$\nabla_n C = \frac{C(\mathbf{x} + h.n) - C(\mathbf{x} + 2h.n)}{h} \quad \mathbf{x} \in \Omega \subset \mathbb{R}^3. \quad (3.19)$$

Considering the adaptively refined mesh, the h value is very small, so the gradient is computed at the regions close enough to the interface. In addition to this technique, the mass lumping feature of FreeFEM was used to prevent the oscillation of concentration values on the diffusive metal-medium interface.

3.3.6 Experimental setup

The degradation rate of CP Mg was evaluated based on the hydrogen evolution tests performed either in NaCl or SBF solutions with eudiometers. The composition of the electrolytes is shown in the following table (Table 3.1). 0.5 g metallic chips (with a surface area of $47.7 \pm 5.0 \text{ cm}^2/\text{g}$ and chip thickness ca. 200 microns) of CP Mg were put in 500 ml electrolyte for 22-24 hours for monitoring the amount of evolved hydrogen. The method of measuring evolved hydrogen was chosen for monitoring the degradation rate because although such a measurement is prone to experimental errors such as relatively high solubility of hydrogen in water and volume change due to temperature and pressure variations, it provides a continuous assessment of the process, resulting in a continuous and smooth curve. Additionally, as small metallic chips were used for the tests, it was not possible to clean these pieces in chromic acid without losing them to measure the mass loss directly. The drawback of choosing the evolved hydrogen as the monitoring method is that it is not the only occurring reaction since oxygen reduction also takes place during the process [33, 81, 82]. As a result, measuring only hydrogen does not capture the totality of the degradation reactions. However, for CP Mg, the contribution of oxygen reduction is low (in contrast to high-purity Mg [33]) and can simply be ignored, meaning that the evolved hydrogen is an accurate equivalent for the mass loss. The bulk pH of electrolytes before and after corrosion was measured by a pH meter (Metrohm-691, Switzerland). Local pH was measured by positioning pH microprobes (Unisense, Denmark, pH-sensitive tip size 10x50 micron) 50 micron above the surface of Mg and monitoring the pH values either in one spot or by horizontal or vertical line-scans or mapping by following a horizontal grid. The electrolytes were not pH buffered additionally since SBF contains carbonates and phosphates that stabilize the pH at the approximate value of 8.5 instead of the 10.5 characteristic for pure NaCl solutions where pH is stabilized by precipitation of Mg(OH)_2 . Meanwhile, synthetic pH buffers, such as TRIS and HEPES were proven to affect the degradation mechanism rather significantly and should not be used for this purpose [35]. The measurements were performed at room temperature of $22 \pm 2^\circ\text{C}$ maintained by the laboratory climate control system. More detailed information about experimental set up and procedures can be found elsewhere [36, 40].

3.3.7 Parameter estimation

The constructed mathematical model contains some parameters that need to be calibrated prior to final validation of the model: diffusion coefficient of

Table 3.1: Chemical composition of NaCl and SBF electrolytes used to perform hydrogen evolution tests, weight loss, local and bulk pH measurements.

| | Concentration / mM | |
|---|--------------------|-----------|
| | 0.85 wt. % NaCl | SBF |
| Na ⁺ | 145.4 | 142.0 |
| K ⁺ | - | 5.0 |
| Mg ²⁺ | - | 1.5 |
| Ca ²⁺ | - | 2.5 |
| Cl ⁻ | 145.4 | 147.8 |
| HCO ₃ ⁻ | - | 4.2 |
| HPO ₄ ²⁻ /H ₂ PO ₄ ⁻ | - | 1.0 |
| SO ₄ ²⁻ | - | 4.2 |
| Synthetic pH buffer (i.e. Tris/HCl, HEPES) | No | No |
| Initial pH value | 5.6-5.9 | 7.35-7.45 |

Mg²⁺ and Cl⁻ ions (D_{Mg} and D_{Cl} to be inserted into Eq. 3.15 to get effective diffusion coefficients), the reaction rates of Eqs. 3.5 and 3.6 (k_1 and k_2), the momentum parameter, β , for controlling the saturation term behavior (in Eqs. 3.10, 3.11, and 3.15), and the γ parameter for the initial interface velocity (Eq. 3.18). An inverse problem setup was required to estimate the proper value of these parameters.

Performing a parameter estimation requires running the computational models several times. Considering the computationally-intensive model of the current study, a sensitivity analysis was performed prior to the parameter estimation to exclude non-essential parameters and reduce the time required to complete the inverse problem run. This sensitivity analysis was accomplished separately in the low diffusion (similar to the SBF solution) and high diffusion (similar to NaCl solution) regimes.

After determining the essential parameters to include, a Bayesian optimization approach [93] was used to construct the inverse problem and calibrate the parameters. The reason for choosing a Bayesian approach was to minimize the number of optimization iterations, in each of which the simulation should run once. The Bayesian optimization is a more efficient option for such computational intensive cases in comparison to gradient-based or fully-stochastic methods as it takes into account all the preceding iterations in a probability tree [94].

The objective function of the optimization problem was the difference between the predicted and experimentally obtained values of evolved hydrogen.

In the computational model, the evolved hydrogen can be computed directly at any time through the mass loss as each mole of corroded Mg is correlated to one mole of released hydrogen (Eq. 3.5). The mass loss can be obtained using the following volume integral:

$$Mg_{\text{lost}} = \int_{\Omega_+(t)} [Mg]_{\text{sol}} dV - \int_{\Omega_+(0)} [Mg]_{\text{sol}} dV, \quad (3.20)$$

where $\Omega_+(t) = \{\mathbf{x} : \phi(\mathbf{x}, t) \geq 0\}$, and then, the amount of produced hydrogen is calculated using the ideal gas law:

$$H_f = \frac{Mg_{\text{lost}}}{Mg_{\text{mol}}} \frac{RT}{P} \quad (3.21)$$

in which R , P , T , Mg_{mol} are the universal gas constant, the pressure, the medium temperature, and the molar mass of Mg, respectively.

3.3.8 Simulation setup

In order to simulate the developed mathematical model, the experimental setup was reconstructed *in silico* with some minor differences. As there is no perfusion in the solution chamber, the mixing effect was neglected, so, as can also be seen in the mathematical model, the advection terms were not considered. Furthermore, the experiments were conducted using small metallic chips, yet, as the biodegradation behavior heavily depends on the exposed surfaces, we represented these chips by a cuboid with the same surface-to-mass ratio. By considering the approximate surface-to-mass of $50\text{cm}^2/\text{g}$ and the total mass of 0.5g , the chips were replaced by a cuboid with the size of $60\text{mm} \times 21\text{mm} \times 0.2\text{mm}$, which approximately has the same ratio, surface area, volume, and mass. Also, the solution chamber with a capacity of 500ml was represented by a cubic container with an edge size of 80mm . Fig. 3.3 depicts the constructed geometry as well as the computational mesh generated to represent it. The mesh is refined on the interface and contains 18,049,471 elements, resulting in 3,077,227 degrees of freedom (DOF) for each PDE.

Simulations were carried out on the VSC (Flemish Supercomputer Center) supercomputer. Taking advantage of HPC techniques to parallelize the simulation is an inevitable aspect of such a computational-intensive model, so based on what described in the implementation section, the mesh was decomposed among 170 computing cores, i.e. 24,137 DOF per core (which includes the ghost nodes to satisfy the boundary condition in each sub-mesh). On the VSC supercomputer, we made use of 5 nodes, 36 cores each, each

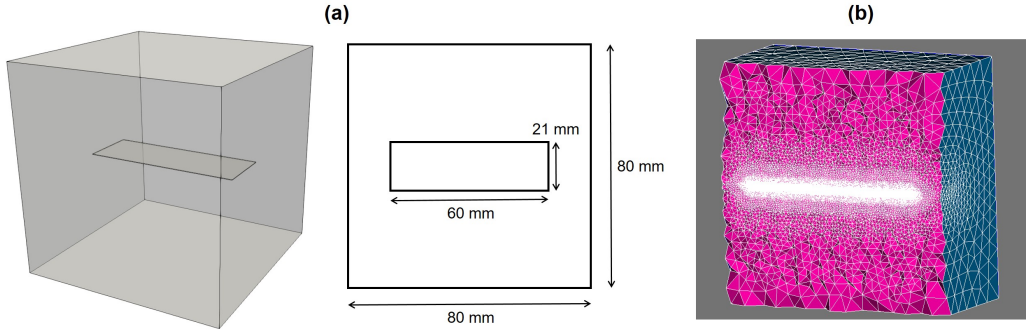


Figure 3.3: Computational representation of the experimental set-up, used to perform parameter estimation and numerical validation of the developed model. a) A cuboid of Mg ($60\text{mm} \times 21\text{mm} \times 0.2\text{mm}$) inside a solution, b) a cross-section of the computational mesh, refined on the corrosion front to increase the required level set accuracy.

node holding CPUs with a clock speed of 2.6 GHz, with 960 GB of the total available memory.

The OH^- transport equation (Eq. 3.13) was not solved during the parameter calibration process. Afterwards, two full simulations (for the NaCl and SBF solutions) were conducted to calculate the pH changes based on the change of the concentration of OH^- ions in the medium. This acted as the validation of the numerical model because no calibration was performed on the output of this equation. The pH was calculated using Eq. 3.9, based on the solution of Eq. 3.13 and a reported value of $7.00e \times 10^{-5}\text{cm}^2/\text{s}$ ($25.2\text{mm}^2/\text{hour}$) for the diffusion coefficient of OH^- ions (D_{OH} to be used in Eq. 3.15) in aqueous solutions [95].

According to the experimental setup, the initial concentration of the Mg^{2+} , Cl^- , and OH^- ions were set to 0 (no Mg^{2+} ions at the beginning), 146mM ($5.175 \times 10^{-6}\text{g/mm}^3$), and $1 \times 10^{-7}\text{g/mm}^3$, respectively. The porosity (ϵ) and tortuosity (τ) of the protective film were considered to be 0.55 and 1, respectively [76]. The saturation concentration $[\text{Mg}]_{\text{sat}}$ was set to the solubility of magnesium chloride in water, which is $134 \times 10^{-6}\text{g/mm}^3$ at 25°C [96]. The density of Mg ($[\text{Mg}]_{\text{sol}}$) and $\text{Mg}(\text{OH})_2$ were set to $1735 \times 10^{-6}\text{g/mm}^3$ and $2344 \times 10^{-6}\text{g/mm}^3$, respectively [68]. A time step convergence study was performed to determine the implicit time step size. Based on the results, a time step with a size of 0.025 hours was chosen. The overall simulated time is 22 hours in accordance with the experimental design of performed immersion tests.

3.3.9 Case study

To further investigate the predictions of the current model on more complex shapes, the biodegradation of a simple screw was studied in the SBF solution using the parameters obtained for the low diffusion regimes. Similar to the simulation of Mg cuboid, the mesh was refined on the metal-medium interface, and it consisted of 1,440,439 elements with 246,580 DOFs for each PDE. All the simulation parameters and materials properties were identical to the simulation of biodegradation in the SBF solution, and the target was to simulate 42 days (1008 hours) of the process. This was selected as a sufficiently long simulated time to observe the effects of biodegradation on larger time scales. The goal of this case study is to demonstrate the applicability of the developed model for any desired 3D shape with no geometrical limitations. As a result, although it was possible to consider a more complicated geometry for the screw (for example by considering threads around the cylindrical part of the screw or having a realistic geometry for the head), the screw geometry consists of basic 3D primitives, which are adequate for the mentioned purpose.

3.4 Results

3.4.1 Optimization results

Based on the performed sensitivity analysis, two parameter sets were obtained for the high diffusion (in NaCl solution) and low diffusion (in SBF solution) simulations, respectively. These parameters are listed in Table 3.2. According to the results, the reaction rate of Eq. 3.5 (k_1), which demonstrates the rate of oxidation-reduction, has less contribution to the process in comparison to the rate of the weakening of the protective film (k_2). Because of this, the parameter k_1 was not selected for the parameter estimation. Also, the model was sensitive to the effect of parameter k_2 in different ranges of values and not on a specific point, and as a result, three constant values were chosen as the delegates of these ranges in the optimization process. The model was not sensitive to the diffusion rate of Cl^- ions, which was also expected because although Cl^- has an important role in the weakening of the partially protective MgO film, its transport equation (Eq. 3.12) is purely diffusive and does not include any reaction term.

The parameter optimization process was performed on the specified range of selected parameters, while the rest of the parameter values were obtained from the literature [68,95]. Table 3.3 shows the output of this process, which was used to simulate the full model. For two estimation processes, 120 opti-

Table 3.2: The effective parameters as the result of the sensitivity analysis and their corresponding range to be considered in the Bayesian optimization for parameter calibration

| | Parameter | Optimization range |
|-----------------------------------|-----------------|-----------------------------|
| Low diffusion (SBF solution) | D_{Mg} | [0.0001, 0.01] |
| | k_2 | $10^{10}, 10^{15}, 10^{20}$ |
| | β | [0.1, 10] |
| | γ | [0, 1] |
| High diffusion (NaCl solution) | D_{Mg} | [0.003, 0.1] |
| | k_2 | $10^{10}, 10^{15}, 10^{20}$ |
| | β | [0.1, 10] |

Table 3.3: Values used to evaluate the model performance, obtained from the output of the optimization process and the literature.

| Parameter | D_{Mg} | D_{Cl} | D_{OH} | k_1 | k_2 | β | γ |
|---------------|-----------------------------------|-----------------------------------|-----------------------------------|-------------------------|--|---------|----------|
| Unit | $\frac{\text{mm}^2}{\text{hour}}$ | $\frac{\text{mm}^2}{\text{hour}}$ | $\frac{\text{mm}^2}{\text{hour}}$ | $\frac{1}{\text{hour}}$ | $\frac{\text{mm}^6}{\text{g}^2 \text{hour}}$ | - | - |
| SBF solution | 0.000338 | 0.05 | 25.2 | 7 | 10^{15} | 0.125 | 0.65 |
| NaCl solution | 0.06273 | 0.05 | 25.2 | 7 | 10^{20} | 0.2 | 0 |

mization iterations were taken cumulatively, which took 276 hours of simulation execution time using 170 computing nodes for each simulation.

3.4.2 Degradation prediction

Fig. 3.4 shows the model output for the predicted produced hydrogen, protective film formation, and the pH changes. The graph of the evolved hydrogen is used as input during the parameter optimization process, but the pH results are produced by the simulations using the optimized parameters to demonstrate the validation of the developed mathematical and computational models. The predicted pH result (Fig. 3.4-d) shows a difference of 5.35% for the simulation in NaCl and 1.03% for SBF simulation. Each simulation took about 3 hours to complete.

In Fig. 3.4, a post-processed view of the final shape of the Mg cuboid in the NaCl solution is presented, in which the degraded geometry is plotted on the Mg^{2+} ions (Fig. 3.4-b) and protective film concentration (Fig. 3.4-c) contours. A transparent contour of the pH values in the solution is depicted for both the NaCl (Fig. 3.4-e) and SBF (Fig. 3.4-f) solutions. The range of colors is kept equal for both contours to make it easy to compare the change

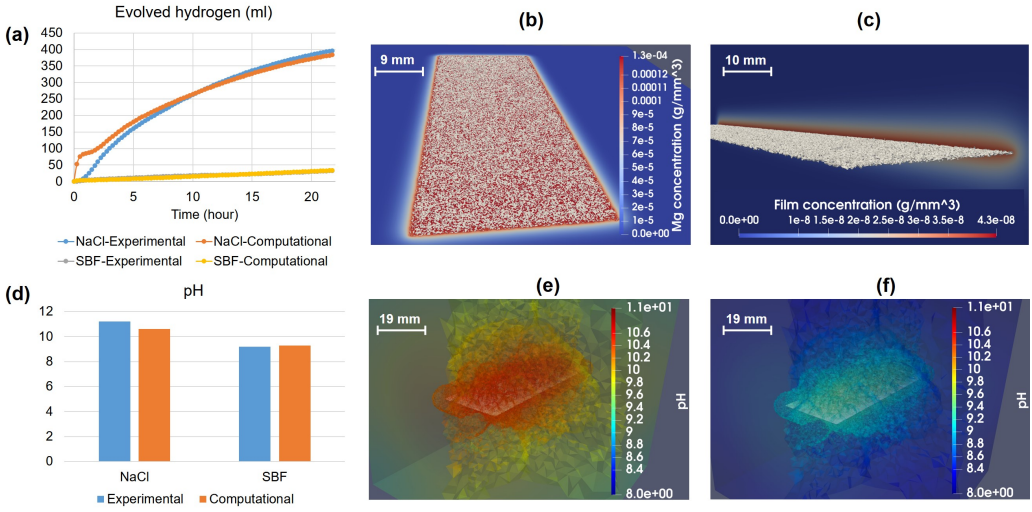


Figure 3.4: Comparing the quantitative output of the model for the rate of degradation and the pH changes in NaCl and SBF solutions with experimentally measured values as well as the simulation results for ion release, mass loss, protective film formation, and pH changes after 22 hours of simulated time: a) calibrated output of the formed hydrogen gas during the degradation (the SBF curves are overlapped), b) the simulation results of Mg^{2+} ions release, c) the simulation results of protective film concentration at the end of the simulation (the color contour shows the concentration of species, and the gray surface is the zero iso-contour of the level set function, which indicates the surface of the Mg block), d) de novo prediction of the global pH changes in the medium, showing a good agreement between the model output and the experimental results, e) pH changes in different regions of the medium in NaCl solution, f) pH changes in SBF solution.

of pH in both solutions.

The concentration values of the state variables of the derived transport PDEs (Mg^{2+} , Cl^- , OH^- , and $Mg(OH)_2$) are plotted along a diagonal line in the solution container in Fig. 3.5, showing how they change in the zones close to the corrosion surface and far from it.

3.4.3 Example application

The simulation of 42 days (19,200 time steps) of the degradation of the simple screw took 9 hours to run using 170 computing cores. Fig. 3.6 depicts the post-processed interface and Mg^{2+} ions release (similar to Fig. 3.4-b) as well as the mass loss during the degradation of the screw in the SBF solution. It

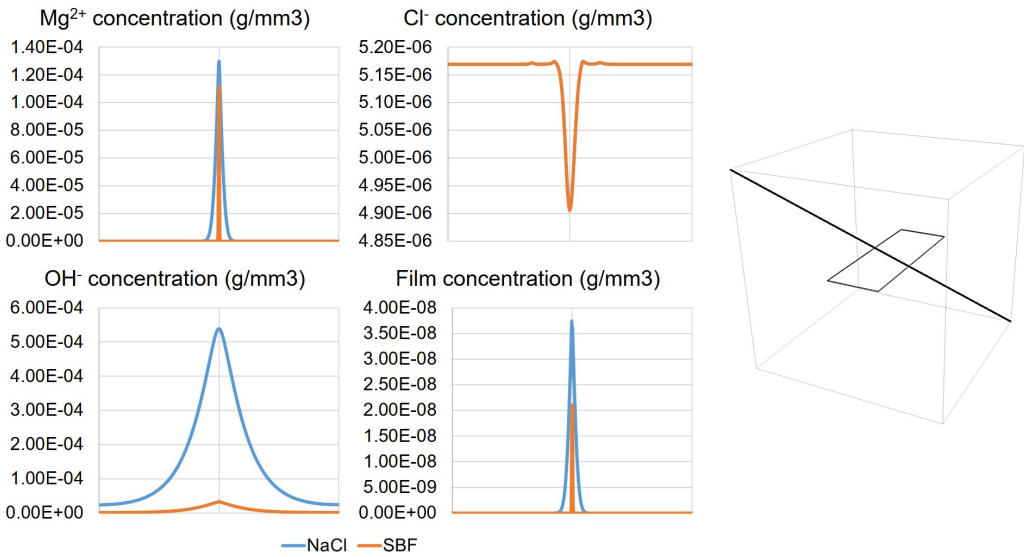


Figure 3.5: The change of concentration for the involved chemical components, Mg^{2+} , Cl^- , OH^- ions, and the protective precipitation structure (which can be correlated to the thickness of the layer) plotted over a diagonal line as shown in the right.

is worth mentioning that the roughness observed on the surface of the screw geometry is related to the node-based visualization of the level-set function evolution and is not caused by either non-uniform corrosion or numerical error in the simulations.

3.5 Discussion

In this study, a physicochemical model of the biodegradation process of commercially-pure Mg was developed by constructing a mathematical model formulating the mass transfer phenomena as well as tracking the location of the surface of the implant during degradation. For the mass transfer model, the equations were derived from the chemistry of biodegradation of the Mg in saline (NaCl) and buffered (SBF) solutions, which includes the oxidation of the metallic part, reduction of water, changes in pH, and formation of a protective film on the surface of the scaffold which contributes to a slower rate of degradation. Beside these aspects, it was also crucial to consider the effect of different ions in the medium on the rate of degradation. Additionally, investigating the structural changes of the scaffolds and implants in practical applications, like resorption of temporary fixation devices, re-

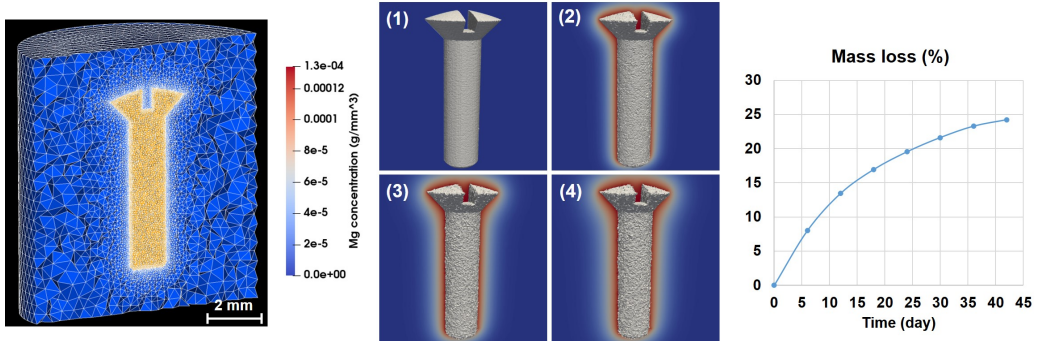


Figure 3.6: A cross-section of the computational mesh and simulation results of the degradation process of the use-case screw in SBF solution as well as the mass loss graph over time. The contours display the concentration of Mg^{2+} ions on a cross-section view of the medium beside the moving surface of the screw at 1) 1st day (initial state), 2) 6th day, 3) 12th day, and 4) 18th day.

quires tracking the movement of the corrosion surface. This was done by constructing an equation based on the level set principle, which captured the movement of the medium-metal interface by defining an implicit surface. The derived equations were coupled and solved using a combination of finite difference and finite element methods. The degradation data to validate the models was collected from immersion tests of small Mg chips, reconstructed as a single cuboid in the computational study with a similar surface over volume properties. The model parameters were calibrated using a Bayesian optimization algorithm, and the obtained parameters were used to simulate the pH changes in NaCl and SBF solutions.

The developed model falls in the categories of physical models of the corrosion process, which provide more insights of the process in comparison to the phenomenological models. The reason is that the phenomenological models focus on the elimination of elements to capture the loss of materials, which makes it impossible to model the formation of new chemical compounds or interaction of species [97]. The physical models, like the one developed in this study, are capable of capturing the underlying chemical interactions. By doing this, processes like the effect of coating, the formation of a protective layer, and pH changes can be modeled. Adding an appropriate interface tracking method enables the physical models to act like the phenomenological models in capturing the corrosion interface movement. In the current study, this has been accomplished using a level set function. Technically speaking, this approach has certain benefits over the ALE method, which is

the method used by several similar studies, including Grogan et al. [66]. In comparison to the ALE method, the level set function tracks the interface instead of a Lagrangian mesh, and elements can freely be marked as solid or liquid. Additionally, employing the ALE method for degradation simulation requires remeshing the geometry as the interface moves, which is not efficient for 3D models and is limited to the available features of the employed numerical solver.

One of the challenging aspects of validating physical models is getting the correct value for the parameters of said models, requiring dedicated experimental input. To overcome this challenge, an efficient inverse problem was constructed based on the Bayesian optimization approach to estimate the unknown parameters. To save time and resources, the parameter estimation process was performed on the most effective parameters, which were selected based on a sensitivity analysis. This selection process implied the importance of parameters in high and low diffusion rates. This included the diffusion coefficients (except the diffusion rate of the hydroxide ion), which were subsequently used in Eq. 3.15 to get the effective coefficient employed in the derived PDEs. The objective function of the optimization process was the difference in the mass loss predicted by the computational model and the experiments, but instead of direct mass loss measurement, we measured the volume of formed hydrogen gas in Mg corrosion, which then was converted to mass loss by considering the stoichiometry of the reactions.

The degradation rate is fast at the beginning, but then it slows down due to the formation of a partially protective film and also because of the saturation concentration. This phenomenon is well captured by the model at high diffusion rates, but in low diffusion rates (in SBF solution), this effect can be reproduced by pushing the corrosion front according to the Stefan formulation of the moving interface problems. This was controlled by the parameter γ (Eq. 3.18). The sensitivity test demonstrated that this parameter doesn't have a significant effect in the high diffusion rates, but for the low diffusion regimes, it was considered in the parameter estimation process. It should be noted that the inclusion of the γ parameter is crucial for short-term simulations only, helping the model mimic the chemical behavior correctly. In other words, the long-term degradation behavior can be successfully simulated without considering the parameter γ . For example, the sensitivity test (Table 3.2) has marked γ as an effective parameter because it plays an important role in the first 22 hours of degradation model behavior. But, for the case study, the result (the graph in Fig. 3.6) would be almost the same with γ set to zero since 40,320 time steps (1008 hours) passed after applying the parameter in the first time step.

For the high diffusion regime simulation, the results show a difference

between the experimental and computational data in the early stages of the degradation process (Fig. 3.4-a). The reason for this behavior lies within Eqs. 3.17 and 3.19, in which the interface velocity was correlated to the gradient of released ions. In high diffusion rates, the material release occurs very fast, so the calculated gradient (Eq. 3.19) vanishes for a short period until the diffusion becomes more uniform. As a result, the interface does not move, and according to Eq. 3.20, no mass loss gets calculated. This effect was automatically ignored in the parameter estimation process since the objective function considers the overall degradation behavior.

The degradation of the CP Mg was assumed to be mostly diffusion-based. As a result, the value of D_{Mg} plays an important role in the behavior of the model. Although it was possible to get the diffusion coefficient of Mg^{2+} from the previously conducted experiments in the literature (similar to what was done for D_{OH}), we decided to not do so because of two reasons: 1) the values reported in the literature are mostly valid for saline solutions only, and 2) the reported values were not in a good agreement with one another [66, 76]. Thus, the diffusion coefficient was obtained using the parameter estimation process for both the NaCl and SBF solutions. The obtained value of D_{Mg} ($0.06273 \text{ mm}^2/\text{hour}$) was in line with the values that Grogan et al. have already suggested ($0.010575 - 0.50575 \text{ mm}^2/\text{hour}$) [66], showing that the constructed inverse problem was successful in reproducing previous results of similar studies. The obtained value of D_{Mg} in the Bajger et al. work [68] is $0.00066 \text{ mm}^2/\text{hour}$, which is mostly related to the simplicity of the employed parameter estimation method as well as having a 2D model instead of a 3D one.

In the *in vitro* biodegradation of Mg-based biomaterials, the local pH of the surrounding solution increases less than that in NaCl solution. This is because the $\text{Mg}(\text{OH})_2$ formed in NaCl stabilizes pH at 10.4 [98], while Mg-Ca-P-C containing products stabilize the pH at 7.8-8.5 since OH^- is consumed for the formation of this product [36, 39]. This phenomenon was captured in Eqs. 3.13 and 3.9 to calculate pH based on the concentration of OH^- ions, showing the local pH changes at any location (Fig. 3.4-e,f). In the current study, the global pH is considered as the validation criterion, which means that the average value of the solution pH is calculated using a volume integral and is compared with the ones obtained from the experiments. Fig. 3.4-d shows that such a prediction has a good agreement with the experimental data.

One of the biggest simplifications of the current study was made by ignoring the contribution of pH changes to the biodegradation mechanism of Mg. Although doing that is relatively simple and straightforward in the approach taken by this study, it results in non-linear terms in the derived PDEs. This

non-linearity inserts another level of complexity to the computational model as the order of the state variables are in the range of 10^{-6} to 10^{-10} , which makes it difficult to yield convergence in the iterative non-linear solvers. By developing a robust non-linear solver, this effect can be added simply by including more relevant terms as the effect of Eq. 3.13 into Eq. 3.10.

Additionally, buffered solutions and the physiological fluids inside the human and animal bodies contain more ions interacting with more complex chemistry [35]. In this study, this effect was encapsulated in a limited number of parameters (such as k_1 and k_2 in Eqs. 3.10, 3.11, and 3.13), but while the results show its success to reproduce experimental observations, it still needs additional elaboration to be able to capture more chemical interactions. For example, SBF solutions contain phosphates, carbonates, and calcium that form hydroxyapatite-like compounds on the surface of Mg, acting as rather strongly blocking corrosion products. In the current state of the developed model, such an effect on the corrosion rate was captured by a low effective diffusion coefficient (Eq. 3.15) for the Mg transport. In future model developments, the effect of presented inorganic ions such as HCO_3^- , $\text{HPO}_4^{2-}/\text{H}_2\text{PO}_4^-$, and Ca^{2+} can be added similar to the way the effect of Cl^- was considered. Additionally, formulating the effect of HPO_4^{2-} that exists in the physiological environments will make the model capable of making more accurate predictions for *in vivo* studies.

A common approach in mechanistic studies is to start with a pure material and gradually increasing complexity by adding impurities and alloying elements. This approach was followed in the current study by beginning with a model for pure Mg that captures the major reactions. The developed model can be further extended to Mg alloys by considering the effect of alloying elements on the reaction rates as well as adding more terms to the transport equations to capture the electrochemical potential changes, converting the PDEs into the Nernst–Planck equation [99]. By doing so, more complex forms of the corrosion process, such as galvanic corrosion, can be predicted by the model. This will increase the applicability of the model for biomedical cases since pure Mg is not commonly used for medical-graded applications. As an additional future development, the corrosion layer can be considered to be heterogeneous, making it possible to simulate the cathodic reactions by randomly distributing more active spots on the surface. Alternatively, a similar effect can be achieved by adapting the degradation rates using polarization curves and introducing an active spot for inhomogeneous anodic dissolution [100]. Applying this will enable the model to take into account additional corrosion products formed due to additional alloying elements such as Zn, Ca, Ag, rare-earth elements, and detrimental cathodic impurities such as Fe.

Although the pH simulations are not enough experimental input to call the model fully validated, the obtained validation results show that the derived mathematical model and the corresponding parallelized computational model give a correct *in silico* representation of the studied process. The performed predictive simulations, including the case study, demonstrate the potential of the developed computational model and software to study the biodegradation behavior of implants. This can be further combined with other computational models to provide a multidisciplinary environment to investigate the mechanical integrity of implants or induced neotissue growth for different applications in orthopedics and tissue engineering.

3.6 Conclusions

The use of biodegradable metals for designing medical devices and implants has the challenge of controlling the release and rate of degradation, which is usually investigated by conducting *in vitro* and *in vivo* tests requiring conducting multiple experiments for different scenarios and situations. In this study, we have developed a mathematical model to predict the biodegradation behavior of commercially pure Mg-based biomaterials, which makes it possible to study the corrosion of implants and scaffolds in a simulated environment. Despite the assumed simplifications, the model can serve as an important tool to find the biodegradable metals properties and predict the biodegradation behavior of Mg-based implants that improves current design workflows.

Chapter 4

Extending the model: adding fluid flow and convection

This chapter is partially based on a manuscript prepared to be submitted:

M. Barzegari, C. Wang, S.V. Lamaka, G. Zavodszky, and L. Geris, “Interface-coupled multiphysics computational modeling of local pH changes during the biodegradation of magnesium biomaterials.”

Similar to the importance of perfusion in tissue engineering bioreactors, fluid flow plays an important role in biodegradation tests in hydrodynamics conditions. In this chapter, the development of a parallel fluid flow model is detailed, which is further coupled with the biodegradation model for simulating immersion tests in hydrodynamics setup.

4.1 Introduction

Considering fluid flow in the developed biodegradation model is crucial in light of the final application of the model, which is to be coupled with cell differentiation and tissue growth models to predict the rate of neotissue formation on biodegradable implants and scaffolds. In tissue engineering, cell expansion and differentiation experiments usually take place inside perfusion bioreactors, meaning that the flow of a biological fluid provides sufficient nutrients needed for the growth process and removes unnecessary and undesirable waste [101–103]. Moreover, the induced shear stress resulting from this perfusion plays a prominent role in the cell differentiation process [104–107], making the fluid flow inside the bioreactor even more critical. Consequently, the effect of the fluid flow should be considered in the biodegradation model

to enable it to make predictions in a perfusion setup, which is interchangeably called hydrodynamics conditions in chemistry.

Fluid flow in the context of a hydrodynamic condition has a similar application in corrosion and biodegradation experiments [108]. In a typical setup, the electrolyte moves and is refreshed over time to remove the corrosion products and provide needed mechanical stimuli if applicable. In biodegradation experiments, the flow velocity and induced shear stress affect the corrosion behavior of degradable scaffolds and implants due to increased mechanical forces and mass transfer [108]. Studies show that hydrodynamics conditions play a significant role in Mg degradation [109] where the corrosion rate increases in comparison to static conditions in immersion tests, in the presence of flowing [110], rotating [111], circulating [112], and *in vivo* perfusion [113]. Additionally, the fluid flow helps remove the corrosion products and avoid their accumulation [114].

The effect of hydrodynamics condition on the rate and pattern of biodegradation is rooted in the distribution and diffusion of fluids [115], which can be related to increment of mechanical stimuli like wall shear stress or increment in ions transport. It is reported that the presence of fluid flow leading to accelerated movement of the corrosive medium increases the rate of uniform and localized corrosion of Mg alloys [108]. The increase in corrosion rate is due to the increase of mass transfer of ions [115], affecting the chemical reactions occurring in the interface of Mg and the electrolyte [114,116]. Moreover, the increment in mass transfer removes more corrosion products from the surface, which is another contribution of the fluid flow to increasing the biodegradation rate [115]. Wang et al. [108] reported that the degradation rate was 0.37 ± 0.007 and $1.21 \pm 0.27 \text{mm.year}^{-1}$ for the corrosion of stents made of Mg AZ31 alloys in static and hydrodynamics conditions, respectively. After considering the volume loss with CT measurements, they have concluded that the corrosion rate of these alloys is three times more in the presence of fluid flow, increasing from $\sim 0.6 \text{mm.year}^{-1}$ in static condition to $\sim 1.5 \text{mm.year}^{-1}$ in a hydrodynamics setup [108]. This shows the significance of adding fluid flow to the developed biodegradation model.

Computational Fluid Dynamics (CFD) is the field of studying the dynamics of fluid flow using mathematical and computational methods [117, 118]. The fluid flow is usually expressed in the form of Navier-Stokes or Stokes equations, on which appropriate numerical schemes are applied and the derived system of equations is solved using computers, resulting in the prediction of flow patterns and secondary entities like the shear stress. CFD modeling has been used in tissue engineering to study fluid flow systems such as dynamic cell culture conditions in perfusion bioreactors [119–121].

In this chapter, a parallel computational model for fluid flow simulations

was developed and coupled with the biodegradation model. The model was developed by solving the derived equations, i.e., Navier-Stokes equations coupled with the Darcy effect for the degrading object, using the finite element method. To ensure proper verification of the simulation results, the model output was compared with an OpenFOAM simulation on the same geometry and setup.

4.2 Methods

4.2.1 Navier-Stokes equations

In its general form, the Navier-Stokes equations describing the flow of an incompressible fluid with constant density ρ in the domain $\Omega \subset \mathbb{R}^d$ (with d being the dimension, so 2 or 3) can be written as [122]:

$$\begin{cases} \frac{\partial \mathbf{u}}{\partial t} - \nabla \cdot [\nu(\nabla \mathbf{u} + \nabla \mathbf{u}^T)] + (\mathbf{u} \cdot \nabla) \mathbf{u} + \nabla p = \mathbf{f}, & x \in \Omega, t > 0, \\ \nabla \cdot \mathbf{u} = 0, & x \in \Omega, t > 0, \end{cases} \quad (4.1)$$

in which \mathbf{u} is the fluid velocity, p is the pressure (which is actually pressure divided by the density), $\nu = \frac{\mu}{\rho}$ is the kinematic viscosity (with μ being the dynamic viscosity), and \mathbf{f} is a force term. The equations are conservation of linear momentum and conservation of mass (also called continuity equation), respectively. When ν is constant, the diffusion term in Eq. 4.1 can be simplified as [123]:

$$\text{div}[\nu(\nabla \mathbf{u} + \nabla \mathbf{u}^T)] = \nu(\Delta \mathbf{u} + \nabla \text{div} \mathbf{u}) = \nu \Delta \mathbf{u}, \quad (4.2)$$

which turns Eq. 4.1 into the following form:

$$\begin{cases} \frac{\partial \mathbf{u}}{\partial t} - \nu \Delta \mathbf{u} + (\mathbf{u} \cdot \nabla) \mathbf{u} + \nabla p = \mathbf{f}, & x \in \Omega, t > 0, \\ \nabla \cdot \mathbf{u} = 0, & x \in \Omega, t > 0, \end{cases} \quad (4.3)$$

Eq. 4.3 satisfies the incompressibility condition $\nabla \cdot \mathbf{u} = 0$ and needs proper initial and boundary conditions to be well-posed. The initial condition can be defined as:

$$\mathbf{u}(\mathbf{x}, 0) = \mathbf{u}_0(\mathbf{x}) \quad \forall \mathbf{x} \in \Omega, \quad (4.4)$$

where \mathbf{u}_0 is a divergence-free velocity field. Various types of boundary conditions can be applied, but the ones we deal with in this chapter are described here. If $\partial\Omega$ is the boundary of Ω , it can be split into 3 distinct boundaries $\partial\Omega = \Gamma_1 \cup \Gamma_2 \cup \Gamma_3$ each of which with a different type. On Γ_1 , the inlet

can be defined as a Dirichlet boundary condition for the velocity for a given velocity profile \mathbf{g} :

$$\mathbf{u} = \mathbf{g} \quad \text{on } \Gamma_1 \quad (4.5)$$

On Γ_2 , a wall boundary no-slip condition can be considered:

$$\mathbf{u} = 0 \quad \text{on } \Gamma_2 \quad (4.6)$$

On Γ_3 , for the outlet condition, a homogeneous Neumann condition on velocity and a zero pressure condition can be defined like:

$$\frac{\partial \mathbf{u}}{\partial \mathbf{n}} = 0, \quad p = 0, \quad \text{on } \Gamma_3 \quad (4.7)$$

with \mathbf{n} being the normal direction on the boundary $\partial\Omega$. Broadly speaking, these boundaries can be grouped into 2 sets: $\Gamma_D = \Gamma_1 \cup \Gamma_2$ and $\Gamma_N = \Gamma_3$ for boundaries with Dirichlet and Neumann conditions, respectively.

The Navier-Stokes equations can be written componentwise for individual components of the flow vector field in the Cartesian coordinates. Denoting $u_i, i = 1, \dots, d$ (with $d = 2$ in 2D and $d = 3$ in 3D), Eq. 4.3 can be presented as:

$$\begin{cases} \frac{\partial u_i}{\partial t} - \nu \Delta u_i + \sum_{j=1}^d u_j \frac{\partial u_i}{\partial x_j} + \frac{\partial p}{\partial x_i} = f_i, & i = 1, \dots, d, \\ \sum_{j=1}^d \frac{\partial u_j}{\partial x_j} = 0. \end{cases} \quad (4.8)$$

4.2.2 Weak formulation of the Navier-Stokes equations

For deriving the weak formulation, the first equation of 4.3 is multiplied by a test function \mathbf{v} defined on a proper function space V (with \mathbf{H}^1 being the Sobolev space defined in domain Ω) in which the test functions vanish on the Dirichlet boundary:

$$V = [\mathbf{H}_{\Gamma_D}^1(\Omega)]^d = \{\mathbf{V} \in [\mathbf{H}^1(\Omega)]^d : \mathbf{v}|_{\Gamma_D} = \mathbf{0}\}. \quad (4.9)$$

yielding to:

$$\int_{\Omega} \frac{\partial \mathbf{u}}{\partial t} \cdot \mathbf{v} d\omega - \int_{\Omega} \nu \Delta \mathbf{u} \cdot \mathbf{v} d\omega + \int_{\Omega} [(\mathbf{u} \cdot \nabla) \mathbf{u}] \cdot \mathbf{v} d\omega + \int_{\Omega} \nabla p \cdot \mathbf{v} d\omega = \int_{\Omega} \mathbf{f} \cdot \mathbf{v} d\omega. \quad (4.10)$$

Applying Green's divergence theory results in:

$$-\int_{\Omega} \nu \Delta \mathbf{u} \cdot \mathbf{v} d\omega = \int_{\Omega} \nu \nabla \mathbf{u} \cdot \nabla \mathbf{v} d\omega - \int_{\partial\Omega} \nu \frac{\partial \mathbf{u}}{\partial \mathbf{n}} \cdot \mathbf{v} d\gamma \quad (4.11)$$

and

$$\int_{\Omega} \nabla p \cdot \mathbf{v} d\omega = - \int_{\Omega} p \nabla \cdot \mathbf{v} d\omega + \int_{\partial\Omega} p \mathbf{v} \cdot \mathbf{n} d\gamma \quad (4.12)$$

Substituting Eqs. 4.11 and 4.12 into Eq. 4.10 yields to:

$$\begin{aligned} & \int_{\Omega} \frac{\partial \mathbf{u}}{\partial t} \cdot \mathbf{v} d\omega + \int_{\Omega} \nu \nabla \mathbf{u} \cdot \nabla \mathbf{v} d\omega + \int_{\Omega} [(\mathbf{u} \cdot \nabla) \mathbf{u}] \cdot \mathbf{v} d\omega - \int_{\Omega} p \nabla \cdot \mathbf{v} d\omega \\ &= \int_{\Omega} \mathbf{f} \cdot \mathbf{v} d\omega + \int_{\partial\Omega} \left(\nu \frac{\partial \mathbf{u}}{\partial \mathbf{n}} - p \mathbf{n} \right) \cdot \mathbf{v} d\gamma \quad \forall \mathbf{v} \in V. \end{aligned} \quad (4.13)$$

The last term of Eq. 4.13 is expressed in accordance to the defined Neumann boundary condition, which vanishes on Γ_3 due to the defined condition in the current study (Eq. 4.7). Moreover, this term vanishes on the Dirichlet boundaries due to the properties of the function space V (Eq. 4.9).

Similarly, the second equation of 4.3 is multiplied by a test function q belonging to the function space Q (with \mathbf{L}^2 being a Hilbert space defined in domain Ω), called the pressure space:

$$Q = \mathbf{L}_0^2(\Omega) = \{p \in \mathbf{L}^2(\Omega) : \int_{\Omega} p d\omega = 0\}, \quad (4.14)$$

resulting in:

$$\int_{\Omega} q \nabla \cdot \mathbf{u} d\omega = 0 \quad \forall q \in Q. \quad (4.15)$$

Eqs. 4.13 and 4.15 are so called weak forms of the Navier-Stokes equations.

4.2.3 Stokes equations

For viscous flow, where the Reynolds number is less than 1 ($Re = \frac{|\mathbf{U}|L}{\nu}$, with L and \mathbf{U} being the representative length and velocity of the domain), the convection term of the Navier-Stokes equations can be neglected, simplifying Eq. 4.3 to [123]:

$$\begin{cases} \alpha \mathbf{u} - \nu \Delta \mathbf{u} + \nabla p = \mathbf{f} & \text{in } \Omega, \\ \nabla \cdot \mathbf{u} = 0 & \text{in } \Omega, \end{cases} \quad (4.16)$$

with α being a positive coefficient. Eq. 4.16 can be used to model laminar flow in low Reynolds regimes and is simpler to handle than Eq. 4.3 from

the numerical computing perspective. The weak formulation of the Stokes equation can be derived by following the approach taken for the Navier-Stokes equations in Section 4.2.2. The final form of the weak formulation is:

$$\begin{cases} \int_{\Omega} (\alpha \mathbf{u} \cdot \mathbf{v} + \nu \nabla \mathbf{u} \cdot \nabla \mathbf{v}) d\omega - \int_{\Omega} p \nabla \cdot \mathbf{v} d\omega = \int_{\Omega} \mathbf{f} \cdot \mathbf{v} d\omega & \forall \mathbf{v} \in V, \\ \int_{\Omega} q \nabla \cdot \mathbf{u} d\omega = 0 & \forall q \in Q, \end{cases} \quad (4.17)$$

Eq. 4.17 can be written in the standard finite element variational form by defining 2 bilinear terms $a : V \times V \mapsto \mathbb{R}$ and $b : V \times Q \mapsto \mathbb{R}$:

$$\begin{aligned} a(\mathbf{u}, \mathbf{v}) &= \int_{\Omega} (\alpha \mathbf{u} \cdot \mathbf{v} + \nu \nabla \mathbf{u} \cdot \nabla \mathbf{v}) d\omega, \\ b(\mathbf{u}, q) &= - \int_{\Omega} q \nabla \cdot \mathbf{u} d\omega, \end{aligned} \quad (4.18)$$

which simplifies the notation of the variational problem of the Stokes equation to:

$$\begin{cases} a(\mathbf{u}, \mathbf{v}) + b(\mathbf{v}, p) = (\mathbf{f}, \mathbf{v}) & \forall \mathbf{v} \in V, \\ b(\mathbf{u}, q) = 0 & \forall q \in Q, \end{cases} \quad (4.19)$$

in which

$$(\mathbf{f}, \mathbf{v}) = \sum_{i=1}^d \int_{\Omega} f_i v_i d\omega. \quad (4.20)$$

4.2.4 Implementation

Numerical implementation of the Stokes (Eq. 4.16) and Navier-Stokes (Eq. 4.16) equations can be tricky due to the presence of specific sources of instability, which highly depends on the type of studied fluid regime [124, 125]. Various numerical models have been presented for dealing with these equations, some of which are commonly used in CFD applications, such as the Newton-Raphson approximation of Navier-Stokes equations and the Chorin's projection method.

In order to increase the stability and avoid problems in the mathematical analysis of the numerical models (e.g., V-ellipticity property), a pseudo-compressibility assumption can be added to the continuity equation. The pseudo-compressible approximation appears as a pressure term εp with ε being a very small coefficient, resulting in the following equation as the final

form of the Navier-Stokes equations that we consider in this study [126]:

$$\begin{cases} \frac{\partial \mathbf{u}}{\partial t} - \nu \Delta \mathbf{u} + (\mathbf{u} \cdot \nabla) \mathbf{u} + \nabla p = \mathbf{f}, \\ \nabla \cdot \mathbf{u} + \varepsilon p = 0. \end{cases} \quad (4.21)$$

Similarly, the Stokes equation can be written as:

$$\begin{cases} \alpha \mathbf{u} - \nu \Delta \mathbf{u} + \nabla p = \mathbf{f}, \\ \nabla \cdot \mathbf{u} + \varepsilon p = 0. \end{cases} \quad (4.22)$$

Another challenging part is to approximate the convection terms in the equations. One of the best approaches to do so is to take advantage of the method of characteristics, in which the characteristics curves of a PDE are used to convert it to an ODE, resulting in a simpler solution. By using the method of characteristics for the convection term and a backward Euler discretization for the temporal term, the weak form of the Navier-Stokes and continuity equations (Eq. 4.21) can be rewritten as:

$$\begin{aligned} & \int_{\Omega} \frac{\mathbf{u}^{n+1} - \mathbf{u}^n \circ X^n}{\Delta t} \cdot \mathbf{v} d\omega + \nu \int_{\Omega} \nabla \mathbf{u}^{n+1} \cdot \nabla \mathbf{v} d\omega - \int_{\Omega} p^{n+1} \nabla \cdot \mathbf{v} d\omega = \int_{\Omega} \mathbf{f} \cdot \mathbf{v} d\omega \\ & \int_{\Omega} \nabla \cdot \mathbf{u}^{n+1} q d\omega + \varepsilon \int_{\Omega} p^{n+1} q d\omega = 0 \end{aligned} \quad (4.23)$$

in which $(\mathbf{u}^{n+1}, p^{n+1})$ are the unknowns to be computed from the known state \mathbf{u}^n coming from the previous time step or the initial condition. In Eq. 4.23, the term $\mathbf{u}^{n+1} - \mathbf{u}^n \circ X^n$ is corresponding to the convection term being approximated using the method of characteristics.

The weak form of the Stokes equations stays almost the same as Eq. 4.17 (because it does not contain transient and convection terms) but needs a slight modification to add the pseudo-compressible terms from Eq. 4.22:

$$\begin{aligned} & \int_{\Omega} (\alpha \mathbf{u} \cdot \mathbf{v} + \nu \nabla \mathbf{u} \cdot \nabla \mathbf{v}) d\omega - \int_{\Omega} p \nabla \cdot \mathbf{v} d\omega = \int_{\Omega} \mathbf{f} \cdot \mathbf{v} d\omega, \\ & \int_{\Omega} q \nabla \cdot \mathbf{u} d\omega + \varepsilon \int_{\Omega} p q d\omega = 0. \end{aligned} \quad (4.24)$$

The model was implemented in the open-source PDE solver FreeFEM [86] using P1 elements for the pressure and P2 elements for the velocity state variables. Eqs. 4.23 and 4.24 can be easily implemented in FreeFEM thanks to the built-in support of the method of characteristics via the `convect` function.

4.2.5 Preconditioning and parallelizing the computation

The solution of the Stokes and Navier-Stokes equations using the finite element method in 3D is a computationally intensive process, and as a result, taking advantage of high-performance techniques to reduce the simulation time becomes crucial in real-world applications. Preconditioning the system and parallelizing the simulation by partitioning the mesh and distributing the partitions among available computing nodes in a parallel computing setup are great solutions to this challenge.

In the current implementation, the METIS graph partitioner [127] and HPDDM package [90] were used to partition the computational mesh and distribute the load over the available resources. For preconditioning and improving the solution time of the derived equations, various (combinations of) preconditioners and iterative or direct solvers available in the PETSc toolkit [89] were tested to find the most suitable combination.

While exact factorization preconditioners (such as LU) are easy to implement and use for fluid flow applications, they show bad memory scaling profiles in large-scale problems, meaning that memory usage increases exponentially with the problem size, making it almost impossible to use them for 3D cases. A better solution for this class of problems is to take advantage of the FieldSplit preconditioner in the PETSc toolkit, which allows solving the derived linear system of equations using the block matrices technique. In this technique, the matrices are divided into smaller blocks, and separate preconditioners or solvers can be assigned to each block (each field). These blocks arise naturally from the underlying physics or numerical discretization of the problem, such as velocity and pressure in fluid flow applications. For matrices with an arbitrary number of blocks, three different “block” algorithms are available in the PETSc toolkit: block Jacobi (**additive**), block Gauss-Seidel (**multiplicative**), and symmetric block Gauss-Seidel (**symmetric_multiplicative**), which can be selected by passing the desired one to the `pc_fieldsplit_type` flag. For two blocks, like the one in fluid flow problems with velocity and pressure as the blocks, another family of solvers based on Schur complements can be used.

In the current study, the FieldSplit preconditioner with Schur complement approximation was used on two blocks for velocity and pressure. A GMRES KSP type [88] was employed to solve the preconditioned system with an iterative solver. An Algebraic Multigrid (AMG) preconditioner [128] was used for the velocity block, and a Jacobi preconditioner was assigned to the pressure block. The result of this configuration, as well as the request for appropriate monitoring tools, can be written as follows:

```

-ksp_monitor -ksp_converged_reason -ksp_type fgmres
-pc_type fieldsplit -pc_fieldsplit_type schur
-pc_fieldsplit_schur_fact_type full
-fieldsplit_velocity_pc_type gamg
-fieldsplit_velocity_ksp_type preonly
-fieldsplit_pressure_pc_type jacobi
-fieldsplit_pressure_ksp_max_it 5

```

to pass to PETSc while solving the equations.

4.2.6 Considering the degrading object

In biodegradation simulations, a degrading object exists in the fluid domain, through which the flow should not pass because it is a solid part. One common approach to handle this situation is to remove the solid part from the fluid flow mesh, but since the part shrinks over time, this is not a feasible and efficient approach, needing tremendous mesh recreation and removal during simulation. As a result, in the current study, the presence of the solid body as a barrier is taken into account by adding a Darcy term for the permeability to the Navier-Stokes and Stokes equations. A penalization technique is then employed to implement it in the weak formulation. To couple the fluid flow model with the biodegradation model, a convection term is added to the ions transport equations, causing the fluid velocity field advect the ions.

Adding the Darcy term to Eq. 4.16 and considering no other acting force yields to:

$$-\nu\Delta\mathbf{u} + \nabla p + \frac{\nu}{K}\mathbf{u} = 0, \quad (4.25)$$

where K is the permeability function. Similar to Eq. 4.25 the effect of the solid part can be added to the Navier-Stokes equation (Eq. 4.3) by the Darcy term, leading to the following equation:

$$\frac{\partial\mathbf{u}}{\partial t} - \nu\Delta\mathbf{u} + (\mathbf{u} \cdot \nabla)\mathbf{u} + \nabla p + \frac{\nu}{K}\mathbf{u} = 0. \quad (4.26)$$

The Darcy term vanishes in regions with high permeability, i.e., inside the fluid domain, resembling the Stokes equation. Still, when K is very small, i.e., inside the solid part, it dominates the flow and acts like a barrier. To avoid numerical perturbation for switching between these 2 regions, a Heaviside function is defined to update K [129]:

$$H(\phi) = \begin{cases} 0, & \phi < -\varepsilon \\ \frac{1}{2} + \frac{\phi}{2\varepsilon} + \frac{1}{2\pi} \sin\left(\frac{\pi\phi}{\varepsilon}\right), & -\varepsilon < \phi < \varepsilon \\ 1, & \phi > \varepsilon \end{cases} \quad (4.27)$$

in which ϕ is the level-set signed distance function used to separate the solid and solution parts (Eqs. 3.3 and 3.4), and ε is set to $1.5h$, with h being the minimum mesh element size. Then, K can be accordingly updated to have a smooth transition between regions with a big difference in permeability:

$$K(\mathbf{x}) = 10^{30}(1 - H) + K_0H \quad (4.28)$$

where K_0 is the permeability of metals in fluid regions ($\sim 10^{-6}$ H/m).

4.2.7 Simulation setup

Test case to compare with OpenFOAM

In order to perform a verification analysis on the developed CFD model, a case of 3D flow inside a chamber was implemented to compare the simulation results with those of a well-established and known CFD solver. For this reason, the OpenFOAM open-source solver was used, which has been extensively used for fluid dynamics simulations over the last decades [130]. The simulation was carried out using the simpleFOAM solver, which uses the SIMPLE (Semi-Implicit Method for Pressure Linked Equations) algorithm for coupling and solving the Navier-Stokes equations.

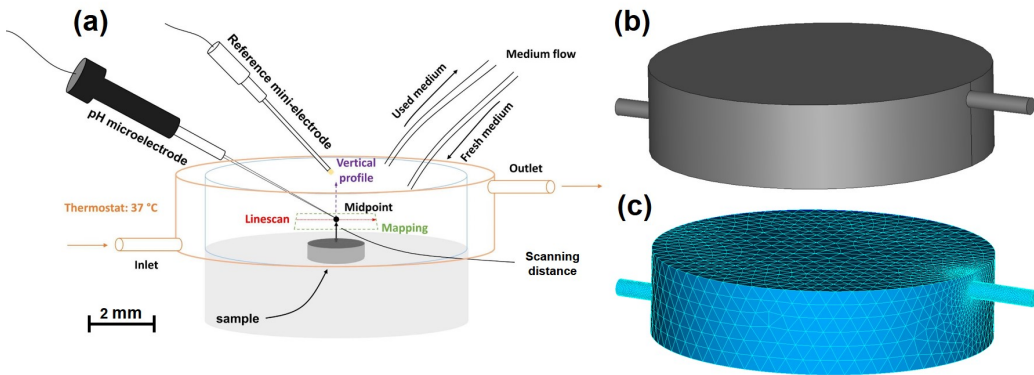


Figure 4.1: Fluid flow model construction for comparing the CFD results with the experimental setup: a) a schematic of the experimental setup, b) the CAD geometry, c) the generated mesh containing tetrahedral elements.

The geometry was chosen based on the experiments performed for biodegradation in hydrodynamics conditions. The experimental setup is depicted in Fig. 4.1-A, where the constructed CAD geometry is shown in Fig. 4.1-B. The computational mesh, comprising linear tetrahedral elements, was generated

using Netgen [91] in the SALOME platform [92]. The final mesh used in both FreeFEM and OpenFOAM models is shown in Fig. 4.1-C, containing 100,888 elements.

The fluid flow direction is from left to right, meaning that the inlet was set on the vertical face of the small pipe on the bottom left side of the chamber, and the outlet was set similarly on the upper right pipe. The rest of the boundaries were set to no-slip boundary conditions. A zero pressure boundary condition was set on the outlet. The inlet velocity was set to 1.0mm/s, and the parameter ν was set to 0.85mm²/s.

Test case to check coupling with degradation model

In addition to the test case for verification of the developed CFD code, two more cases were constructed to evaluate the model's performance in the presence of a barrier, i.e., the degrading object in the coupled biodegradation model. To this end, after coupling the models, a simple 3D geometry of a cylinder with an embedded sphere as the degrading object inside was simulated. The simulation parameters were set similarly to the verification case. The inlet and outlet were assigned to the bases of the cylinder, and the altitude was assigned as the wall boundary condition. Fig. 4.2 shows a schematic of the computational setup for this test case as well as a vertical cut of the generated computational mesh containing 640,249 elements. The mesh was refined on the interface of the degrading object to increase the numerical accuracy of the biodegradation model.

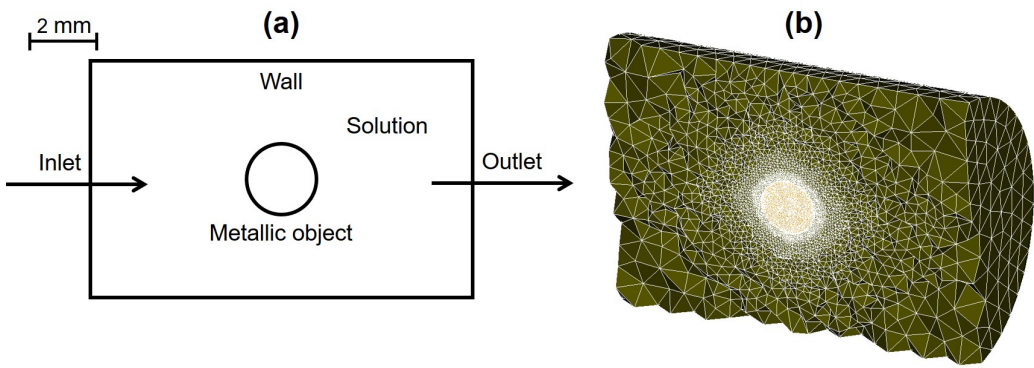


Figure 4.2: Model construction for checking the coupling of the fluid flow and biodegradation models: a) schematic representation of the domain b) the generated computational mesh.

Additionally, a simple 2D representation of the full chamber model (Fig.

4.1) was constructed to test the effect of the fluid flow on the degradation behavior of the metallic parts. In this model, a high inlet velocity and a high diffusion coefficient were used to have an exaggerated degradation, showing how the fluid flow would affect the change of morphology of the object. The degrading metallic part was selected to be a small rectangle on the bottom of the chamber. The domain setup is depicted schematically in Fig. 4.3. The computational mesh was generated using the SALOME platform and contained 24,946 elements.

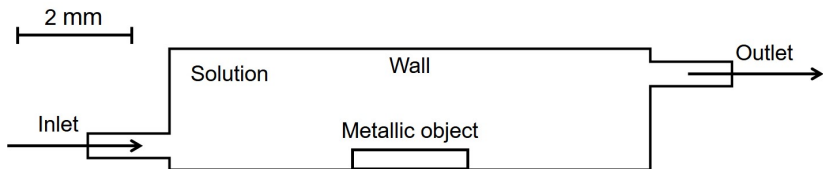


Figure 4.3: Schematic view of the model used for checking the effect of the fluid flow on biodegradation behavior.

4.3 Results

To verify the robustness of the model predictions, the results of the CFD code developed in FreeFEM were compared both quantitatively and qualitatively with an OpenFOAM model of an identical set-up. The qualitative comparison was made via the streamlines, showing how the flow develops by plotting the trajectory lines of the fluid velocity field inside the desired domain, which is the chamber in this case. Figs. 4.4 and 4.5 show such comparison between the developed model and OpenFOAM. Fig. 4.4 shows the streamlines for both models from a side view, in which the flow enters the chamber from the left inlet pipe and leaves it from the top right outlet. The qualitative comparison shows a good agreement between the predictions of the models.

Similarly, Fig. 4.5 depicts a comparison but from the top view, showing good agreement between the predictions, although the OpenFOAM model (bottom) shows slightly better performance on the boundaries as can be appreciated from the existence of extra streamlines close to the cylinder boundary in the FreeFEM code results.

Moreover, a quantitative comparison is possible by comparing the numerical values predicted by the models in various regions of the desired domain, including the regions close to the boundaries. Fig. 4.6 shows the comparison

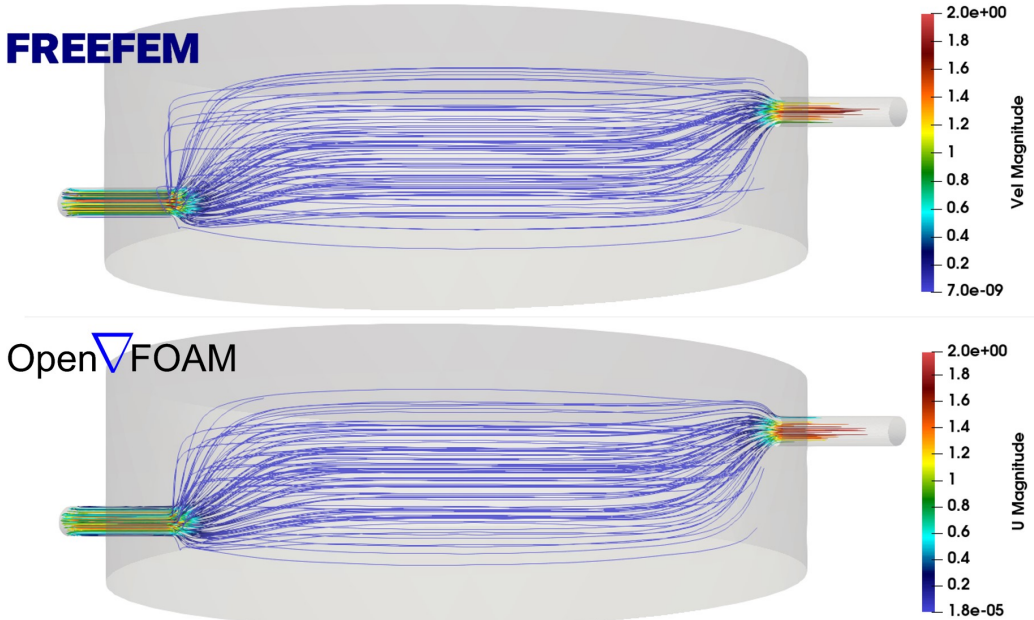


Figure 4.4: Comparing the results of the developed CFD model (top) with OpenFOAM (bottom) via plotting the streamlines of the fluid velocity field, depicted from the side view. The colors on the trajectory lines show the magnitude of the velocity vector (in mm/s).

of the fluid velocity field visualization between the developed CFD code and OpenFOAM on a cross-section in the center of the chamber, showing that both models produce the same results quantitatively.

A closer look at the center of Fig. 4.6 is depicted in Fig. 4.7, where the color bar range is adapted to contain only the visible values. This zoomed-in comparison confirms the good agreement between the CFD model and OpenFOAM results. The employed mesh is relatively coarse in the center (regions far from the inlet and outlet), the effect of which can be seen as non-smooth velocity profiles in Fig. 4.7. Still, both models handle this coarse mesh effect similarly.

Fig. 4.8 shows the result of a proof-of-concept simulation in which the biodegradation model [131] (presented in Chapter 3) is coupled with the fluid flow model. This was done by solving Eq. 4.26 (or Eq. 4.25 for simpler cases) and adding a convection term to the equations of the biodegradation model to include the directional effect of fluid flow on the degrading object. The interplay between the fluid flow and the degradation can be seen in Fig. 4.8 with the released ions being advected to the right (the direction of the fluid

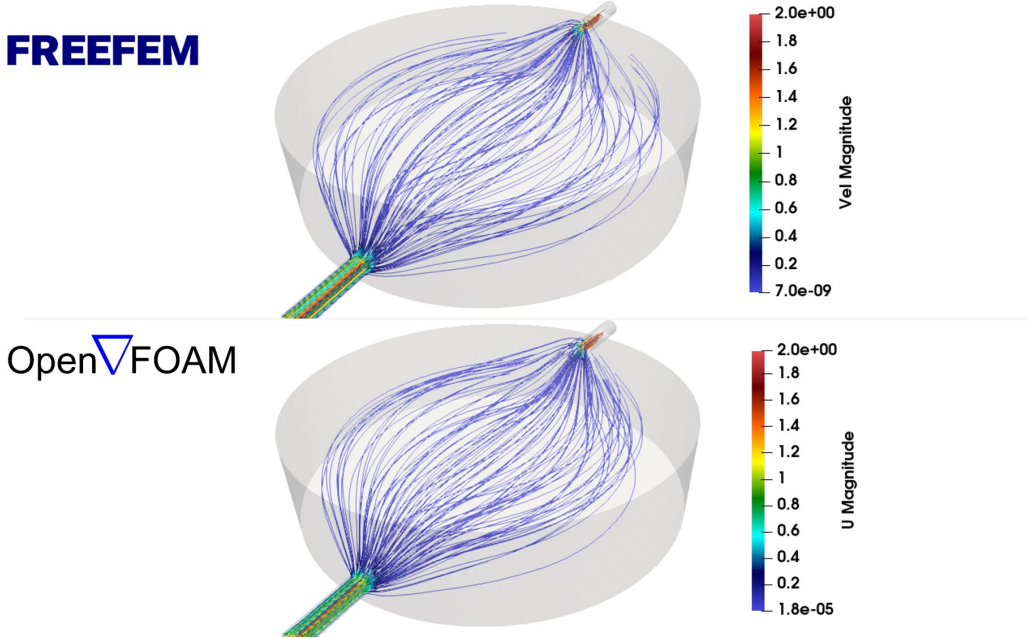


Figure 4.5: Streamlines of the fluid velocity field plotted from a top view to compare the output of the developed CFD model (top) and OpenFOAM (bottom) with colors showing the magnitude of the velocity vector at each point (in mm/s).

flow) and the degrading object being slightly more degraded on the left.

Fig. 4.9 shows the effect of the degrading object on the fluid velocity field, depicted as streamlines passing over the solid part at the end of the performed simulation. The figure demonstrates the fluid flow response to the presence of the changing morphology of the obstacle, obtained from solving the Navier-Stokes equations containing the Darcy term (Eq. 4.26).

Fig. 4.10 shows the results of the second test case for the coupled biodegradation model, in which the release of metallic ions is depicted over time along with the change of the morphology of the degrading object. The released metallic ions get convected in the direction of the flow field inside the chamber, which was obtained by solving the Navier-Stokes equations.

4.4 Discussion

In this study, a parallel fluid flow model was developed to be coupled with the computational biodegradation model enabling the consideration of the effect of the hydrodynamics conditions in corrosion tests. The most important

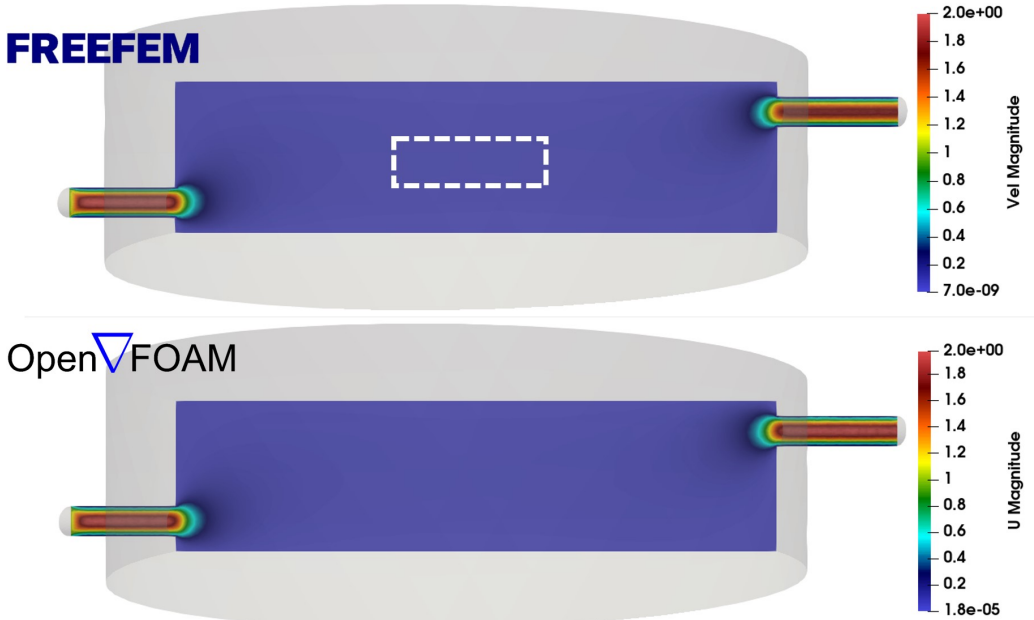


Figure 4.6: comparison between the fluid velocity field predicted by the developed CFD code (top) and OpenFOAM (bottom), depicted on a vertical cross-section in the center of the chamber. Fluid enters the chamber from the left and leaves it from the right. The colors show the magnitude of the velocity vector at each point (in mm/s). The white dashed-line box shows the zoomed-in area of Fig. 4.7.

form of hydrodynamics in tissue engineering is the perfusion phenomenon in bioreactors, which makes the development of such coupled degradation-CFD model even more crucial considering the final application of the biodegradation model. Similar to perfusion bioreactors, the hydrodynamics set-up in biodegradation tests helps removing corrosion products and providing mechanical forces if applicable.

In order to verify the developed CFD model, a test case was prepared to simulate a similar chamber flow model in both the in-house FreeFEM code and the OpenFOAM code, a well-established open-source CFD solver. Qualitative (Figs. 4.4 and 4.5) and quantitative (Figs. 4.6 and 4.7) comparison of results show identical predictions for the flow field in both models, demonstrating that the derivation of the weak forms of Navier-Stokes equations as well as their numerical implementation in FreeFEM were performed correctly. This comparison indicates that the developed code can be used instead of a well-known and sophisticated CFD solver for the desired flow

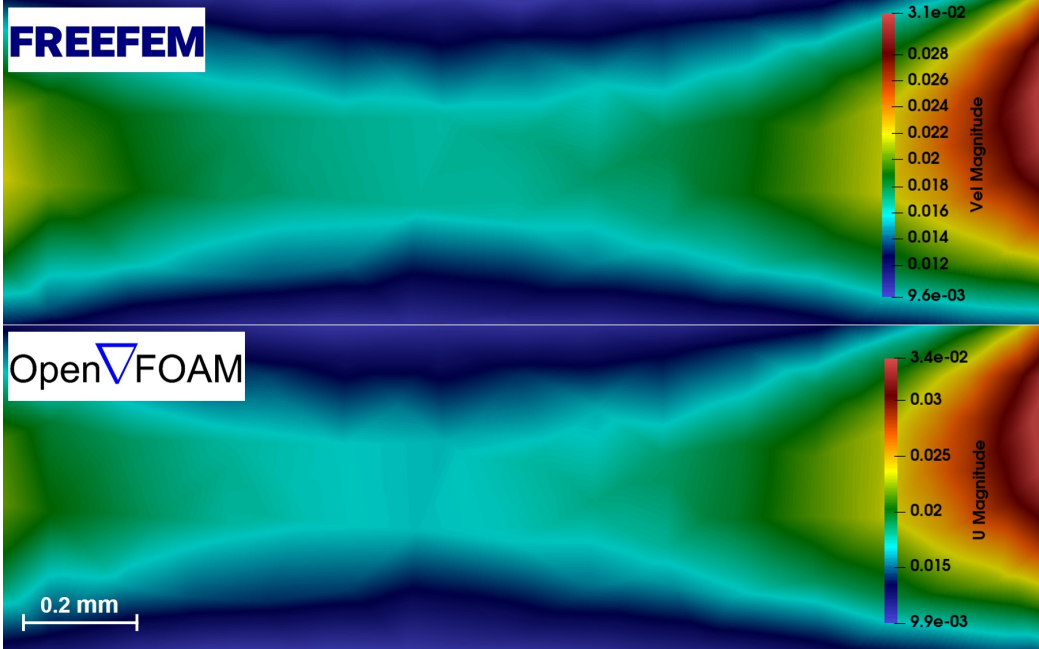


Figure 4.7: A zoomed-in view of the area depicted as white dashed-line in Fig. 4.6, indicating the fluid velocity field for results predicted by the developed CFD code (top) and OpenFOAM (bottom) with colors showing the magnitude of the velocity vector at each point (in mm/s).

regime, which is laminar flow with low Reynolds numbers.

The reason for developing an in-house CFD code instead of using a well-established CFD solver lies in the lack of availability of proper coupling software. Although various efficient solver coupling codes exist and are widely used in similar scenarios (such as the preCISE coupling library [132]), at the time of this writing and to the best of the authors' knowledge, there is no compatible coupling software for FreeFEM, the language in which the computational model of the biodegradation process was implemented. In case of existence, the computational biodegradation model could have been linked with OpenFOAM, SU2, or Code_Saturne in an efficient in-memory way. But, with such an approach not available, the only feasible approach would be coupling the models using disk IO (input-output), meaning that in each time step, the computational model should write the domain data on disk (we should notice that the domain evolves since it is a moving interface problem), and the CFD code reads the data, computes the flow field, and writes it back to the disk so that the biodegradation would read it back. Despite the possibility of employing this approach, the computationally in-

tensive aspects of the models, which is the result of a 3D mesh refined on the corrosion interface leading to normally 2M-4M elements, makes the workflow dramatically inefficient. Working in HPC environments and dealing with a partitioned mesh can make the situation even more complex. This reasoning made it inevitable to develop an in-house CFD code so that it can be seamlessly and efficiently coupled with other models.

In order to couple the flow model with the computational biodegradation model, both models should be modified to include the effect of the other one. For the biodegradation model, the effect of fluid flow was considered as an extra convection term in the set of derived reaction-diffusion equations, which can be implemented using the method of characteristics in FreeFEM. On the other side, the inclusion of the effect of a degrading object can be more tricky in the CFD model. This was done by adding a Darcy term to the Navier-Stokes and Stokes equation, which considers a high permeability for the regions inside the degrading object, preventing fluid from penetrating into those parts. After the degrading part interface shrinks, the Darcy term gets updated automatically since it is formulated based on the level-set function used in the biodegradation model to describe the moving corrosion interface. Figs. 4.8 and 4.9 demonstrate the effect of the presence of the degrading part on the pattern of flow, while Fig. 4.10 shows the effect of fluid flow on the biodegradation, which is the ions being convected in the direction of the fluid velocity field, leading to a minor directional degradation in which the side facing the flow direction degrades slightly faster.

The performed verification study on the developed CFD code is not enough to call it a fully validated fluid flow model. However, by considering the desired flow regime in biodegradation tests, the verification shows that the coupled model is capable of predicting acceptable and correct results. Nonetheless, dedicated validation tests can be further done to fully validate the developed model as a general CFD code which can be used standalone for simulating laminar flows with low Reynolds numbers.

4.5 Conclusion

In this chapter, a parallel fluid flow model was developed and linked with the biodegradation model, making it possible to simulate the degradation process in hydrodynamics conditions. Proper preconditioners and solvers were selected to improve the parallel efficiency of the developed model in HPC environments. The results obtained from the fluid flow model were compared with the output of a similar simulation performed using OpenFOAM, in which a good agreement was observed, verifying the performance

of the developed model for the desired flow regime needed to perform local pH simulations in Chapter 5.

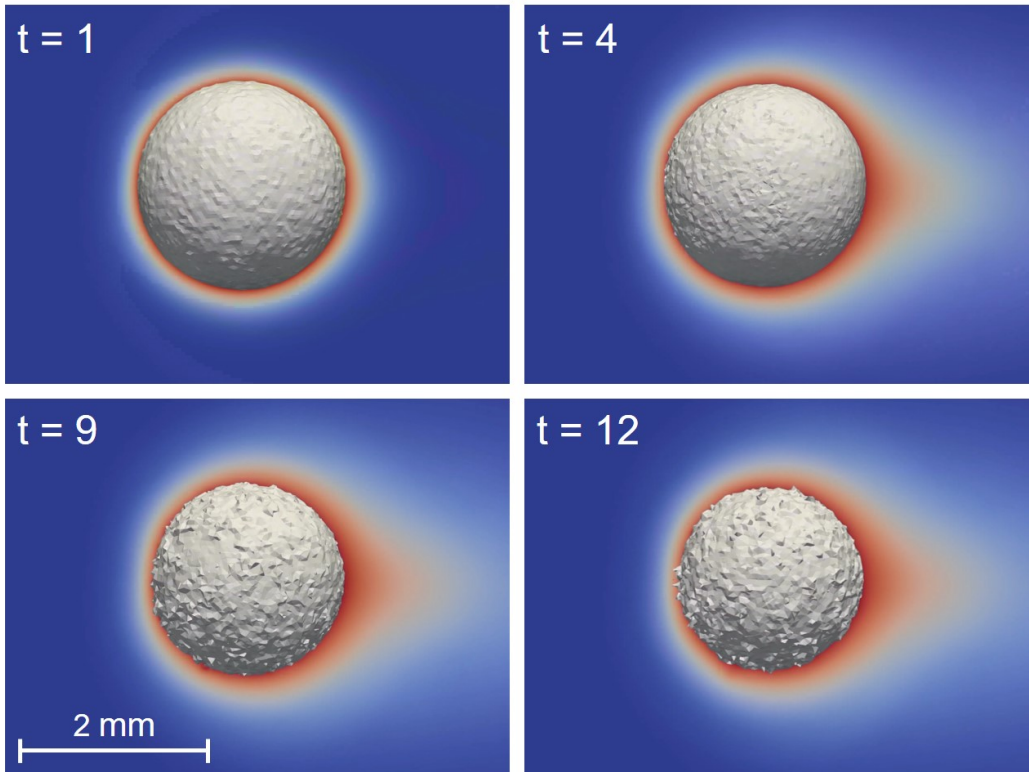


Figure 4.8: Biodegradation simulation results in the presence of fluid flow over time, showing the interplay between the fluid flow and biodegradation models. The displayed time is in an arbitrary unit for demonstrating the intervals only. The flow gets detoured due to the presence of an obstacle, and the released ions get advected to the direction of fluid flow (left to right). The colors represent the concentration of Mg ions as they get released to the surrounding environment and subsequently get diffused/advectioned. The gray surface shows the zero iso-contour of the used level-set function to track the degrading object's interface, demonstrating the solid part's change of morphology.

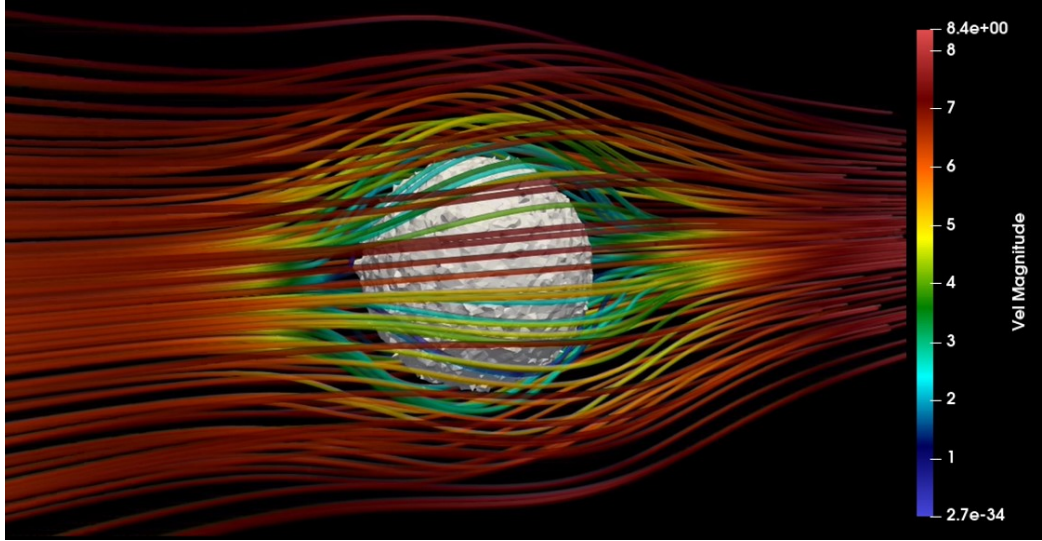


Figure 4.9: Visualization of the fluid velocity field depicted by streamlines passing over a degrading object. Colors show the magnitude of the velocity field (in mm/s) projected on the streamlines.

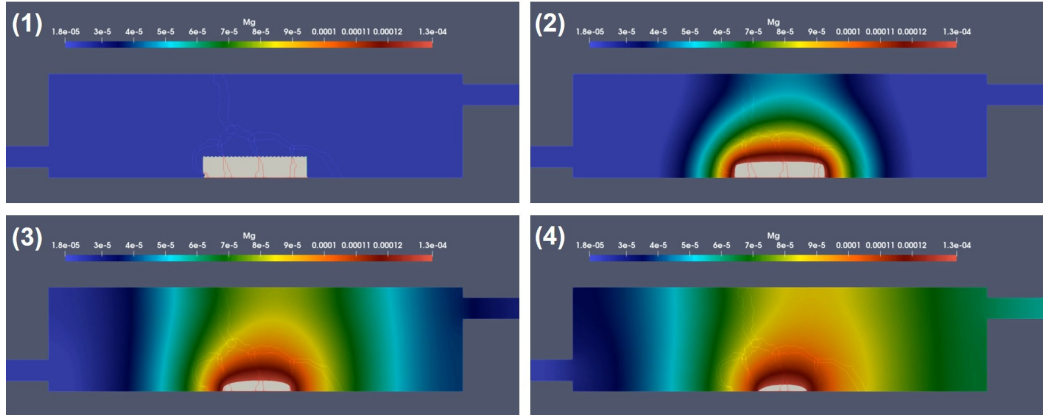


Figure 4.10: Visualization of the results of the biodegradation of an object inside the chamber in hydrodynamics conditions. Colors show the concentration of released metal ions getting convected in the direction of fluid flow. The light gray part shows the degrading object. The numbers (1) to (4) demonstrate the evolution of the simulation over time.

Chapter 5

Extending the model: simulating local pH evolution

This chapter is based on a manuscript prepared to be submitted:
M. Barzegari, C. Wang, S.V. Lamaka, G. Zavodszky, and L. Geris,
“Interface-coupled multiphysics computational modeling of local pH
changes during the biodegradation of magnesium biomaterials.”

In this chapter, the basic biodegradation model developed in Chapter 3 is further developed to capture more advanced chemistry occurring at the corrosion interface in HBSS solutions, making it possible to simulate more complex environments and local pH changes during the biodegradation process.

5.1 Introduction

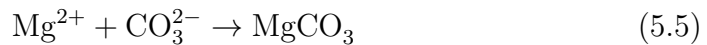
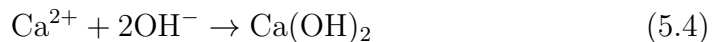
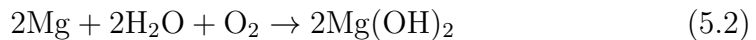
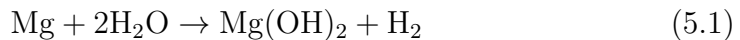
Mg is the most studied biodegradable metal [2,3,71,133], on which many research groups have performed valuable biodegradation studies [11,134–136]. The biodegradation behavior of Mg is investigated in *in vitro* corrosion tests, in which the selection of the corrosive media plays an important role since it affects the underlying chemical reactions [35]. By considering the main application of the biomaterial, which can be tissue engineering scaffolds, vascular stents, or orthopedic fixation implants, the corrosive media can be selected to be a representative of the service environment. The most basic form of the medium is a saline (NaCl) solution, in which the degradation rate is the highest possible [35]. More complex solutions can be used to mimic the behavior of the body environment by taking into account additional body fluid com-

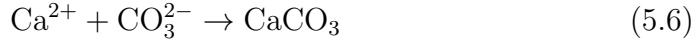
ponents, the most popular of which are Ringer's solution, PBS (phosphate buffered saline), SBFs (simulated body fluids), HBSS (Hank's balanced salt solution), and Earle's balanced salt solution (EBSS) [35]. Adding more organic components to the solution will make it ready to simulate cell culture conditions. The common media for this purpose are MEM (Minimum Essential medium) and DMEM (Dulbecco's modified Eagle's medium) [35].

Various studies have already investigated the effect of different components in the aforementioned corrosive media on the degradation behavior of Mg materials [36–40]. A typical composition of "simulated body fluid" solutions (such as SBF, HBSS, and EBSS) is chloride, carbonate, phosphates, sulfate, and calcium. The individual effect of these components on the rate of degradation of Mg has been extensively studied, in which it has been observed that carbonate and phosphate slow down the rate while the effect of sulfate is negligible [38, 40]. The concentration of HCO_3^- affects the pH buffering capacity and the degradation rate of Mg simultaneously [47].

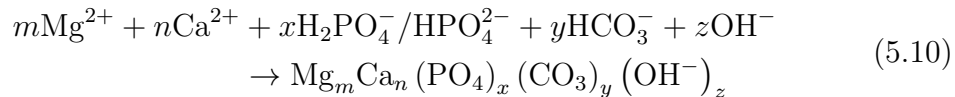
The effect of calcium ions is more complex because it has been found that Ca^{2+} doesn't contribute to the Mg corrosion directly [7], but a mixed effect of Ca^{2+} , Mg^{2+} , HCO_3^- , and $\text{H}_2\text{PO}_4^-/\text{HPO}_4^{2-}$ forms a co-precipitation layer on the corroded surface of Mg, slowing down the corrosion rate of commercially pure Mg as well as of some Mg alloys [36, 39]. It has also been reported that although various Mg alloys show different intrinsic degradation behavior in NaCl solution, they possibly behave similarly in simulated body fluids [40, 137]. Since the humoral regulations inside the human body control the changes in pH of body fluids, it is common to use pH buffers to mimic a similar condition, but it should be taken into account that buffering solutions may affect the degradation rate of Mg [138, 139] and may also delay the formation of the precipitate layer [39]. An alternative solution to address this issue is to use natural pH buffers such as $\text{HCO}_3^-/\text{CO}_2$, an option that is commonly used for immersion tests under cell culture conditions. In this situation, an equilibrium between H_2CO_3 (CO_2), HCO_3^- , and CO_3^{2-} keeps the pH constant. As a result, using simulated body fluids for corrosion tests without additional synthetic pH buffers is still acceptable [39, 40].

The major reactions occurring in simulated body fluids can be written as:





The protection layer is formed on the corroded surface as a hydroxyapatite-like precipitation according to the following reaction [44, 82, 140, 141]:



In fact, the similarity in corrosion behavior of various Mg alloys in SBF solutions is due to the similar composition of this quasi-protective layer, a mechanism that doesn't occur in NaCl solution, leading to a more apparent difference in degradation rate between Mg alloys. The composition of the formed hydroxyapatite-like precipitation layer is close to the ones found *in vivo* [35]. Additionally, local pH measurements in HBSS and SBF show that, in contrast to saline solutions, the local pH value is not alkaline [39, 142]. This has been reported for hydrodynamics situations, under which the medium composition is kept constant by replacing the consumed ions by means of fluid flow.

Building mathematical and computational models of the biodegradation process in complex buffered solutions can help save the resources required to perform *in vitro* tests, but the details of the aforementioned chemistry are challenging to capture in a mechanistic model. Few attempts have been made to model the underlying chemical reactions in SBF solutions [100, 143, 144], but due to the complexity of the resulting mathematical models, it is not feasible to extend them to 3D and real-world cases, like for simulation of the degradation of biomedical implants. In the case of data-driven approaches [145], the applicability is limited to the studied conditions, making it difficult for developed models to achieve high extensibility and generalizability.

In this chapter, a detailed mathematical model is presented to extend the work discussed in Chapter 3 and [131], in which a mechanistic model of the biodegradation process is coupled with a thermodynamics-based code to predict local interfacial biodegradation of Mg in HBSS solutions. The local pH changes are the validation criterion to compare the simulation results with experimental ones. Besides other parameters affecting the Mg biodegradation mechanism, monitoring the pH changes at the degradation interface has proved to be significant due to its direct effect on the formation and stability of the degradation products layer [146].

Table 5.1: The elemental composition of ultra-high pure and commercial pure Mg used for performing corrosion experiments (percentages)

| | Fe | Si | Mn | Al | Cu | Ni |
|--------|---------|---------|---------|---------|---------|---------|
| CP-Mg | 0.03420 | 0.0001 | 0.00237 | 0.00402 | 0.00037 | <0.0002 |
| UHP-Mg | 0.0012 | <0.0001 | 0.00037 | 0.00291 | <0.0001 | <0.0002 |

5.2 Methods

5.2.1 Experimental setup

In this study, the corrosion tests were performed on ultra-high pure (UHP) and commercially pure (CP) Mg in hydrodynamics conditions. The elemental composition of the used materials is shown in Table 5.1, measured by Atomic Absorption Spectrometer (AAS). The samples were prepared as rod shapes with a diameter of 2mm mounted in epoxy resin with a disc shape. The electrolyte used for corrosion tests was commercial HBSS (ThermoFisher Scientific, no. 14025100), the composition of which is presented in Table 5.2.

Table 5.2: Chemical composition of the HBSS electrolytes used to perform corrosion tests for local pH measurements.

| Components | mM |
|---------------------------------------|-------|
| KCl | 5.33 |
| KH ₂ PO ₄ | 0.44 |
| NaHCO ₃ | 4.17 |
| NaCl | 137.9 |
| Na ₂ HPO ₄ | 0.34 |
| CaCl ₂ | 1.26 |
| MgCl ₂ · 6H ₂ O | 0.49 |
| MgSO ₄ · 7H ₂ O | 0.41 |
| D – Glucose | 5.56 |

Local pH measurements were performed using a glass-type pH microelectrode with a tip diameter of 10 μm (Unisense, pH-10). The electrode was positioned above the sample at a distance of $50 \pm 3\mu\text{m}$. At this distance, a line scan mapping routine was performed to obtain the horizontal pH profiles, in which a specimen-centered area ($3000 \times 3000\mu\text{m}$, which was used as the simulation domain as well) was mapped with the step length of 100 μm . The sampling interval was 3 s, the result of which was a total duration of approximately 1 hour to scan the area. Similarly, the vertical pH profiles were

scanned starting at the height of $50\mu\text{m}$ above the midpoint of the specimen up to $500\mu\text{m}$ in the bulk medium. Fig. 5.1 demonstrates the setup of the experiment schematically, in which the flow enters the chamber from the left with a rate of $1.0\text{mL}\cdot\text{min}^{-1}$ (Medorex TL15E peristaltic pump) and leaves it to the right. The tests were performed independently at room temperature (RT, 22 ± 2 in an air-conditioned lab) and 37°C (Thermo Scientific SAHARA S13).

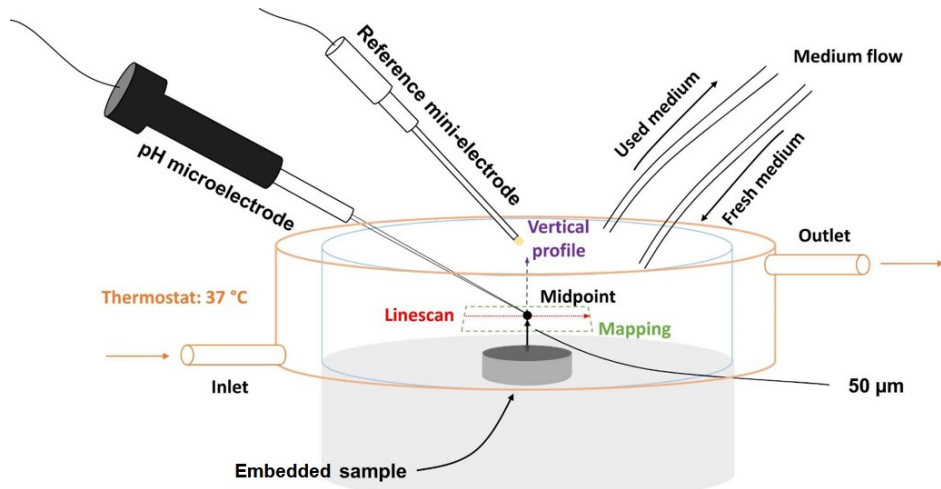


Figure 5.1: Experimental setup for validating the coupled biodegradation model

The *in vitro* cross-section morphology of the specimens was characterized using a dual beam FIB/SEM platform (LYRA3 TESCAN) equipped with an EDX system (Oxford Inca with a silicon drift detector), the result of which was used to compare qualitatively with the simulation predictions.

5.2.2 Computational model construction

The computational model in the current study comprises three coupled modules:

1. An extended version of the mechanistic biodegradation model based on our previous work [131] (Chapter 3) to obtain Mg and hydroxide ions distributions and the initial formation of the protective layer based on the modeling hypotheses.
2. A thermodynamics-based simulation to estimate the concentration of various components of the electrolyte in regions close to the surface of the sample based on the calculated pH of module 1.

3. A module to link the former two, calculating the hydroxyapatite-like precipitation concentration, in which calculated pH values were transferred from module 1 to module 2 for each node of the computational mesh to calculate the concentration of ions depending on the computed local pH and transfer back the calculated precipitation concentration to module 1.

Fig. 5.2 shows a schematic representation of the coupled modules and the way that simulation data are being transferred between them. It should be noted that the results obtained from module 2 are calculated in an equilibrium state as it is a thermodynamics-based code, but module 1 works based on kinetics equations and calculations. As a result, it is assumed that the kinetics of the reactions is affected by the equilibrium state of involved chemical components in each time step, which can be considered as a small time window in which the chemical species are in equilibrium. This fact should be seen as an assumption made for simplifying the calculation of the stoichiometry of the protective layer (Eq. 5.10), in which the effect of the underlying kinetics on the change of pH is neglected.

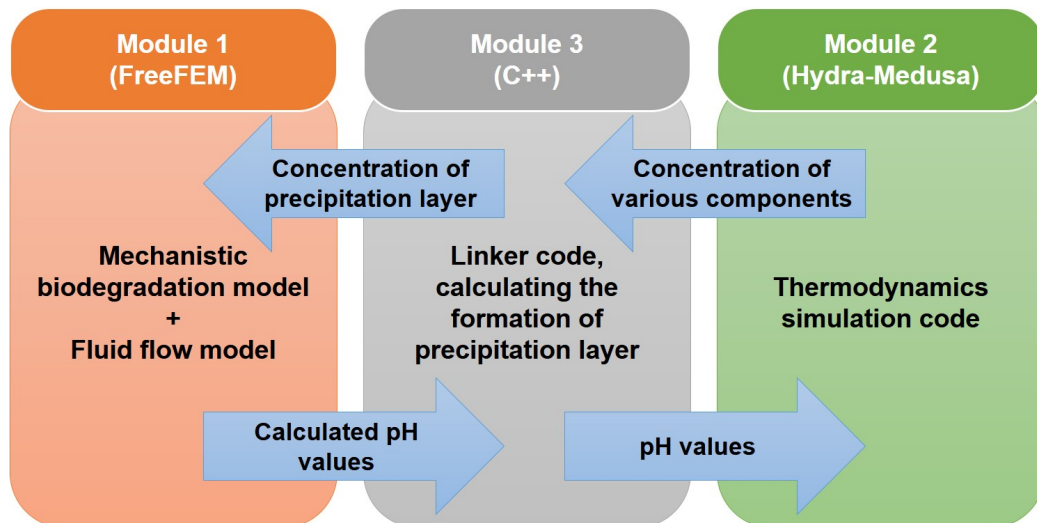
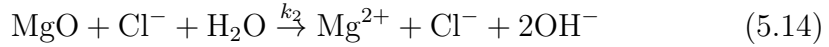
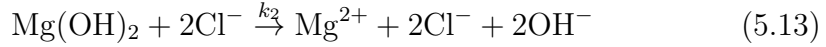
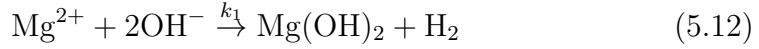
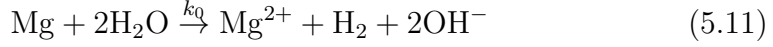


Figure 5.2: Schematic representation of the coupled modules for modeling of local pH changes, showing how they are connected as well as the programming languages and tools used for the implementation.

The computational biodegradation model (module 1) was developed by deriving a set of reaction-diffusion-advection equations from the chemistry of the corrosion of Mg in hydrodynamics conditions. The following basic reactions are captured by this model, which is an extension of our previous

contribution [131] (Chapter 3) as the overall process is described in more detailed equations:



The following state variables hold the concentration of various basic ions involved in reactions described by Eqs. 5.11, 5.12, 5.13, and 5.14:

$$\begin{aligned} C_{\text{Mg}} &= C_{\text{Mg}}(\mathbf{x}, t), & C_{\text{Mg}_{[\text{s}]}} &= C_{\text{Mg}_{[\text{s}]}}(\mathbf{x}, t), & C_{\text{Mg}(\text{OH})_2} &= C_{\text{Mg}(\text{OH})_2}(\mathbf{x}, t) \\ C_{\text{Cl}} &= C_{\text{Cl}}(\mathbf{x}, t), & C_{\text{OH}} &= C_{\text{OH}}(\mathbf{x}, t) & \mathbf{x} \in \Omega \subset \mathbb{R}^3 \end{aligned}, \quad (5.15)$$

Additionally, two more state variables are needed to couple the models, representing the calculated concentration of the hydroxyapatite-like precipitation as well as the cumulative layer concentration:

$$C_{\text{Hydrox}} = C_{\text{Hydrox}}(\mathbf{x}, t), \quad C_{\text{Film}} = C_{\text{Film}}(\mathbf{x}, t) \quad \mathbf{x} \in \Omega \subset \mathbb{R}^3, \quad (5.16)$$

where the total film concentration can be calculated as:

$$C_{\text{Film}} = C_{\text{Hydrox}} + C_{\text{Mg}(\text{OH})_2}. \quad (5.17)$$

With the above state variables defined, the biodegradation model can be constructed by implementing the following PDEs:

$$\frac{\partial C_{\text{Mg}_{[\text{s}]}}}{\partial t} = -k_0 C_{\text{Mg}_{[\text{s}]}} \quad (5.18)$$

$$\frac{\partial C_{\text{Mg}}}{\partial t} = \nabla \cdot (D_{\text{Mg}}^e \nabla C_{\text{Mg}}) - \nabla \cdot (\mathbf{u} C_{\text{Mg}}) + k_0 C_{\text{Mg}_{[\text{s}]}} - k_1 \alpha C_{\text{Mg}} C_{\text{OH}}^2 + k_2 C_{\text{Film}} C_{\text{Cl}}^2 \quad (5.19)$$

$$\frac{\partial C_{\text{Mg}(\text{OH})_2}}{\partial t} = k_1 \alpha C_{\text{Mg}} C_{\text{OH}}^2 - k_2 C_{\text{Film}} C_{\text{Cl}}^2 \quad (5.20)$$

$$\frac{\partial C_{\text{Cl}}}{\partial t} = \nabla \cdot (D_{\text{Cl}}^e \nabla C_{\text{Cl}}) - \nabla \cdot (\mathbf{u} C_{\text{Cl}}) \quad (5.21)$$

$$\frac{\partial C_{\text{OH}}}{\partial t} = \nabla \cdot (D_{\text{OH}}^e \nabla C_{\text{OH}}) - \nabla \cdot (\mathbf{u} C_{\text{OH}}) + k_0 C_{\text{Mg}_{[\text{s}]}} - k_1 \alpha C_{\text{Mg}} C_{\text{OH}}^2 + k_2 C_{\text{Film}} C_{\text{Cl}}^2 \quad (5.22)$$

showing the mathematical representation of reactions 5.11, 5.12, 5.13, and 5.14 in hydrodynamics condition in the form of a set of reaction-diffusion-advection equations. k_0 , k_1 , and k_2 are reaction rate constants corresponding to the Mg oxidation, film formation, and film elimination reactions, respectively. In Eqs. 5.19, 5.20, and 5.22, α is defined as:

$$\alpha = \left(1 - \beta \frac{C_{\text{Film}}}{[\text{Film}]_{\max}}\right), \quad (5.23)$$

in which the protective film maximum concentration is calculated using its porosity (ϵ) [68]:

$$[\text{Film}]_{\max} = \rho_{\text{Film}} \times (1 - \epsilon). \quad (5.24)$$

In Eqs. 5.19, 5.21, and 5.22, \mathbf{u} is the velocity field from the surrounding fluid flow governed by the Stokes equation:

$$\begin{cases} -\nu \Delta \mathbf{u} + \nabla p + \frac{\nu}{K} \mathbf{u} = 0 \\ \nabla \cdot \mathbf{u} + \varepsilon p = 0. \end{cases} \quad (5.25)$$

in which \mathbf{u} is the fluid velocity, p is the pressure (which is actually pressure divided by the density), $\nu = \frac{\mu}{\rho}$ is the kinematic viscosity (with μ being the dynamic viscosity), and K is the permeability function.

The local pH can be calculated using the simulated concentration of hydroxide (Eq. 5.22):

$$\text{pH} = 14 + \log_{10} (C_{\text{OH}}/\text{MW}_{\text{OH}} \times 10^6), \quad (5.26)$$

with $\text{MW}_{\text{OH}} = 17.01$ being the molecular weight (MW) of the hydroxide ions.

The concentration of the hydroxyapatite-like precipitation (C_{Hydrox} in Eqs. 5.15 and 5.17) is calculated using the thermodynamics-based simulations (module 2) based on calculated local pH (Eq. 5.26) for each node of the desired domain. After solving the derived equations in each time step, the linking module passes the obtained local pH to the thermodynamics module to calculate the individual concentration of involved chemical components. Then, the individual concentrations are converted to the concentration of the hydroxyapatite-like precipitation by taking into account the stoichiometry of the formation reaction (Eq. 5.10), leading to the calculation of C_{Hydrox} for each node. After this, the total concentration of the film can be calculated according to Eq. 5.17 by passing back the calculated value to module 1.

The thermodynamics-based simulations were conducted using the Hydra-Medusa code [147–149], in which the input data of chemical equilibrium constants, solubility products, temperature, and involved chemical components

are used to generate a set of equilibrium diagrams correlating pH to concentration or fraction of desired chemical components. The experimental conditions, including the initial composition of the electrolyte (Table 5.2) and evaluated temperatures (25°C and 37°C), were given as input, and contributing components and solubility products were selected as represented in Table 5.3.

Table 5.3: Solubility products of related chemical reactions at 25°C (RT) and 37°C [150]

| Chemical reaction | $pK_{sp} 25^{\circ}\text{C}$ | $pK_{sp} 37^{\circ}\text{C}$ |
|---|------------------------------|------------------------------|
| $\text{Ca}_5(\text{PO}_4)_3\text{OH} \rightarrow 5\text{Ca}^{2+} + 3\text{PO}_4^{3-} + \text{OH}^-$ | 54.46 | 58.77 |
| $\text{Mg}(\text{OH})_2 \rightarrow \text{Mg}^{2+} + 2\text{OH}^-$ | 11.25 | 11.25 |
| $\text{Ca}(\text{OH})_2 \rightarrow \text{Ca}^{2+} + 2\text{OH}^-$ | 5.20 | 5.38 |
| $\text{MgCO}_3 \rightarrow \text{Mg}^{2+} + \text{CO}_3^{2-}$ | 8.03 | 5.51 |
| $\text{CaCO}_3 \rightarrow \text{Ca}^{2+} + \text{CO}_3^{2-}$ | 8.48 | 8.44 |
| $\text{Mg}_3(\text{PO}_4)_2 \rightarrow 3\text{Mg}^{2+} + 2\text{PO}_4^{3-}$ | 23.28 | 27.62 |
| $\text{H}_2\text{O(l)} \rightarrow \text{H}^+(aq) + \text{OH}^-(aq)$ | 14.00 | 13.61 |
| $\text{HCO}_3^-(aq) \rightarrow \text{CO}_3^{2-}(aq) + \text{H}^+(aq)$ | 10.33 | 10.24 |
| $\text{HPO}_4^{2-}(aq) \rightarrow \text{PO}_4^{3-}(aq) + \text{H}^+(aq)$ | 12.35 | 12.32 |

The derived PDEs for the mechanistic model (Eqs. 5.19, 5.20, 5.21, and 5.22) were solved using a standard first-order finite element scheme. The open-source PDE solver FreeFEM [86] was used to implement the finite element model, resulting in a linear system of equations. The obtained equations were solved in parallel using efficient preconditioners and iterative solvers available in the open-source high-performance computing (HPC) toolkit PETSc [89]. The HYPRE BoomerAMG [87] and FieldSplit preconditioners were applied to the reaction-diffusion PDEs and the Stokes equations, respectively, and the GMRES solver [88] was used to solve the linear systems. Moreover, the computational mesh was partitioned and distributed among available computing resources using the HPDDM preconditioner [90]. Additionally, a Level-Set-based approach was employed to track the change of morphology of the degrading part, on the solution of which appropriate boundary conditions for the PDEs were applied via the penalization method. The details of this implementation are presented in our published works [131, 151] and Chapters 3 and 7. Since Eq. 5.22 is a non-linear PDE, a Picard-relaxation approach was followed to linearize this equation. The linking module (module 3) was implemented as a FreeFEM plugin in C++.

5.2.3 Simulation setup

Since the objective of the current study is to investigate local pH changes in regions close to the degrading metal, the computational domain was selected to include only a small portion of the chamber used in the experimental setup (Fig. 5.1). The domain was a $3 \times 3 \times 3$ mm cube on top of the degrading object, and the degrading block, represented as a disc with a diameter of 2mm and height of 0.3mm, was attached to the outside of the cube. The cube size was selected such that it represents the sample-centered area used in the experimental setup for line scan mapping. This setup is depicted in Fig. 5.3. The computational mesh was generated using a set of first-order tetrahedral elements, which was adaptively refined on the interface of the degrading sample to increase the numerical accuracy of the employed interface capturing technique. The Netgen mesh engine [91] in the SALOME platform [92] was used to generate the mesh. The generated mesh contained 290,997 elements with 51,757 degrees of freedom (DOF) for each equation.

The boundary conditions include an inlet on the left of the box, an outlet on the right, a wall on the bottom except where the degrading part exists, and a free slip on top. The inlet velocity was selected to be a linear profile ranging from zero on the bottom to $0.01\text{mm}.\text{s}^{-1}$ on the top, a value coming from solving the Navier-Stokes equations in the full chamber model (described in Chapter 4).

The values of model parameters were set based on our previous work [131] (Chapter 3), but the following assumptions were also applied for selecting the proper parameters of the coupled computational model:

1. Diffusion rate of hydroxide ions is 5-10 times more than the rate of Mg ions, so D_{OH} was set as $D_{\text{OH}} = 7.5D_{\text{Mg}}$ [146].
2. The hydroxyapatite-like precipitation does not form immediately at the beginning and emerges later [146, 150]. In the current model, it is set to start forming after the first hour of simulation time.
3. The magnesium hydroxide layer is thicker at 37°C [150], so the film elimination parameter (k_2) was set to be 50 times lower in this temperature in comparison to the room temperate.

The density of the electrolyte was selected to be $1.085 \times 10^{-3}\text{g}.\text{mm}^{-3}$, and the dynamic viscosity was set to $1.28 \times 10^{-3}\text{g}.\text{mm}^{-1}\text{s}^{-1}$. The simulations were carried out on the Snellius supercomputer using 100 CPU cores on a thin node with 256 GB of total memory.

5.3 Results

5.3.1 Thermodynamics-based simulation

Inputting the experimental conditions in the Hydra-Medusa software, including the initial composition of the electrolyte, temperature and the contributing chemical components, results in a big and complex output containing all the possible occurring chemical reactions. From this output, relevant reactions for the current biodegradation systems were filtered out, and the filtered reactions were converted to desired concentration units. Fig. 5.4 depicts the output of this process separately for simulations performed at 25°C (RT) and 37°C, showing how the concentration of relevant components varies with changing the environment pH. The solubility products of these simulations were taken from Table 5.3, and equilibrium concentrations were set to be equal to the electrolyte composition, listed in Table 5.2. These results (module 2) were used by the linking module (module 3) to provide equilibrium information for the mechanistic model (module 1).

5.3.2 Biodegradation simulations

In the current study, the local pH profiles, i.e., the pattern of pH changes in the region close to the degradation surface, were used to validate the developed coupled computational model. The comparison between computational predictions and experimental results was made in 3 different ways: 1) qualitative comparison of pH distribution above the degradable metal in a sample-centered square with an edge size of 3mm, 2) comparing the horizontal pH profiles, where the pH was measured over a line parallel to the sample, and 3) comparing vertical pH profiles, in which the pH was measured over a distance from the surface of the sample to the bulk of the electrolyte.

Fig. 5.5 shows a visualization of the local pH profiles from the top and side views for simulations performed at 25°C (RT) and 37°C after 12 hours. These patterns are comparable with the local pH distribution measured in the experiments, as shown in Fig. 5.6. In these figures, the flow is from left to right, advecting the released ions in the flow direction.

Quantitative profiles provide a more accurate comparison between the computational predictions and experimentally-obtained values. The horizontal profiles, also called line scans, are depicted in Fig. 5.8, in which the local pH changes are plotted over a horizontal line located 50 μm above the surface of the sample. The profiles are shown separately for the experiments performed with CP and UHP Mg and the computational model. The results were recorded after 3, 6, and 12 hours of immersion.

Similarly, Fig. 5.8 shows the vertical pH profile after 12 hours of degradation, which was the final time of the simulation. The local pH is measured over a distance of 0.5mm vertically, starting from 50 μ m above the sample.

5.4 Discussion

In this study, an interface-coupled multiphysics biodegradation model was developed in order to predict the corrosion behavior in simulated body fluids in the presence of various chemical components. The quantity to compare with the experimental results was the predicted local pH, which reflects the capabilities of the model to capture the complex chemistry occurring near the biodegradation interface. For this end, our previous biodegradation model [131] (Chapter 3) was extended and coupled with a fluid flow model capturing the hydrodynamics condition. Then, the coupled model was linked to a thermodynamics-based code for computing the concentration of involved chemical components, the results of which were provided back to the biodegradation model via a linking module to compute the concentration of the precipitation layer.

It has been shown that the local pH changes can be a reflective characteristic of the biodegradation process in SBF-like solutions [146, 150]. Consequently, the vertical and horizontal local pH profiles can be reasonably used for the validation of the computational models of the biodegradation process. Capturing the complex interaction of various chemical components on the biodegradation interface in a mechanistic model can be a big challenge, especially for 3D cases with any arbitrary shape. That's why several modules were coupled in the current study to deliver such a model.

In this work, while the experiments were performed using CP and UHP Mg, the computational model does not take into account the difference in the elemental composition of these materials. Instead, the biodegradation model was developed by ignoring the effect of alloying elements and impurities. There are noticeable quantitative and qualitative variations in the obtained experimental results, such as different behavior of CP and UHP for horizontal pH profiles in line scan mappings (Fig. 5.7) and distribution of local pH above the sample (Fig. 5.6). However, these differences are still roughly the same behavior and quantity, which support the performed assumption and simplification of ignoring the dissimilarity of elemental composition. As a consequence, the computational results, including the pH profiles (Fig. 5.8), line scans (Fig. 5.7), and local pH distributions (Fig. 5.5), lies between the values and profiles obtained for CP and UHP Mg.

Recent studies on measuring local pH changes on the biodegradation sur-

face of Mg alloys show that the local values are different from the pH within the bulk of the electrolyte [146]. For example, in the tests performed by Mareci et al. [152], such observation was made when the vertical pH profiles were compared to the global pH values. Similar behavior was observed in the Wang et al. work [150]. Reproducing this behavior is problematic in mechanistic computational models due to the uniformity of the diffusion of hydroxide ions that change the pH. In other words, a uniform diffusion with a relatively high diffusion coefficient leads to the same local and global pH values. In the model presented here however, spatially dependent behavior was successfully reproduced *in silico* by letting a narrow film form at the beginning of the mechanistic biodegradation simulation and then computing the interaction of various ions in this narrow region by using the coupled thermodynamics-based code. Comparing the results of the predicted vertical pH profiles with the experimentally obtained curves (Fig. 5.8) shows good agreement, implying that the employed approach was able to mimic the complex chemistry on the biodegradation surface from a quantitative point of view. Yet, a different behavior can be observed further away from the surface where the local pH approaches the global value. In experimental results, this happens at a shorter distance from the implant compared to the computational predictions (Fig. 5.8) where yielding to the global pH seems to occur at longer distances from the biodegradation surface. This behavior can be confirmed by the visualization of computed pH (Fig. 5.5) and is due to the uniform diffusion mechanism of ions in the computational model, causing a gradient in the bulk part outside of the narrow formed region.

The results of horizontal line scan mapping on the surface of the sample and local pH distribution (Figs. 5.7 and 5.6) show that the pH starts to change in regions above the sample. In the computational predictions depicted in Fig. 5.7, the change of pH starts sharply when the line scan reaches the sample, a behavior rooted in the presence of the fluid flow model, which prevents ions from being diffused to the left, as shown in Fig. 5.5. Similarly, the advected ions in the direction of fluid flow (to the right in Fig. 5.5) prevent the pH value from decreasing dramatically where the sample ends in the line scan mapping. Moreover, the line scans show different behavior for experiments performed at room temperature compared to 37°C, especially for CP Mg samples. At RT, the horizontal pH profile tends to descend slightly over time, meaning that the profile measured after 3 hours of degradation is placed above the one measured after 12 hours. This behavior occurs oppositely for the measurement done at 37°C. The computational predictions of line scan profiles follow the same pattern, which could be due to how the coupled model computed the change of concentration of various chemical components and their contribution to the change of local pH.

Regarding the horizontal line scan results, a slight increase in the local pH values can be observed in the computational results in the region where the sample ends (Fig. 5.7). Although a similar behavior can be seen in the experimentally-obtained line scans (Fig. 5.6), it should be further investigated from the numerical implementation perspective to make sure that numerical artifacts do not contribute to it. One possible approach that may help remove numerical artifacts in this regard is to make the type of employed boundary conditions consistent in the employed fluid flow model. In the current model, a velocity condition was used for the inlet while the outlet condition was fixed pressure. Using the same type of boundary conditions for both inlet and outlet, meaning either assigning pressure conditions to the inlet or velocity to the outlet, can be considered in further extensions of the model to check their effect on the obtained local pH results.

As mentioned before, various chemical components of the electrolyte contribute differently to the change of pH, among which Ca^{2+} seems to have the most intricate effect [7]. It has been reported that in the absence of Ca^{2+} ions, the surface pH tends to be between 10 and 11, the typical range for pH value in biodegradation tests performed in saline solution [146]. This value is in line with the computational predictions of our previous study [131] (Chapter 3). However, in presence of Ca^{2+} cations, local pH between 7.8 and 8.5 and significantly lower degradation rates are reported [36, 153–155]. These findings are in line with the predictions made by the model presented in this chapter, obtained by coupling a mechanistic modeling approach and chemical equilibrium modeling, the latter of which considers the presence of Ca^{2+} .

The simplification assumptions made for developing the computational model, including the correlation between the diffusion rates of hydroxide and Mg ions, higher film elimination rate at room temperature, and the time at which the precipitation layer starts to form, can be seen as the limitations of the developed model. Regarding the latter mentioned assumption, the time was hard-coded into the model due to limitations of implementing the actual mechanisms of inducing the precipitation in the model. This can be improved in further developments of the model by incorporating a kinetics-based description of the precipitation layer formation, similar to the formation of magnesium hydroxide layer defined using a PDE (Eq. 5.20). This improvement will remove the necessity of the assumption made for linking the results obtained in equilibrium using the thermodynamics-based code (module 2) with the kinetics-based model (module 1), which was elaborated in section 5.2.2.

Knowing the mechanism of ionic activities at regions close to the biodegradation interface is crucial for comprehending the chemical process of Mg in complex solutions such as simulated physiological conditions. The developed

computational model can be seen as an facilitating tool for moving towards understanding these mechanisms by making it possible to virtually investigate the effective parameters such as the flow rate and environment composition. This knowledge will be helpful for biomedical applications where new coating and stabilization systems can be developed for different implantation environments.

5.5 Conclusion

In this chapter, the model developed in Chapter 3 was extended and combined with the fluid flow model developed in Chapter 4 to deliver a computational model of the biodegradation process in hydrodynamics conditions capable of predicting local pH changes close to the corrosion surface. In order to simulate local pH evolution in simulated body fluids, the precipitation of the hydroxyapatite-like protective model should be modeled. This was done by coupling the mentioned model with a thermodynamics-based code to compute the concentration of active chemical components contributing to the formation of the protective layer on the degradation interface. Results obtained from the coupled model show a good agreement with experimentally-obtained local pH measurements, demonstrating the effectiveness of the developed simulation workflow.

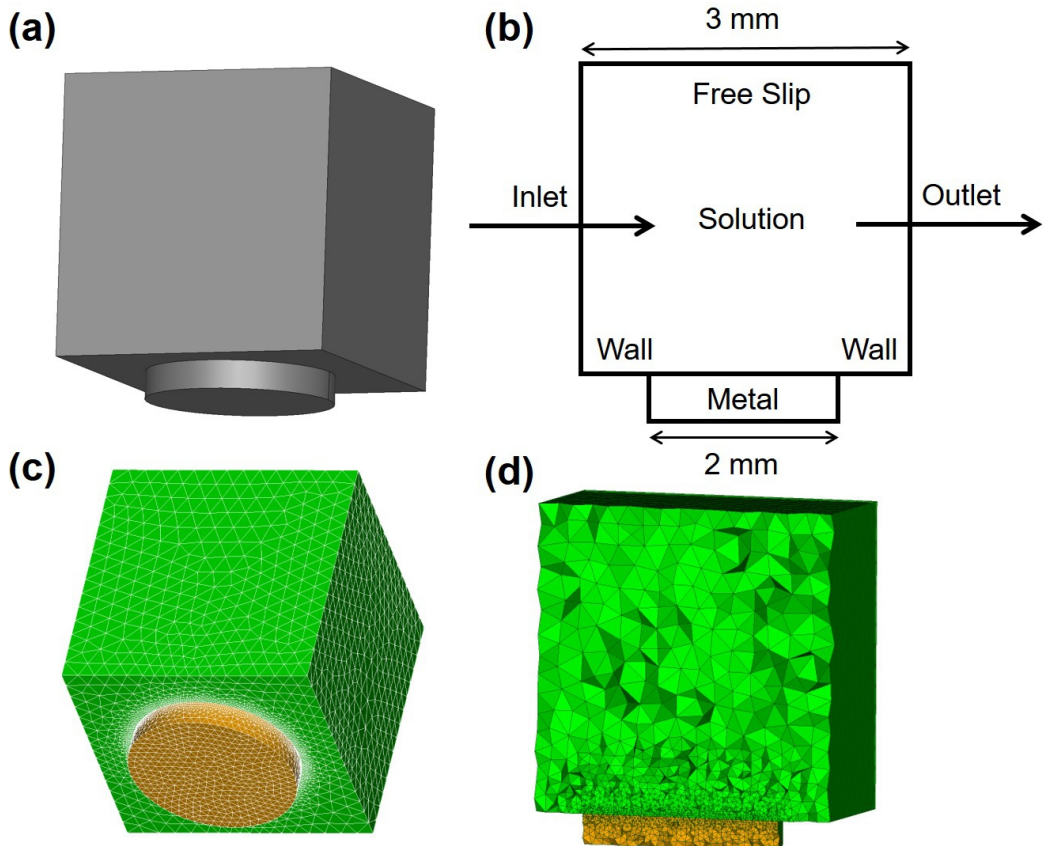


Figure 5.3: Computational model setup for local pH simulations: a) the geometry of the desired domain, being a small portion of the full chamber on top of the disc-like sample, b) the dimensions of the domain and applied boundary conditions for the fluid flow simulation, c) the generated computational mesh, depicting the flow region in green and the biodegradable sample in yellow, d) a cross-section of the mesh showing the refined meshing on the interface of the degradable metal.

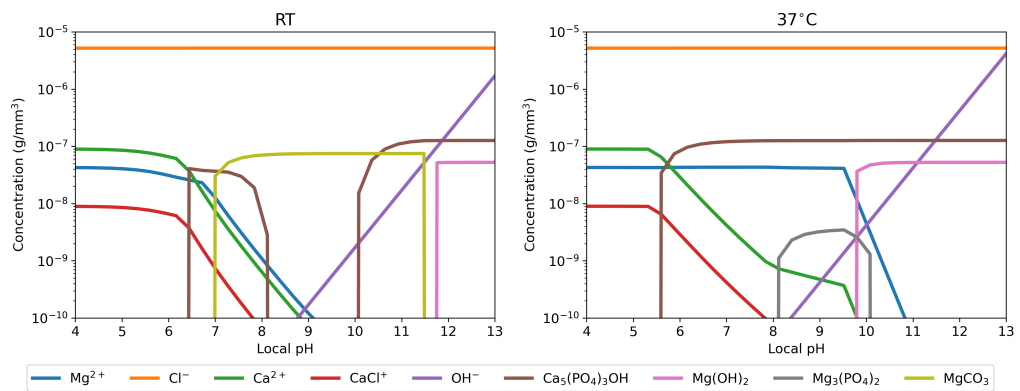


Figure 5.4: Selected relevant components from the Hydra-Medusa software output for given experimental conditions, showing how the concentration of various components vary with changing local pH

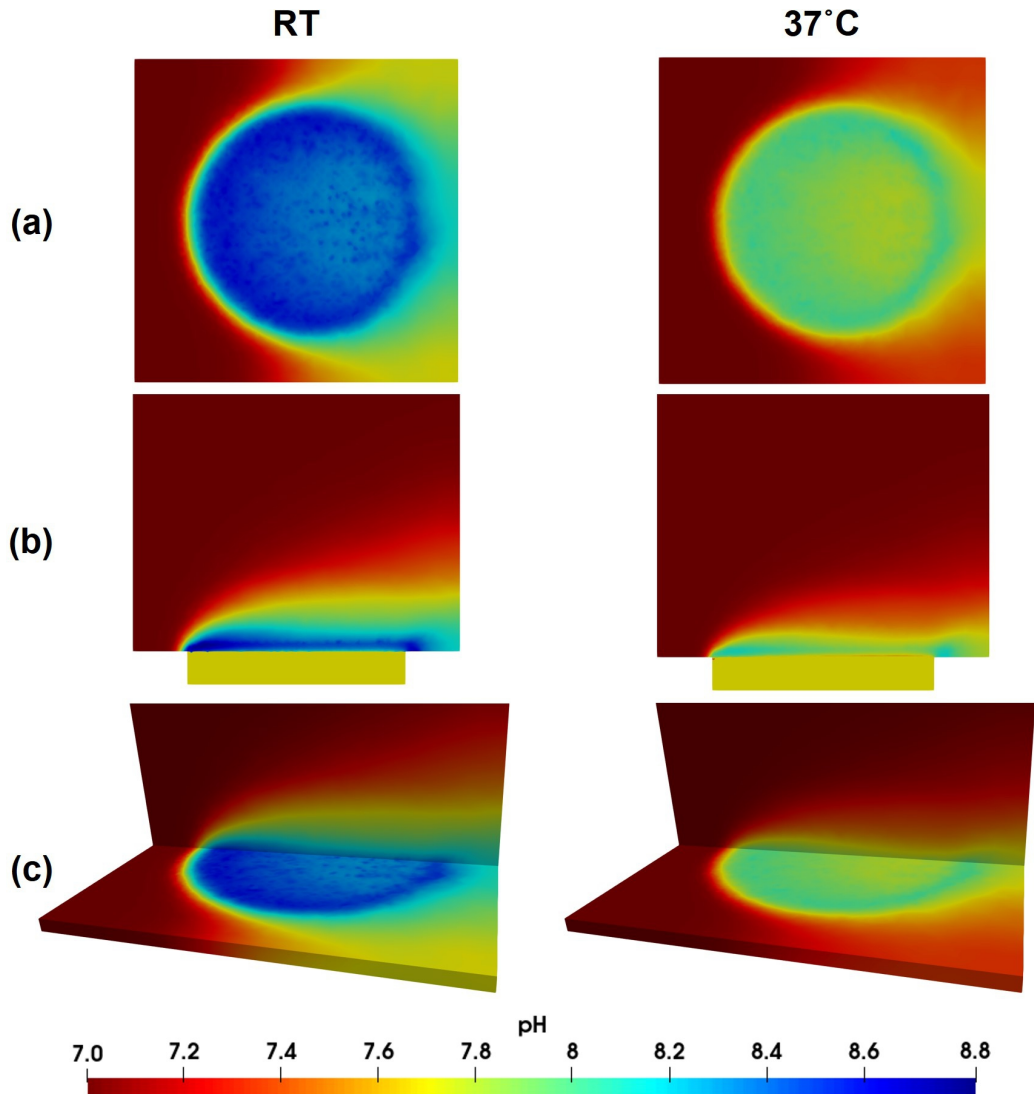


Figure 5.5: Simulation results for local pH predictions, depicting the local pH in a) top view from a horizontal cross-section, b) side view from a vertical cross-section, and c) perspective view with both the top and side cross sections, for simulations performed at 25°C (RT) and 37°C .

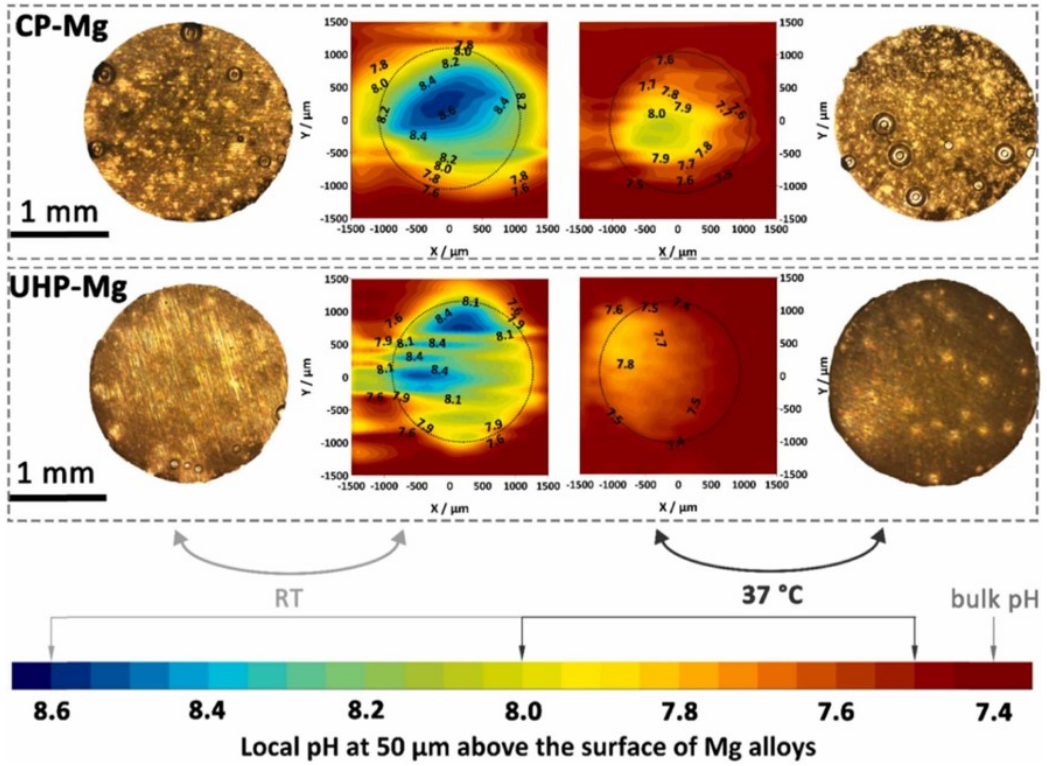


Figure 5.6: Experimental results for the distribution of local pH above the surface of the sample, measured after 12 hours of degradation.

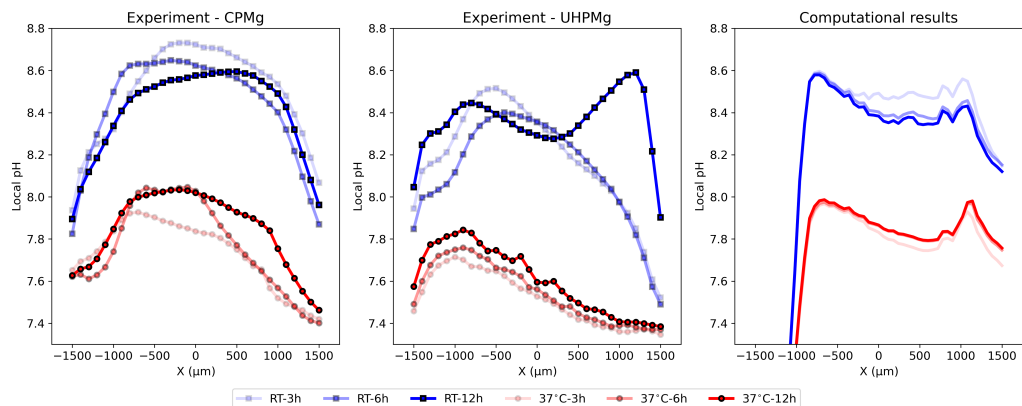


Figure 5.7: Comparing computational predictions and experimentally-obtained horizontal line scans of local pH changes, measured 50 μm above the surface of the sample after 3, 6, and 12 hours of degradation.

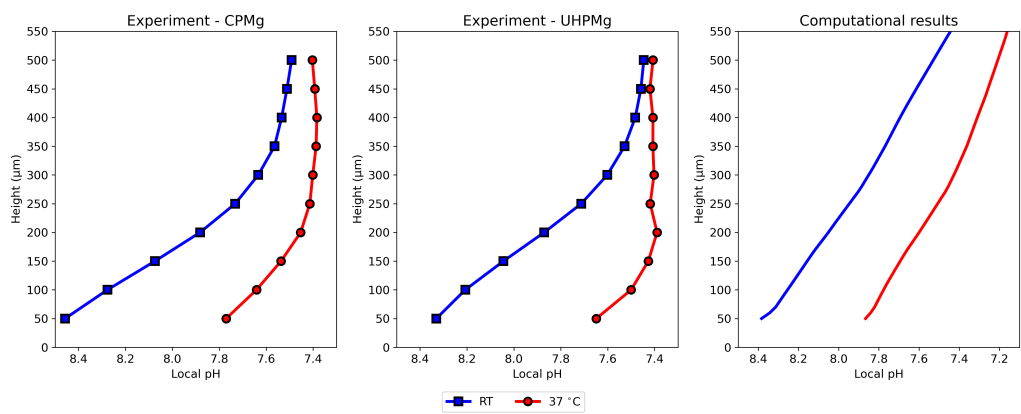


Figure 5.8: Comparing computational and experimental results for the local pH profiles, measured over a vertical line above the center of the sample after 12 hours of immersion.

Chapter 6

Computational modeling of the neotissue growth process

This chapter contains partial results from previously published content in *Advanced Functional Materials*:

D. Van, B. Liang, S. Anania, M. Barzegari, B. Verlée, G. Nolens, J. Pirson, L. Geris, F. Lambert, “3D-Printed Synthetic Hydroxyapatite Scaffold With In Silico Optimized Macrostructure Enhances Bone Formation In Vivo,” *Advanced Functional Materials*, vol. 32, p. 2105002, 2022.

This chapter focuses on developing computational models of the curvature-driven neotissue growth process, which can be coupled with the biodegradation model to have a hybrid model of biodegradation of biomaterials combined with the growth of neotissue inside/around them. To this end, two curvature-driven models were developed using the phase-field and level-set interface tracking techniques and compared to evaluate their similarities and differences.

6.1 Introduction

Neotissue is defined as the cells and the extracellular matrix they produce. Coupling biodegradation and neotissue growth models can be useful for tuning the biodegradation rate to the rate of regeneration of new tissue, an example of which can be found in Chapter ???. Similar to the biodegradation model, the modeling of the tissue formation process can take advantage of the interface tracking techniques in which the neotissue surface evolves over time, representing the growth process. Neotissue growth in porous scaf-

folds has been shown to be depending on the local mean curvature of the interface between the neotissue and the surrounding void space [156–158]. The commonly-used interface tracking techniques provide an efficient way to formulate curvature-driven problems. Although these models do not have immediate clinical applications, they can be quite useful for *in vitro* tissue engineering experiments where the proliferation behavior and growth of various cell types need to be improved.

Numerical tracking of interface movement has been widely used for certain modeling applications in science and engineering for multi-material and multiphase problems such as solidification, melting, corrosion, and grain growth to name a few [159]. The most popular Eulerian methodologies in this regard are the level-set [80, 160, 161], volume-of-fluid (VOF) [162], and phase-field methods [163, 164].

The basic idea of the level-set method is to employ the Hamilton-Jacobi (HJ) algorithm for solving the general interface advection equation. The independent variable in the level-set method is a signed distance function called the level-set function ψ [80]. The level-set function should be re-initialized as the interface evolves, which is the reason behind an inadvertent mass loss, one of the most prominent shortcomings of the level-set method. Although the VOF method is not vulnerable to the mass loss issue, calculating the interface curvature is difficult from the volume fraction [159], making it less efficient to be used for curvature-driven problems.

To overcome these challenges, diffuse interface methods [165] have gained attention in recent decades, among which the phase-field method has shown potential for solving complex moving interface problems. Contrary to the level-set method, the interface is considered a smooth transition between phases, which usually has a finite width in diffuse interface methods. In the phase-field method, a non-conserved (or conserved) order parameter ϕ is defined such that $\phi = 1$ in one bulk phase and $\phi = -1$ in the other. Then, the smooth transition between these two phases ($-1 < \phi < 1$) is marked as the interface. One of the advantages of the phase-field method is that the derived equation can be solved over the entire desired domain without considering the location of the interface. Moreover, although the curvature and interface normal vectors are not formulated explicitly, the phase-field method is suitable for problems in which the evolution of the interface depends on the local curvature or a field acting normal to the interface [159]. The phase-field method keeps a constant thickness for the smooth transition region normal to the interface, and as a result, no re-initialization as for the level-set method is needed.

The phase-field method has been already proved to be an efficient interface tracking technique for various problems in micro/meso scales such as

solidification [163, 166], microstructural evolution [167], grain growth [168], crack propagation [169, 170], electromigration [171] and extractive metallurgy [164]. However, it has been used recently for dealing with problems described in macro level, such as corrosion [172–178] and cell/tissue growth [179, 180]. This chapter discusses the development of a phase-field model of the tissue growth process to describe the cell growth behavior on 3D surfaces as a moving-boundary problem. Additionally, a similar model was developed based on the level-set method to compare the performance and results of both interface tracking methods. Both models were implemented using the finite element method.

6.2 Deriving the model

This section demonstrates the derivation of the phase-field and level-set equations from the general advection equation, showing the similarities and differences of these interface tracking techniques for moving boundary problems.

6.2.1 General equation of interface motion

The general interface advection equation for an Eulerian description of interface movement can be written as [159]:

$$\frac{\partial \phi}{\partial t} + \mathbf{u} \cdot \nabla \phi = 0, \quad (6.1)$$

where ϕ is the phase-field and \mathbf{u} is the interface velocity. The velocity \mathbf{u} can be divided into normal (u_n) and external velocity components (\mathbf{u}_e):

$$\mathbf{u} = u_n \mathbf{n} + \mathbf{u}_e, \quad (6.2)$$

in which $\mathbf{n} = \nabla \phi / |\nabla \phi|$ is the unit vector normal to the interface. So, Eq. 6.1 can be rewritten as:

$$\frac{\partial \phi}{\partial t} + u_n |\nabla \phi| + \mathbf{u}_e \cdot \nabla \phi = 0. \quad (6.3)$$

The normal velocity can be decomposed into more components to take into account the effect of interface curvature (κ) such that the terms are independent and proportional to the curvature, respectively:

$$u_n = a - b\kappa, \quad (6.4)$$

where the coefficients a and b have units of m/s and m²/s. Substituting this into Eq. 6.2 yields the final form of the interface motion equation:

$$\frac{\partial \phi}{\partial t} + a |\nabla \phi| + \mathbf{u}_e \cdot \nabla \phi = b\kappa |\nabla \phi|. \quad (6.5)$$

6.2.2 Phase-field formulation

To further proceed with the phase-field formulation, a proper kernel should be selected for the phase-field variable, which can be done based on Beckermann et al. [181]:

$$\phi = -\tanh\left(\frac{n}{\sqrt{2}w}\right), \quad (6.6)$$

in which w is the thickness of the transition profile (ϕ varies from -0.9 to $+0.9$ in a narrow layer with the width of $3\sqrt{2}w$), and n is the coordinate normal to the interface. The curvature can be written as a function of the phase-field variable:

$$\kappa = \nabla \cdot \mathbf{n} = \nabla \cdot \left(\frac{\nabla \phi}{|\nabla \phi|} \right) = \frac{1}{|\nabla \phi|} \left[\nabla^2 \phi - \frac{(\nabla \phi \cdot \nabla) |\nabla \phi|}{|\nabla \phi|} \right]. \quad (6.7)$$

Using the defined kernel, the terms in Eq. 6.7 can be expressed as:

$$|\nabla \phi| = -\frac{\partial \phi}{\partial n} = \frac{1 - \phi^2}{\sqrt{2}w} \quad \text{and} \quad \frac{(\nabla \phi \cdot \nabla) |\nabla \phi|}{|\nabla \phi|} = \frac{\partial^2 \phi}{\partial n^2} = -\frac{\phi(1 - \phi^2)}{w^2}. \quad (6.8)$$

Substituting Eq. 6.8 into Eq. 6.7 yields to the following definition of interface curvature:

$$\kappa = \frac{1}{|\nabla \phi|} \left[\nabla^2 \phi + \frac{\phi(1 - \phi^2)}{w^2} \right], \quad (6.9)$$

which subsequently changes Eq. 6.5 into:

$$\frac{\partial \phi}{\partial t} + a|\nabla \phi| + \mathbf{u}_e \cdot \nabla \phi = b \left[\nabla^2 \phi + \frac{\phi(1 - \phi^2)}{w^2} \right]. \quad (6.10)$$

Eq. 6.10 is the derived form of the phase-field equation for tracking an evolving interface, containing terms corresponding to normal interface motion, advection by an external field, and curvature-driven movement. The term $|\nabla \phi|$ in Eq. 6.10 can be replaced by its definition in Eq. 6.8 to form another version of the equation:

$$\frac{\partial \phi}{\partial t} + a \frac{1 - \phi^2}{\sqrt{2}w} + \mathbf{u}_e \cdot \nabla \phi = b \left[\nabla^2 \phi + \frac{\phi(1 - \phi^2)}{w^2} \right], \quad (6.11)$$

which is an easier version to be implemented using numerical methods. The unique term on the right-hand side of Eq. 6.11 is a characteristic of the phase-field method.

6.2.3 Level-set formulation

From the mathematical perspective, the level-set equation has a direct connection to the phase-field equation and can be derived by replacing the phase-field variable with a sign distance function. To this end, Eq. 6.5 can be rewritten to be a level-set equation:

$$\frac{\partial \psi}{\partial t} + a|\nabla \psi| + \mathbf{u}_e \cdot \nabla \psi = b\kappa|\nabla \psi|, \quad (6.12)$$

with ψ being a sign distance function that describes the distance of each point of the computational domain to the interface. This implies that the zero iso-contour of the level-set function defines the interface.

6.3 Dimensionless forms for various cases

6.3.1 Stationary interface

A stationary interface, where there is no interface motion ($a = 0$ and $\mathbf{u}_e = 0$), is a primary problem in examining the formulation and select proper grid spacing parameters. For a 1-D case, Eq. 6.11 can be simplified as:

$$\frac{\partial \phi}{\partial t} = b \left(\frac{\partial^2 \phi}{\partial x^2} + \frac{\phi(1 - \phi^2)}{w^2} \right). \quad (6.13)$$

To scale this equation, the following dimensionless variables can be defined:

$$x' = \frac{x}{x_c} \quad \text{and} \quad t' = \frac{t}{t_c}. \quad (6.14)$$

So, Eq. 6.13 can be rewritten using these new variables:

$$\frac{1}{t_c} \frac{\partial \phi}{\partial t'} = \frac{b}{x_c^2} \frac{\partial^2 \phi}{\partial x'^2} + \frac{b}{w^2} f(\phi), \quad (6.15)$$

with $f(\phi)$ being defined as:

$$f(\phi) = \phi(1 - \phi^2). \quad (6.16)$$

Defining $x_c = w$ and $t_c = w^2/b$ leads to the following dimensionless form of Eq. 6.13:

$$\frac{\partial \phi}{\partial t'} = \frac{\partial^2 \phi}{\partial x'^2} + \phi(1 - \phi^2). \quad (6.17)$$

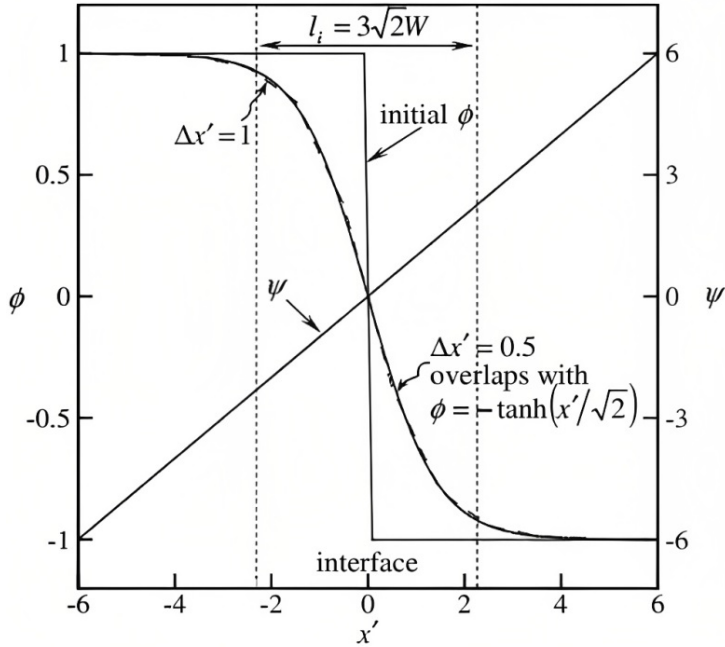


Figure 6.1: Comparison of phase-field variable and level-set function on the interface of a stationary interface with step function like initial condition [159]

Numerical results for Eq. 6.17 is depicted in Fig. 6.1, and the phase-field profile is compared with the level-set distance function profile. An appropriate value for grid spacing and the layer width should be selected such that $0.25w < \Delta x' < 0.5w$. Additionally, the selected value of w should satisfy $w < R/4.2$, in which R is the local radius of curvature [159].

6.3.2 Evolution under constant normal speed

For a problem in which the interface moves with constant velocity exclusively, Eq. 6.11 in 1-D can be simplified according to the condition of $a = \text{const.}$, $\mathbf{u}_e = 0$, and $b = 0$:

$$\frac{\partial \phi}{\partial t} + a \frac{1 - \phi^2}{\sqrt{2}w} = \beta \frac{\partial^2 \phi}{\partial x^2} + \beta \frac{f(\phi)}{w^2}, \quad (6.18)$$

in which β is a numerical parameter for smoothing the interface and relaxation behavior of the phase-field profile.

Defining dimensionless variables according to Eq. 6.14 yields to:

$$\frac{1}{t_c} \frac{\partial \phi}{\partial t'} + \frac{a}{w} \frac{1 - \phi^2}{\sqrt{2}} = \frac{\beta}{w^2} \frac{\partial^2 \phi}{\partial x'^2} + \frac{\beta}{w^2} f(\phi), \quad (6.19)$$

which can be reordered to:

$$\frac{\partial\phi}{\partial t'} + \frac{1-\phi^2}{\sqrt{2}} = \beta' \left(\frac{\partial^2\phi}{\partial x'^2} + f(\phi) \right), \quad (6.20)$$

with $\beta' = \beta/aw$. For a stable numerical implementation, $\Delta t'/\Delta x' < 0.1$ and $\beta' < 1.2$ should be met roughly [159].

6.3.3 Curvature-driven interface evolution

A curvature-driven motion, which is desired for the current study, is straightforward to formulate using the phase-field method. A dimensionless form of Eq. 6.11 can be derived using a similar method for the stationary interface for a multidimensional case with $u_n = -b\kappa$, $a = 0$, and $\mathbf{u}_e = 0$:

$$\frac{\partial\phi}{\partial t'} = \nabla'^2\phi + \phi(1-\phi^2), \quad (6.21)$$

in which t' and ∇' are defined similar to Eq. 6.14 as $t' = t/(w^2/b)$ and $\nabla' = \nabla/w$, respectively.

6.4 Adapting the formulation for curvature-driven tissue growth

Due to intrinsic support of interface curvature in the phase-field and level-set methods, an *in silico* model of curvature-based tissue growth can be efficiently implemented using these principles. The growth-induced changes in the neotissue topology during the culture process can be seen as a moving interface between two different domains [158]. In this study, one domain represents the neotissue volume (Ω_{nt}), and the other one is the void (Ω_v), which are separated by an interface (Γ) as can be seen in Fig. 6.2.

The interface Γ evolves over time to fill the void space, having a faster growth in regions with higher curvature. Based on this definition, the phase-field variable can be defined as follows to separate these domains:

$$\begin{cases} \phi = 1 & \text{in } \Omega_{nt} \\ \phi = -1 & \text{in } \Omega_v \\ -1 < \phi < 1 & \text{in } \Gamma \end{cases} \quad (6.22)$$

Similarly, a level-set function can be defined such that it separates the neotissue and void domains:

$$\begin{cases} \psi > 0 & \text{in } \Omega_{nt} \\ \psi < 0 & \text{in } \Omega_v \\ \psi = 0 & \text{in } \Gamma \end{cases} \quad (6.23)$$

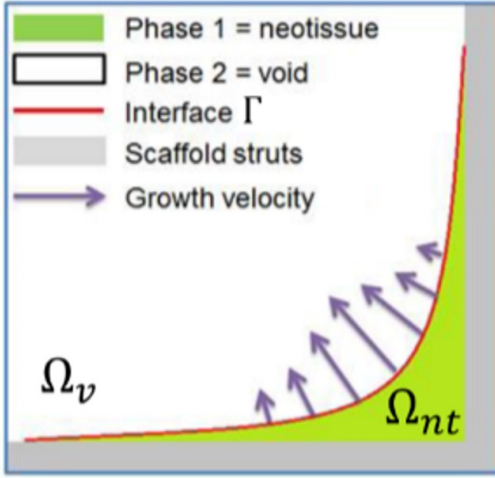


Figure 6.2: Schematic representation of the phase-field and level-set models for tissue growth, in which the neotissue domain (Ω_{nt}) is separated from the void domain (Ω_v) by an interface (Γ).

In order to adapt Eq. 6.21 for the curvature-driven process of neotissue growth, one can consider the following equation:

$$\frac{\partial \phi}{\partial t'} = (\nabla'^2 \phi + \phi(1 - \phi^2)) . H(\nabla'^2 \phi + \phi(1 - \phi^2) > 0), \quad (6.24)$$

in which H denotes a Heaviside step function. Eq. 6.24 implies that the growth is only allowed for regions with a positive curvature (right hand side of Eqs. 6.11 and 6.21).

Using the same approach, a similar level-set formulation can be obtained based on Eq. 6.12 by omitting the normal velocity and curvature terms and embedding the effect of the curvature in the velocity field. Doing this yields a convection equation for the distance function:

$$\frac{\partial \psi}{\partial t} + \mathbf{u} \cdot \nabla \psi = 0, \quad (6.25)$$

in which the convection velocity field can be defined as:

$$\mathbf{u} = \begin{cases} -\kappa \mathbf{n} & \text{if } \kappa > 0 \\ 0 & \text{if } \kappa \leq 0 \end{cases} \quad (6.26)$$

with κ being calculated similarly to Eq. 6.7 for a distance function ψ . This implies that neotissue grows faster where the curvature is higher and does not grow if the curvature is negative or equal to zero [156]. The negative

sign in Eq. 6.26 is due to our definition of ψ , where the normal n_Γ points toward neotissue, so growth has to be towards the opposite of the gradient of the level-set function ($\nabla\psi$).

6.5 Numerical implementation

6.5.1 Phase-field model

The numerical solution of the phase-field equation requires dealing with the nonlinearity of the equation. Additionally, in the case of the dimensional form (Eq. 6.11), small coefficients of the state variable in the PDE lead to numerical difficulties. As a result, numerical implementation of the phase-field equation, especially for the spectral methods and the finite element method, is not straightforward and is an active field of research [182, 183].

In the finite element method, the solution of a PDE is calculated based on a sum of a set of certain basis functions, which are commonly piecewise linear, quadratic or polynomial functions that are non-zero only on a small element. For doing this, the PDE is first written in a weak formulation, and then the weak form is projected on a discretized space (a set of elements) to be written as the summation of the basis functions.

In this section, the numerical solution of the stationary form (Eq. 6.13) and its corresponding considerations are elaborated as an example of employing the finite element formulation for simulating the phase-field equation. So, by assuming $b = 1$, the problem can be summarized as:

$$\begin{cases} \frac{\partial\phi}{\partial t} - \Delta\phi + \frac{1}{w^2}f(\phi) = 0, & (x, t) \in \Omega \times (0, T] \\ \frac{\partial\phi}{\partial n} \Big|_{\partial\Omega} = 0 \\ \phi|_{t=0} = \phi_0 \end{cases} \quad (6.27)$$

which demonstrates the PDE, the boundary condition, and the initial condition of the phase-field variable where Ω is the domain of interest, $\partial\Omega$ is its boundary, and T is the final time. Deriving the weak formulation of Eq. 6.27 is relatively straightforward as it can be seen as a time-dependent diffusion-reaction PDE, but the difficulty arises in choosing the numerical stability scheme for discretizing the temporal derivative and dealing with the nonlinearity of $f(\phi)$ when normally the $\frac{1}{w^2}$ coefficient is a small number.

Incorporating a first-order semi-explicit scheme for Eq. 6.27 yields [183]:

$$\frac{1}{\Delta t} (\phi^{n+1} - \phi^n, v) + (\nabla\phi^{n+1}, \nabla v) + \frac{1}{w^2} (f(\phi^n), v) = 0, \quad \forall v \in H^1(\Omega), \quad (6.28)$$

where Δt is the time step, (\cdot, \cdot) denotes the inner product, and $H^1(\Omega)$ is the Sobolev space of the domain Ω , which is a space of functions whose derivatives are square-integrable functions in Ω . The main issue with this discretization scheme is its restrictive time step condition which should satisfy [182]:

$$\Delta t < \frac{2w^2}{L}, \quad (6.29)$$

where L is a limit related to the non-linear part:

$$\max |f'(\phi)| \leq L. \quad (6.30)$$

Obviously, since $\Delta t \sim w^2$, a very small time step is required to achieve stability in this scheme.

Taking advantage of a fully implicit scheme improves the stability because it will be unconditionally stable, but it results in an equation that is difficult to implement as it needs to solve a fixed point problem at each time step. For example, a modified second-order implicit Crank-Nicolson scheme for Eq. 6.27 can be written as [183, 184]:

$$\left(\frac{\phi^{n+1} - \phi^n}{\Delta t}, v \right) + \left(\nabla \frac{\phi^{n+1} + \phi^n}{2}, \nabla v \right) + \frac{1}{w^2} \left(\tilde{f}(\phi^{n+1}, \phi^n), v \right) = 0, \quad \forall v \in H^1, \quad (6.31)$$

where:

$$\tilde{f}(u, v) = \begin{cases} \frac{F(u) - F(v)}{u - v} & \text{if } u \neq v \\ f(u) & \text{if } u = v \end{cases} \quad (6.32)$$

in which F is the potential term ($f(\phi) = F'(\phi)$).

An alternative can be deriving a stabilized semi-implicit scheme by adding a stabilization term to Eq. 6.28. The first-order version of such a scheme can be written as:

$$\left(\frac{1}{\Delta t} + \frac{S}{w^2} \right) (\phi^{n+1} - \phi^n, v) + (\nabla \phi^{n+1}, \nabla v) + \frac{1}{w^2} (f(\phi^n), v) = 0, \quad \forall v \in H^1(\Omega), \quad (6.33)$$

which is unconditionally stable for any $S \geq \frac{L}{2}$ [182].

6.5.2 Level-set model

The derived level-set PDE (Eq. 6.25) is an advection equation, which can be implemented numerically using the finite element method, in which the temporal term is discretized by the backward Euler method, and the advection term can be treated with the method of characteristics.

A key parameter of the developed model is the local growth velocity of the neotissue. In the current implementation, the velocity was dependent on the interface's local mean curvature as shown in [157, 185]. In order to match the growth velocity to experimental data, a coefficient can be added to the derived interface convection velocity (Eq. 6.26):

$$\mathbf{u} = \begin{cases} -\kappa A \mathbf{n} & \text{if } \kappa > 0 \\ 0 & \text{if } \kappa \leq 0 \end{cases} \quad (6.34)$$

The model calibration performed by Guyot et al. [185] was for a culture condition on titanium scaffolds in a bioreactor setting, estimating parameter A to be $4 \times 10^{-14} \text{m}^2/\text{s}$, obtained using trial and error from the experimental data on low flow rate tests [186]. More dedicated calibration experiments were performed on prismatic structures, demonstrating a considerably slower growth on the CaP scaffolds, nevertheless confirming the curvature-based nature of tissue growth [187].

In practical implementations, the distance function is not differentiable at every location of the domain due to discontinuities in the gradients, so one can consider taking advantage of artificial diffusion terms to overcome this issue, leading to the following equations for the normal vector and curvature calculation:

$$\mathbf{n} = \frac{\nabla \varphi}{|\nabla \varphi|} + \varepsilon \Delta \mathbf{n} \quad (6.35)$$

$$\kappa = \nabla \cdot \mathbf{n} + \varepsilon \Delta \kappa, \quad (6.36)$$

in which ε denotes the numerical diffusion coefficient.

6.6 Simulation setup

Numerical simulations of neotissue formation on various shapes (scaffolds) were carried out using the developed phase-field and level-set models to compare their performance. In 2D, two shapes were used, a square and a semi-circle (Fig. 6.3), which were simulated using both phase-field and level-set models. The qualitative comparison of the two developed models were done using this 2D setup, so for 3D cases, the models were simulated on vastly different geometries for just checking the performance of the interface tracking techniques on 3D scaffolds. In 3D, both models were evaluated on a cube, but the level-set model was also used to simulate the cell growth behavior on scaffolds with triply periodic minimal surface (TPMS) shapes.

The initial configuration of the phase-field variable and level-set distance function corresponds to a homogenous single cell layer over the scaffold struts

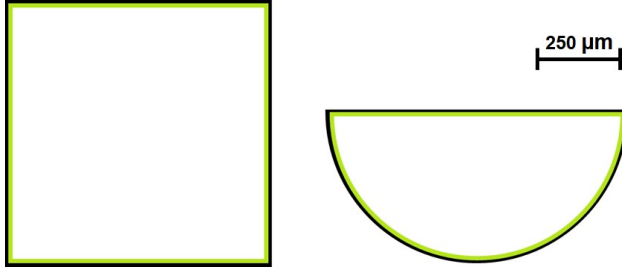


Figure 6.3: Schematic representation of the simulation domains

with a thickness equal to $10\mu m$ in a dimensional setup [188]. This is depicted as the green layer in Fig. 6.3. For the 3D level-set model, neotissue growth was simulated for a variety of TPMS family and compared in a qualitative manner. A full quantitative prediction is not possible due to the absence of relevant validation experiments, which explains why comparisons between geometries are made over non-dimensional time.

The derived weak forms were implemented using FreeFEM open-source PDE solver [86]. An Eulerian computational mesh for each simulation was constructed by generating tetrahedral elements using the internal mesh generator of FreeFEM, called BAMG. To decrease run time and increase the performance of the simulation, the mesh was partitioned using METIS graph partitioner [127] and HPDDM preconditioner [90], available in FreeFEM and the PETSc toolkit [89]. Moreover, the efficiency was boosted by using the HYPRE BoomerAMG preconditioner [87] and the GMRES iterative solver [88] of the PETSc toolkit.

6.7 Results and discussion

In the current study, various 2D and 3D cases for the simulation of curvature-based neotissue formation were prepared and separately simulated using the phase-field and level-set models. The cases were a square and a semi-circle for 2D simulations, mimicking the situation in which cells were homogeneously seeded onto the scaffold to initiate the production of extracellular matrix. Similarly, a 3D cube was considered for evaluating the performance of the implementation of both models in 3D. Additionally, the level-set model was used to simulate cell proliferation on TMPS scaffolds with quantitative measurements being carried out for the percentage and filling rate of generation of neotissue.

The results of neotissue growth model simulations can be visualized by

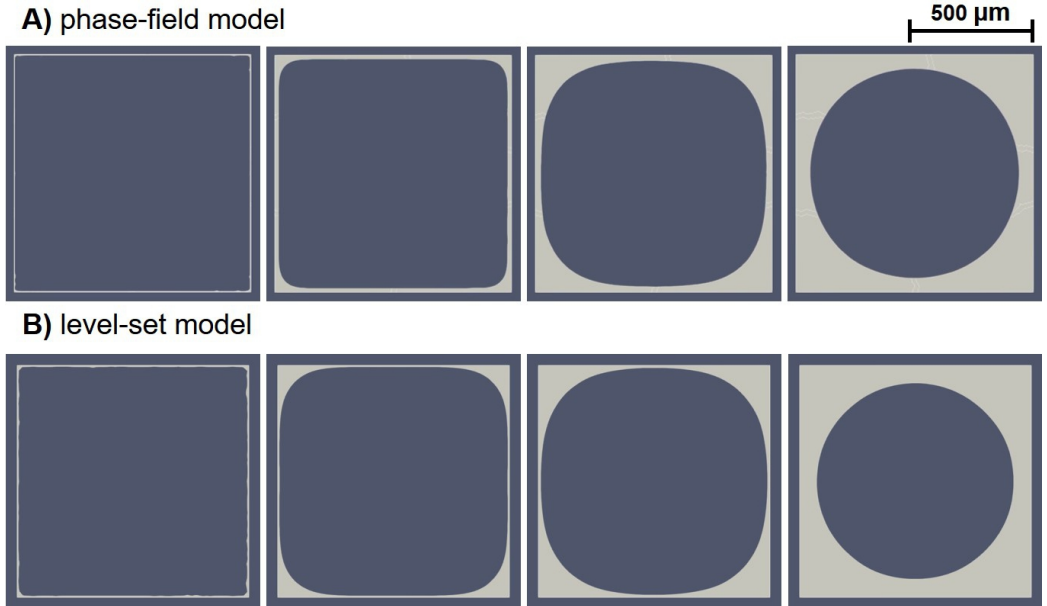


Figure 6.4: Simulation result of the phase-field (A) and level-set (B) models for neotissue growth in the square domain. The light gray region shows the +1 part of the phase-field variable and the positive part of the distance function for the phase-field (A) and level-set (B) models, respectively. The evolution occurs from left to right over non-dimensionalized time.

depicting the +1 part of the phase-field variable (Eq. 6.22) and the positive part of the level-set function (Eq. 6.23). Fig. 6.4 demonstrates such a visualization for the phase-field and level-set simulations performed on the square domain. Cells were seeded on the perimeter of the square, and the formation of neotissue was modeled using the evolution of the phase-field variable and level-set function. The light gray region in these figures shows the +1 part of the phase-field variable and the positive part of the level-set function.

As shown in Fig. 6.4, a qualitative comparison of the evolution of the formed tissue interface between the phase-field and level-set models indicates that they capture the curvature-driven growth similarly. It seems that the level-set model resulted in sharper interfaces, in which the surfaces without curvature do not move at all. But, in the phase-field predictions, the surfaces not having any curvature slightly move. This can be seen by comparing the growth pattern on the middle part of the top edge of the square, where it starts to grow only in the fourth column in Fig. 6.4 for the level-set results, while a minor move can be seen in the phase-field predictions. This

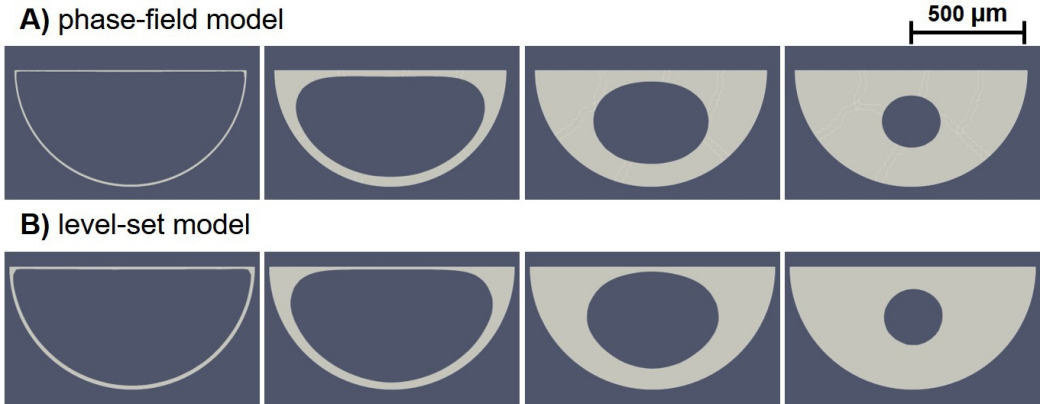


Figure 6.5: Simulation result of the phase-field (A) and the level-set (B) models for neotissue growth in the semi-circle domain. The evolution occurs from left to right over non-dimensionalized time.

slightly different behavior can be related to the implementation details, such as the lack of a proper Heaviside function in FreeFEM that the phase-field model depends on. Another possible reason for this difference can be the visualization aspect since the transition region of the phase-field variable representing the surface is thicker in the phase-field model in comparison to the zero iso-contour of the level-set function. As a result, the evolution can be artificially plotted in the visualization software, which was ParaView in this case. This effect can be investigated further by refining the mesh to minimize artificial evolution.

A similar visualization is depicted in Fig. 6.5 for the neotissue formation on the semi-circle domain. Results show that the phase-field and level-set models have good agreement on the way they treat the curvature-based tissue growth. As seen in the figure, both models show identical predictions on the surface with curvature (the curvy edge of the semi-circle). However, the small difference observed for the square case can also be seen here on the top surface, where the neotissue grows slightly faster in the phase-field model.

Fig. 6.6 shows the evolution of the phase-field variable corresponding to the results depicted in Fig. 6.5-A, demonstrating how the diffuse interface model works. In this figure, the concept of the diffusive interface can be observed, where a narrow region between the two phases (the neotissue and the void space in this case) is formed and moves over time. This visualization demonstrates the internal mechanism of the phase-field model, in which the narrow region is kept at a fixed length (defined by the kernel in Eq. 6.6 for a length of $3\sqrt{2}w$) and gets advected over time by the phase-field equation (Eq.

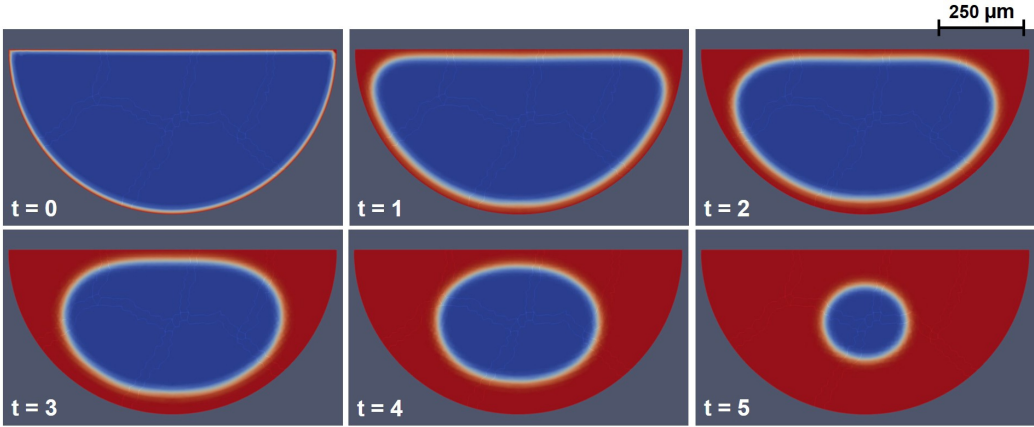


Figure 6.6: Visualization of the evolution of phase-field variable in the semi-circle domain. The evolution is depicted over time in an arbitrary unit, occurring from top to bottom and from left to right in each row. The red, blue, and white show the +1 region, -1 region, and the transient phase representing the interface, respectively.

6.11). In contrast, in the level-set formalism, the interface is not tracked as a fixed length region, and instead, the zero iso-contour of a signed distance function is the interface between the phases. The signed distance function maps each node of the whole space (the desired computational domain) into the distance to the interface, and as a result, the change in the function determines the movement of the interface.

Similar results are obtained in 3D, where the cells are seeded on the circumstance of a cuboid. Fig. 6.7 shows the simulation results of this 3D case, in which the evolution of the phase-field variable is converted to a bulk of the formed neotissue. As can be seen in this figure, the phase-field model performs well in 3D, showing a similar growth behavior to the 2D model. The mesh in the 3D case is relatively coarse, but the captured behavior of tissue growth by the phase-field model seems to be more acceptable than in the 2D case. This claim can be observed on the top and bottom surfaces of the cube, where the interface does not move until a curvature is created in those regions, a behavior that was captured better by the level-set model in the 2D cases.

Similarly, Fig. 6.8 shows the evolution of neotissue formation in a 3D level-set simulation, in which the results are similar to the ones obtained using the phase-field model (Fig. 6.7). Generally speaking, the level-set model requires finer mesh in 3D in order to capture the interface movement accurately, which is the reason behind having a smoother interface in Fig.

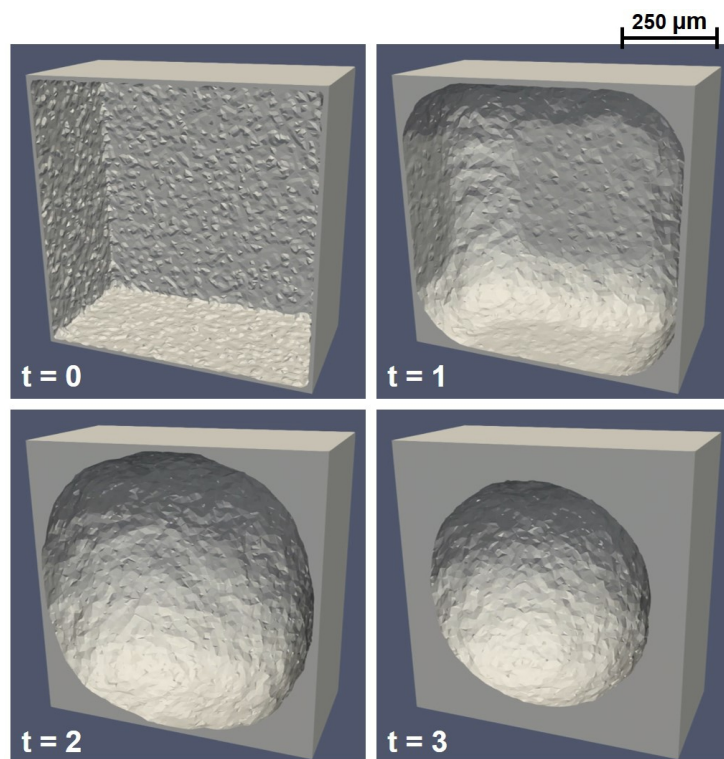


Figure 6.7: Simulation result of the phase-field model for neotissue growth in a 3D cube domain, in which the +1 regions of the phase-field variable are visualized to show the formation of neotissue over non-dimensionalized time.

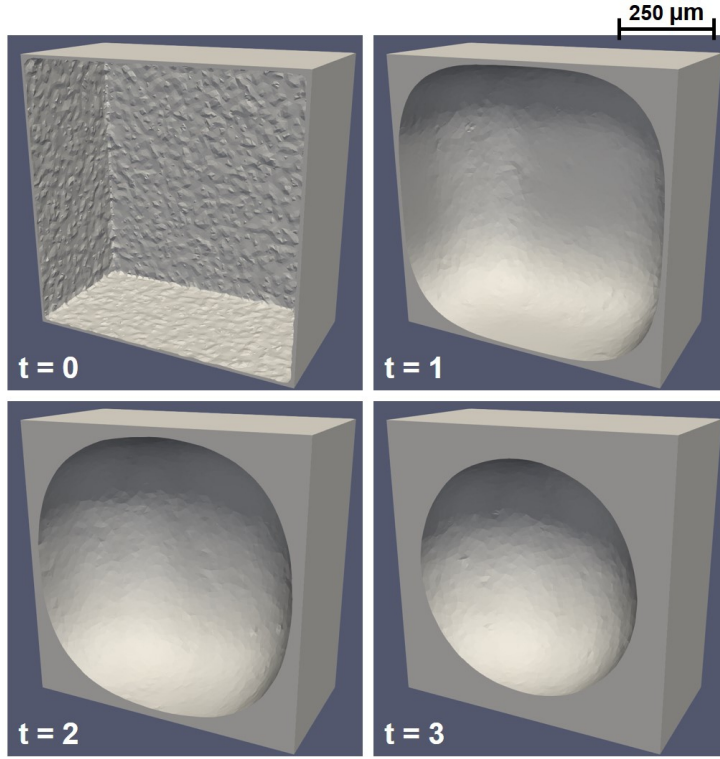


Figure 6.8: Simulation result of the level-set model for neotissue growth in a 3D cube domain, in which the positive regions of the level-set variable are visualized to show the formation of neotissue over non-dimensionalized time.

6.8 in comparison to Fig. 6.7. However, a qualitative comparison shows that both models act equivalently for capturing the curvature-dependent growth in 3D.

Fig. 6.9 depicts various simulation results of the netissue formation in gyroid-TPMS scaffolds, demonstrating an example of the final application of these models in action. The reason for choosing gyroid-TPMS scaffolds is their promising performance for neotissue formation due to their favourable local curvature. Various geometries for investigating the pore size and wall thickness were evaluated in order to obtain the combination leading to optimal neotissue growth. Pore size was varied between $700\mu m$ and $1.3mm$, and wall thickness was varied from $200\mu m$ to $800\mu m$, which are ranges that take into account restrictions of the manufacturing process in terms of the smallest feature dimensions. Balancing the need for swift neotissue ingrowth (Fig. 6.9-B, relevant for short-term implant stability) with the volume of neotissue formed (Fig. 6.9-A, relevant for long-term dental implant stabil-

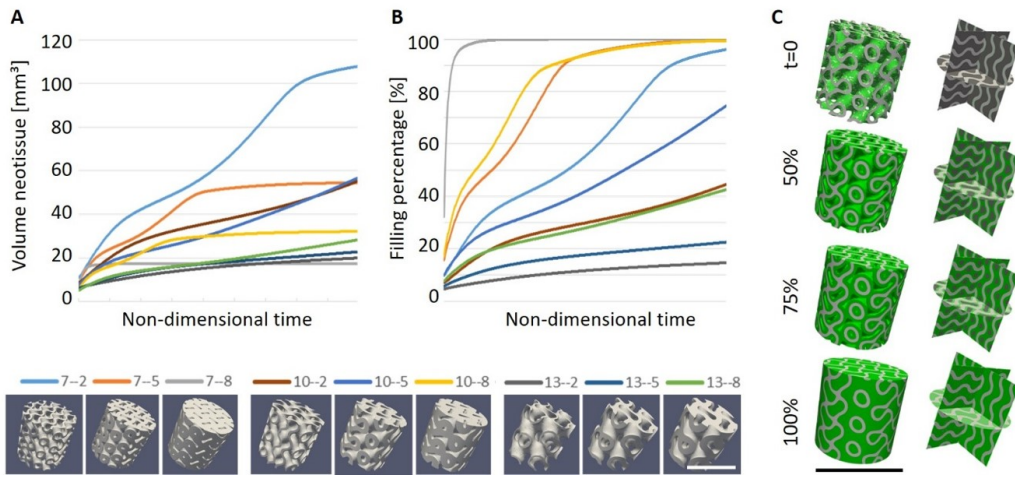


Figure 6.9: Neotissue formation quantified in absolute volume (A) and filling percentage (B) for cylindrical test samples (diameter 6 mm, height 6 mm). The different combinations are indicated in the legend by 2 numbers, the first of which refers to pore size (7: 700 μm , 10: 1 mm, 13: 1.3 mm), and the second refers to wall thickness (2: 200 μm ; 5: 500 μm ; 8: 800 μm). (C) Side view and cross-sectional view of neotissue growth in gyroid (7-2) scaffold for different levels of filling, starting with the initial condition at $t=0$ (top). Scale bars: 6 mm.

ity), the combination of 700 μm pore size and 200 μm wall thickness (Fig. 6.9-C) seemed to be the most optimal structure.

The study shown as an example above [187] demonstrates the relevance of the developed tissue growth models in tissue engineering applications. *In silico* modeling is widely used for tissue engineering as it offers a more exhaustive approach compared to a “trial-and-error” method and reduces the number of experimental tests. Optimization of scaffold structures for bone tissue engineering purposes is often corroborated by comparison with *in vitro* tests [189,190] and only a small number of *in vivo* studies have been reported in this regard [191–193]. However, in these *in vivo* studies, optimization was first performed on mechanical properties rather than the structural elements such as local curvature underlying the *in silico* model presented in this chapter. Having such a model developed makes it easier to investigate the structural elements of scaffolds for improved regenerative performance. Using the modeling results makes it possible to limit the number of conditions tested *in vivo*.

6.8 Challenges in coupling tissue growth and biodegradation models

Coupling our biodegradation model [131] (Chapter 3) with the developed tissue growth model in this chapter could have been a milestone of the current PhD thesis, where the neotissue is produced by the cells seeded on a biodegradable scaffold. Another interesting example could be using biodegradable porous implants in bone healing applications (similar to the model presented in Chapter ??), in which the implant degrades while new bone forms and replaces the porous implant. However, despite the effort put on tissue growth modeling, such coupling can be complicated to accomplish in a mechanistic manner due to specific technical difficulties. In this section, these challenges are briefly reviewed.

Both the biodegradation and the tissue growth models are free boundary problems, in which an interface capturing method (phase-field or level-set for the tissue growth and level-set for the biodegradation) was used to track the movement of a boundary. The moving boundary in the biodegradation model is the corrosion front, the interface between the metallic part and the surrounding environment, which can be a static electrolyte in immersion tests or circulated solutions in a perfusion setup. Various mass transfer boundary conditions are defined on this boundary [131], meaning that the boundary conditions are not fixed and move with the evolution of the surface. In other words, the boundary conditions of a set of equations are defined on the solution of one of the governing equations of the model (level-set equation), which is one of the challenging parts of the implementation of that model. On the other hand, the moving boundary in the tissue growth model is the surface of the formed neotissue, the interface between the neotissue and the surrounding environment in the bioreactor, which is considered as the void space since there is no tissue in that region. Coupling these two models requires defining the moving boundary problem of neotissue growth on the solution of the interface capturing of the biodegradation model. Regardless of using the same technique for both problems or using separate methods for each problem, such coupling can be quite challenging from the implementation perspective.

The second problem is related to the behavior of neotissue formation after coupling the models when the biodegradable material shrinks and a new void space appears at the back of the formed neotissue. Fig. 6.10 shows this problem schematically. Fig. 6.10-A shows an initial state of the coupled system, in which a level-set formulation is used to divide the domain into the scaffold and medium parts (the ψ function on the top) while a phase-field

function divides the domain into tissue and void space (the ϕ function on the bottom). The positive side of the level-set function ($\psi > 0$) is not defined in the domain of the tissue growth model ($\phi = \text{NaN}$). After several time steps, the system enters a state similar to the one depicted in Fig. 6.10-B, where the scaffold has shrunk to the left due to biodegradation, and the tissue has grown to the right. As can be seen in the figure, these movements cause a new area to appear between the scaffold and neotissue, in which the level-set function is negative ($\psi < 0$) and the phase-field variable is one ($\phi = +1$). Since this area is part of the void space for the phase-field model, the tissue should grow in this direction as well, but this behavior does not have a clear definition from an implementation point of view. From a common-sense perspective, one might expect part of the tissue to still be attached to the surface of the scaffold and move with it to the left, a behavior that is quite challenging to consider in the formulation of the two coupled interface moving problems. Moreover, it is not fully clear how such behavior happens in experiments, so dedicated experiments are required to observe the actual reaction of the growing neotissue to the shrinkage of the scaffold. This behavior may be sensitive to experimental conditions such as static or perfusion setup of the medium, making the problem even more complex from the mathematical perspective.

A potential solution for the mentioned coupling challenge would be to take advantage of the multi-phase field method for describing both the biodegradation and tissue growth processes using a single model. Putting this solution into practice requires a tremendous amount of work to re-implement the biodegradation model using the phase-field method, which needs to change part of the fundamental equations in the mathematical model elaborated in Chapter 3, but it removes the necessity of coupling two models and dealing with the emerging difficulties in the implementation. Such an idea has already been implemented in studies like Moure et al. work [194, 195], in which they used a multi-phase field model to investigate individual and collective cell migration and crawling.

The next challenge would be the validation of the coupled model. In addition to the necessity mentioned above for performing dedicated experiments to observe the actual behavior of tissue growth on biodegradable scaffolds, such experiments are crucial to validate the model from a quantitative point of view. Doing these experimental studies seems to be challenging and resource-demanding because both the qualitative behavior and quantitative measurements should be recorded. The qualitative behavior is crucial to observe how tissue growth reacts to the shrinkage of the material underneath, while the quantitative output of the experiments can be directly used to validate the rate of degradation and neotissue formation predicted by the

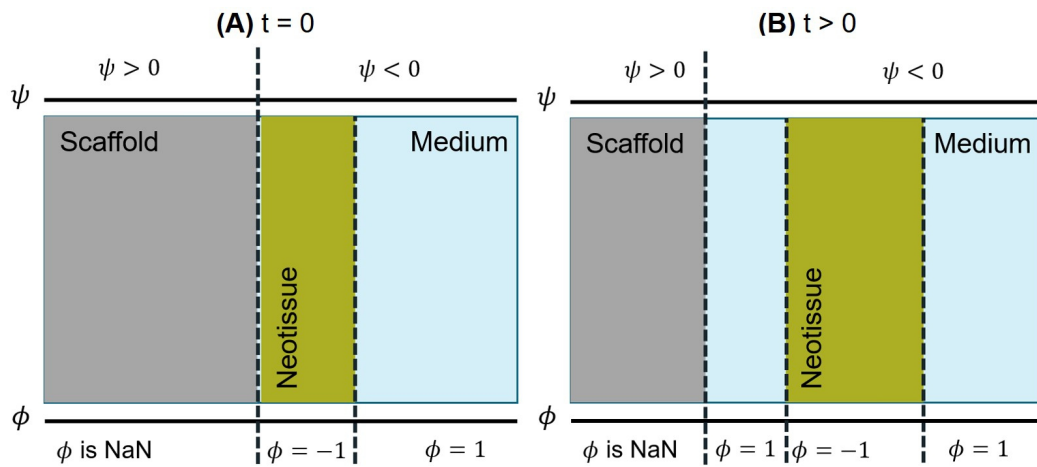


Figure 6.10: Schematic presentation of coupled neotissue growth and biodegradation models (implemented using phase-field and level-set methods respectively): A) initial state of the system with level-set (ψ) and phase-field (ϕ) variables dividing the domain for the biodegradation and neotissue growth models, respectively, B) the state of the system after some time steps, in which the biodegradation shrinks the scaffold to the left, the neotissue grows to the right, and a new area emerges between the scaffold and the neotissue.

coupled model. Such resource-demanding experiments were never planned as part of this PhD, and as a result, the coupled models could not be easily validated.

A suitable workaround for the aforementioned challenges can be coupling the biodegradation model with a simpler tissue growth model in the first place. A simpler model here implies that it does not include an interface tracking sub-model, for which the above challenges may appear in the implementation. An example of such simplified coupling is the work of Byrne et al. [196], in which random walk algorithms were used to model neotissue differentiation, scaffold degradation, and their coupled effect phenomenologically. Another example of a more straightforward model is Carlier et al. work [197, 198], in which they solved a set of taxis-diffusion-reaction PDEs describing the evolution of biochemical factors, cells, and extracellular matrices to model the healing process, assuming the entire domain is already occupied by some form of tissue (no void space). Due to the lack of interface capturing, such a model is easier to integrate with the biodegradation model. This approach can be more difficult to validate, but it comes with the advantage of a more straightforward implementation. Looking at the time scales of the both processes however, several weeks for neotissue filling of a 3D porous scaffold of 6 mm cube and several months to years for the degradation of the same scaffold (depending on composition and circumstances), a practical work-around might be to decouple them. This would mean first simulating the neotissue growth until complete filling and only then considering scaffold degradation which focuses all the attention on the zone between the tissue and the scaffold.

6.9 Conclusion

In this chapter, two curvature-driven models of the neotissue growth process were developed using the phase-field and level-set interface tracking methods. The models were used in various 2D and 3D growth simulations with cells seeded on the circumference of basic geometrical primitives, showing the similarities and differences between the phase-field and level-set methods. Additionally, the level-set model was used to simulate tissue growth on open porous scaffolds generated with TPMS geometries, demonstrating the applicability of the developed models for tissue engineering applications. The complications to couple the tissue growth models with the developed biodegradation model in Chapter 3 were also elaborated, in which the potential solutions to address the emerging coupling challenges were discussed.

Chapter 7

Model parallelization for high-performance computing

This chapter is based on previously published content in *The International Journal of High Performance Computing Applications*:

M. Barzegari, and L. Geris, “Highly scalable numerical simulation of coupled reaction–diffusion systems with moving interfaces,” *The International Journal of High Performance Computing Applications*, vol. 36, pp. 198–213, 2022.

A combination of reaction-diffusion models with moving-boundary problems yields a system in which the diffusion (spreading and penetration) and reaction (transformation) evolve the system’s state and geometry over time. These systems can be used in a wide range of engineering applications. In this study, as an example of such a system, the degradation of metallic materials is investigated. A mathematical model is constructed of the diffusion-reaction processes and the movement of corrosion front of a magnesium block floating in a chemical solution. The corresponding parallelized computational model is implemented using the finite element method, and the weak and strong scaling behaviors of the model are evaluated to analyze the performance and efficiency of the employed high-performance computing techniques.

7.1 Introduction

Moving-boundary problems [79] are a subset of the general concept of boundary-value problems which not only require the solution of the underlying partial differential equation (PDE), but also the determination of the boundary of

the domain (or sub-domains) as part of the solution. Moving-boundary problems are usually referred to as Stefan problems [79] and can be used to model a plethora of phenomena ranging from phase separation and multiphase flows in materials engineering to bone development and tumor growth in biology. Reaction-diffusion systems are the mathematical models in which the change of state variables occurs via transformation and spreading. These systems are described by a set of parabolic PDEs and can model a large number of different systems in science and engineering, for instance predator-prey models in biology and chemical components reactions in chemistry [78]. Combining the reaction-diffusion systems with moving-boundary problems provides a way to study the systems in which the diffusion and reaction lead to the change of domain geometry. Such systems have great importance in various real-world scenarios in chemistry and chemical engineering as well as environmental and life sciences.

In this study, the material degradation phenomenon has been investigated as an example of a reaction-diffusion system with moving boundaries, in which the loss of material due to corrosion leads to movement of the interface of the bulk material and surrounding corrosion environment. More specifically, the degradation of magnesium (Mg) in simulated body fluid has been chosen as a case study. Magnesium has been chosen due to its growing usability as a degradable material in biomedicine, where it is usually used in biodegradable implants for bone tissue engineering and cardiovascular applications [5, 71]. The ultimate application of such a model can be then to study the degradation behavior of resorbable Mg-based biomaterials.

A wide range of different techniques has already been developed to study the moving interfaces in reaction-diffusion problems, which can be grouped into 3 main categories: 1) mesh elimination techniques, in which some elements are eliminated to simulate the interface movement (or loss of material in corrosion problems), 2) explicit surface representation, such as the arbitrary Lagrangian-Eulerian (ALE) method, which tracks the interface by moving a Lagrangian mesh inside an Eulerian grid, and 3) implicit surface tracking, in which an implicit criterion is responsible to define the moving interface during the reaction-diffusion process. Related to the aforementioned case study, studies performed by [59] and [63] are examples of the first group. [59] have constructed a simulation of degradation using the mesh elimination technique. [63] have developed a continuous damage (CD) model by using an explicit solver to study the degradation. The work of [66] is an example of the second group as they have developed one of the first models to correlate the mass flux of the metallic ions in the biodegradation interface to the velocity of said interface. This was used to build an ALE model to explicitly track the boundary of the material during degradation. Stud-

ies of the third category are based more on mathematical modeling rather than available models in simulation software packages. This approach results in more flexibility and control over the implementation of the computational model. For instance, [75] have derived a system of mathematical equations to study galvanic corrosion of metals, taking advantage of the level set method (LSM) to track the corrosion front. [68] have used the definition of velocity of the biodegradation interface as the speed of the moving boundary in LSM, enabling them to track the geometrical changes of the material during degradation. Similarly, [199] have used a combination of LSM and extended finite element method (XFEM), a method to model regions with spatial discontinuities, to study the moving corrosion front in the pitting corrosion process. A very similar approach and formulation has been taken by [200] to model localized pitting corrosion. An alternative method for tracking the moving interface is the phase field method, which has been used in a wide range of relevant studies. A comparison between the behavior of phase-field and LSM formulations for an evolving solid-liquid interface has been performed by [201], showing that both methods lead to the same results for diffusion-reaction systems. The approach taken in this study was similar to the one from Bjger et al., where LSM was employed to correlate the diffusion and reaction processes to the movement of the solid-solution interface using continuous variables.

Tracking the moving front at the diffusion interface requires high numerical accuracy of the diffusive state variables, which can be achieved using a refined computational grid. This makes the model computationally intensive, and as a consequence, implementing parallelization is an inevitable aspect of simulating such a model. Such an approach enables the model to simulate large-scale systems with a large number of degrees of freedom (DOF) in 3D with higher performance and efficiency in high-performance computing (HPC) environments. In recent years, parallelization of diffusion-reaction systems simulation has been investigated, but the studies are mainly conducted for stochastic (statistical) models. For instance, [202] have developed a parallel stochastic model for large-scale spatial reaction-diffusion simulation, and similarly, [203] have developed a stochastic high-performance simulator for specific biological applications. Also as an example for massively parallel systems, [204] have conducted a simulation of reaction-diffusion processes in biology using graphics processing units (GPUs). Although stochastic models have more parallel-friendly algorithms, explaining the underlying process, especially when it involves reaction-diffusion processes of chemistry and biology, is less complex and more universal using mechanistic (deterministic) models, which are based on well-developed mathematical models of continuous systems [205]. To the best of authors' knowledge, none of

the previous contributions to the topic of reaction-diffusion systems with moving interfaces has employed parallelization techniques to increase the performance and speed of execution of the model without compromising the accuracy of the interface tracking.

In the current study, we developed a mechanistic model of a reaction-diffusion system coupled with a moving interface problem. Improving the accuracy of the interface capturing requires a refined computational mesh, leading to a more computation-intensive simulation. To overcome this challenge and yield more interactable simulations, scalable parallelization techniques were implemented making the model capable of being run on massively parallel systems to reduce the simulation time. The investigated case-study is the material degradation process. The developed model captures the release of metallic ions to the medium, formation of a protective film on the surface of the material, the effect of presented ions in the medium on the thickness of this protection layer, and tracking of the movement of the corrosion front (Fig. 7.1). The interface tracking was performed using an implicit distance function that defined the position of the interface during degradation. This implicit function was obtained by constructing and solving a level set model. It is also worth noting that in a real-world application, such systems require a calibration (also called parameter estimation or inverse problem), in which the model should be simulated hundreds of times. This makes the parallelization even more crucial for these models.

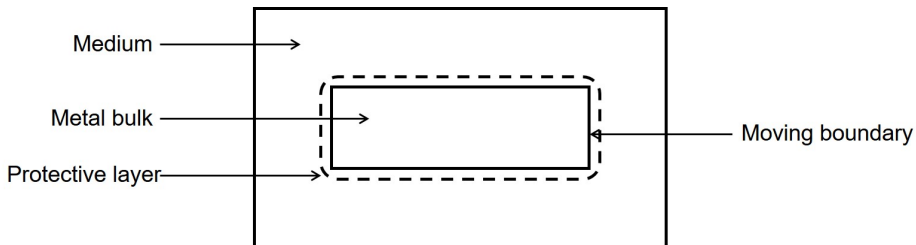


Figure 7.1: A schematic presentation of different components of the developed model for simulation of the degradation process with a moving front.

7.2 Background theory and model description

Before elaborating the parallel implementation strategy, the mathematical model is briefly described in this section. The model is constructed based

on the chemistry of degradation, starting from the previous work by [68], in which the ions can diffuse to the medium and react with each other.

7.2.1 Chemistry of degradation

In metals, degradation occurs through the corrosion process, which usually consists of electrochemical reactions, including anodic and cathodic reactions as well as the formation of side products [2].

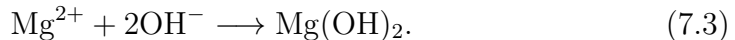
For Mg, the corrosion reactions comprise the following steps [2]: first, the material is released as metallic ions and free electrons, which causes the volume of the bulk material to be reduced:



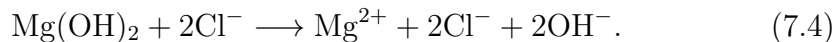
The free electron reduces water to hydrogen gas and hydroxide ions:



Then, with the combination of the metallic and hydroxide ions, a porous film is formed on the surface, slowing down the degradation rate by protecting the material underneath:



With the presence of some specific ions in the surrounding medium, such as chloride ions in a saline solution, the protective film might be broken partially, which contributes to an increase of the rate of degradation:



The degradation process of metals is a continuous repetition of the above reactions.

7.2.2 Reaction-diffusion equation

A reaction-diffusion partial differential equation can describe the state of a reaction-diffusion system by tracking the change of the concentration of the different components of the system over time [78]. The equation is a parabolic PDE and can be expressed as

$$\frac{\partial u}{\partial t} - \nabla \cdot [D\nabla u] = f(u) \quad (7.5)$$

in which the change of the state variable $u = u(\mathbf{x}, t)$, $\mathbf{x} \in \Omega \subset \mathbb{R}^3$ is described as a combination of how it diffuses and how it is produced or eliminated via reactions. The term $f(u)$ is a smooth function that describes the reaction processes.

In the example used in this study, the state variable in Eq. 7.5 is the concentration of effective chemical components involved in the degradation process, namely magnesium ions and the protective layer, denoted by C_{Mg} and C_{Film} respectively.

$$C_{\text{Mg}} = C_{\text{Mg}}(\mathbf{x}, t), \quad C_{\text{Film}} = C_{\text{Film}}(\mathbf{x}, t) \quad \mathbf{x} \in \Omega \subset \mathbb{R}^3 \quad (7.6)$$

Ω is the whole domain of interest, including the bulk material and its surrounding medium. So, by assuming that the reaction rates of Eqs. 7.3 and 7.4 are k_1 and k_2 respectively, one can write the change of those state variables according to Eq. 7.3 and Eq. 7.4 as

$$\frac{\partial C_{\text{Mg}}}{\partial t} = \nabla \cdot (D_{\text{Mg}}^e \nabla C_{\text{Mg}}) - k_1 C_{\text{Mg}} + k_2 C_{\text{Film}} [\text{Cl}]^2 \quad (7.7)$$

$$\frac{\partial C_{\text{Film}}}{\partial t} = k_1 C_{\text{Mg}} - k_2 C_{\text{Film}} [\text{Cl}]^2. \quad (7.8)$$

We assumed that the concentration of the chloride ions is constant (denoted by $[\text{Cl}]$ in the equation) and does not diffuse into the protective film. The missing part of the model described by Eqs. 7.7 and 7.8 is the effect of the protective film on the reduction of the degradation rate. To this end, we defined a saturation term, $(1 - \frac{C_{\text{Film}}}{[\text{Film}]_{\text{max}}})$ for the concentration of Mg ions in the equations. By considering the film's porosity (ϵ), the maximum concentration of the protective layer can be calculated based on its density ($\rho_{\text{Mg(OH)}_2}$):

$$[\text{Film}]_{\text{max}} = \rho_{\text{Mg(OH)}_2} \cdot (1 - \epsilon). \quad (7.9)$$

The defined saturation term acts as a function of space that varies between 0 and 1 in each point. By adding this term to the concentration of Mg ions, we can write

$$\frac{\partial C_{\text{Mg}}}{\partial t} = \nabla \cdot (D_{\text{Mg}}^e \nabla C_{\text{Mg}}) - k_1 C_{\text{Mg}} \left(1 - \frac{C_{\text{Film}}}{[\text{Film}]_{\text{max}}}\right) + k_2 C_{\text{Film}} [\text{Cl}]^2 \quad (7.10)$$

$$\frac{\partial C_{\text{Film}}}{\partial t} = k_1 C_{\text{Mg}} \left(1 - \frac{C_{\text{Film}}}{[\text{Film}]_{\text{max}}}\right) - k_2 C_{\text{Film}} [\text{Cl}]^2. \quad (7.11)$$

Since the film is a porous layer and allows the ions to diffuse through it, the diffusion coefficient in Eq. 7.10 is a function of space and not a constant

value (which is the reason for being denoted as D_{Mg}^e). We can calculate this effective diffusion function by interpolating two values at any point: 1) $D_{\text{Mg}}^e = D_{\text{Mg}}$ when $C_{\text{Film}} = 0$, and 2) $D_{\text{Mg}}^e = \frac{\epsilon}{\tau} D_{\text{Mg}}$ when $C_{\text{Film}} = [\text{Film}]_{\text{max}}$, in which ϵ and τ are the porosity and tortuosity of the protective film, respectively. The interpolation leads to the effective diffusion function:

$$D_{\text{Mg}}^e = D_{\text{Mg}} \left(\left(1 - \frac{C_{\text{Film}}}{[\text{Film}]_{\text{max}}} \right) + \frac{C_{\text{Film}}}{[\text{Film}]_{\text{max}}} \frac{\epsilon}{\tau} \right). \quad (7.12)$$

7.2.3 Level-set method

The level set method is a methodology that allows moving interfaces to be described by an implicit function. In other words, the boundaries of domains can be tracked as a function instead of being explicitly defined. In the level set method, a signed distance function, $\phi = \phi(x, y, z, t)$, describes the distance of each point in space to the interface, and the zero iso-contour of this function implies the interface [80]. In the current study, this function was defined in a way that divides the domain into two subdomains: 1) the bulk material, in which the implicit function is positive ($\phi > 0$), and 2) the medium, in which the function is negative ($\phi < 0$). The interface is defined as the points in space where $\phi = 0$. Fig. 7.2 shows a schematic representation of the solid-medium interface in the current study, in which the interface moves as the material degrades over time.

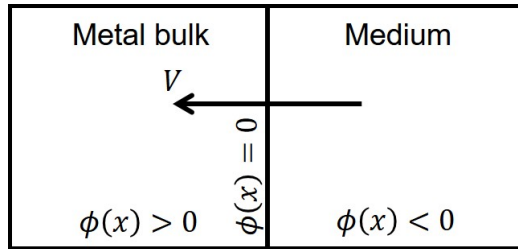


Figure 7.2: A schematic representation of the implicit function definition in the current study. V denotes the shrinkage speed of the interface due to degradation.

The level set equation defines this implicit function. The full level set equation can be written as [80]:

$$\frac{\partial \phi}{\partial t} + \underbrace{\vec{V}^E \cdot \nabla \phi}_{\text{External velocity field}} + \underbrace{V^N |\nabla \phi|}_{\text{Normal direction motion}} = \underbrace{b\kappa |\nabla \phi|}_{\text{Curvature - dependent term}} \quad (7.13)$$

in which the terms correspond to temporal changes, external velocity field effect, normal direction motion, and curvature-dependent interface movement, respectively. $\vec{V^E}$ is the external velocity field, and V^N is the magnitude of the interface velocity along the normal axis. In practical usage, some of the terms are neglected. In this study, perfusion (rotation of the liquid around the bulk sample) is not considered, and the degradation rate does not depend on the curvature of the interface. As a result, by assuming that the interface moves in normal direction only, Eq. 7.13 can be simplified to

$$\frac{\partial \phi}{\partial t} + V^N |\nabla \phi| = 0 \quad (7.14)$$

where V^N is depicted in Fig. 7.2. The Rankine–Hugoniot equation can be used to calculate the interface velocity in mass transfer problems [85]:

$$\{\mathbf{J}(x, t) - (c_{\text{sol}} - c_{\text{sat}}) \mathbf{V}(x, t)\} \cdot n = 0 \quad (7.15)$$

in which \mathbf{J} is the mass flux, c_{sol} is the concentration of the material in the bulk part (i.e. its density), and c_{sat} is the concentration at which the material (here, the ions) saturates through the medium. So, for the investigated Mg degradation problem, Eq. 7.15 will be:

$$D_{\text{Mg}}^e \nabla_n C_{\text{Mg}} - ([\text{Mg}]_{\text{sol}} - [\text{Mg}]_{\text{sat}}) V^N = 0. \quad (7.16)$$

Inserting the obtained velocity of Eq. 7.16 into Eq. 7.14 and considering the direction of the shrinkage velocity, which is in the opposite direction of the surface normal vector, yields

$$\frac{\partial \phi}{\partial t} - \frac{D_{\text{Mg}}^e \nabla_n C_{\text{Mg}}}{[\text{Mg}]_{\text{sol}} - [\text{Mg}]_{\text{sat}}} |\nabla \phi| = 0. \quad (7.17)$$

Eq. 7.17 is the final formulation of the level set equation in the current study, which alongside Eqs. 7.10 and 7.11 forms the mathematical model of degradation of Mg with a moving interface. Eq. 7.17 contributes indirectly to the evolution of Eqs. 7.10 and 7.11 as it defines the boundary, the zero iso-contour of the ϕ function, on which the boundary conditions of the equations are applied.

7.3 Methodology of model implementation

The developed mathematical model comprised of Eqs. 7.10, 7.11, and 7.17 cannot be solved using analytical techniques. The alternative approach in

these scenarios is solving the derived PDEs numerically. In this study, we used a combination of finite element and finite difference methods to solve the aforementioned equations. In the developed numerical model, the PDEs are solved one by one, each of which is a linear equation, so the model implementation follows the principles of solving linear systems. In the following section, only the process to obtain the solution of Eq. 7.10 is described in detail, but the other PDEs were solved using the same principle. Although the adopted finite element method is standard, we elaborate on its derivation to clarify the bottlenecks of the later-discussed implementation.

7.3.1 Finite element discretization (bottleneck of the algorithm)

In order to solve Eq. 7.10 numerically, we used a finite difference scheme for the temporal term and a finite element formulation for the spatial terms. For simplicity of writing, notations of variables are changed, so C_{Mg} is represented as u (the main unknown state variable to find), C_{Film} is denoted by p , $[\text{Cl}]$ is denoted by q , and the saturation term $(1 - \frac{F}{F_{\max}})$ is denoted by s . By doing this, Eq. 7.10 can be written as

$$\frac{\partial u}{\partial t} = \nabla \cdot (D \nabla u) - k_1 s u + k_2 p q^2. \quad (7.18)$$

To obtain the finite element formulation, the weak form of derived PDE is required. In order to get this, we define a space of test functions and then, multiply each term of the PDE by any arbitrary function as a member of this space. The test function space is

$$\mathcal{V} = \{v(\mathbf{x}) | \mathbf{x} \in \Omega, v(\mathbf{x}) \in \mathcal{H}^1(\Omega), \text{ and } v(\mathbf{x}) = 0 \text{ on } \Gamma\} \quad (7.19)$$

in which the Ω is the domain of interest, Γ is the boundary of Ω , and \mathcal{H}^1 denotes the Sobolev space of the domain Ω , which is a space of functions whose derivatives are square-integrable functions in Ω . The solution of the PDE belongs to a trial function space, which is similarly defined as

$$\mathcal{S}_t = \left\{ u(\mathbf{x}, t) | \mathbf{x} \in \Omega, t > 0, u(\mathbf{x}, t) \in \mathcal{H}^1(\Omega), \text{ and } \frac{\partial u}{\partial n} = 0 \text{ on } \Gamma \right\}. \quad (7.20)$$

Then, we multiply Eq. 7.18 to an arbitrary function $v \in \mathcal{V}$:

$$\frac{\partial u}{\partial t} v = \nabla \cdot (D \nabla u) v - k_1 s u v + k_2 p q^2 v. \quad (7.21)$$

Integrating over the whole domain yields:

$$\int_{\Omega} \frac{\partial u}{\partial t} v d\omega = \int_{\Omega} \nabla \cdot (D \nabla u) v d\omega - \int_{\Omega} k_1 s u v d\omega + \int_{\Omega} k_2 p q^2 v d\omega. \quad (7.22)$$

The diffusion term can be split using the integration by parts technique:

$$\int_{\Omega} \nabla \cdot (D \nabla u) v d\omega = \int_{\Omega} \nabla \cdot [v(D \nabla u)] d\omega - \int_{\Omega} (\nabla v) \cdot (D \nabla u) d\omega \quad (7.23)$$

in which the second term can be converted to a surface integral on the domain boundary by applying the Green's divergence theory:

$$\int_{\Omega} \nabla \cdot [v(D \nabla u)] d\omega = \int_{\Gamma} D v \frac{\partial u}{\partial n} d\gamma. \quad (7.24)$$

For the temporal term, we use the finite difference method and apply a first-order backward Euler scheme for discretization, which makes it possible to solve the PDE implicitly:

$$\frac{\partial u}{\partial t} = \frac{u - u^n}{\Delta t} \quad (7.25)$$

where u^n denotes the value of the state variable in the previous time step (or initial condition for the first time step). Inserting Eqs. 7.23, 7.24, and 7.25 into Eq. 7.22 yields:

$$\int_{\Omega} \frac{u - u^n}{\Delta t} v d\omega = \int_{\Gamma} D v \frac{\partial u}{\partial n} d\gamma - \int_{\Omega} D \nabla u \cdot \nabla v d\omega - \int_{\Omega} k_1 s u v d\omega + \int_{\Omega} k_2 p q^2 v d\omega. \quad (7.26)$$

The surface integral is zero because there is a no-flux boundary condition on the boundary of the computational domain (defined in the trial function space according to Eq. 7.20). By reordering the equation, we get the weak form of Eq. 7.18:

$$\int_{\Omega} u v d\omega + \int_{\Omega} \Delta t D \nabla u \cdot \nabla v d\omega + \int_{\Omega} \Delta t k_1 s u v d\omega = \int_{\Omega} u^n v d\omega + \int_{\Omega} \Delta t k_2 p q^2 v d\omega. \quad (7.27)$$

So, the problem is finding a function $u(t) \in \mathcal{S}_t$ such that for all $v \in \mathcal{V}$ Eq. 7.27 would be satisfied. By defining a linear functional $(f, v) = \int_{\Omega} f v d\omega$ and encapsulating the independent concentration terms into $f^n = pq^2$, Eq. 7.27 can be simplified as:

$$(u, v)[1 + \Delta t k_1 s] + \Delta t (D \nabla u, \nabla v) = (u^n, v) + \Delta t (f^n, v) \quad (7.28)$$

which can be further converted to the common form of the weak formulation of time-dependent reaction-diffusion PDEs by multiplying to a new coefficient $\alpha = \frac{1}{1 + \Delta t k_1 s}$:

$$(u, v) + \alpha \Delta t (D \nabla u, \nabla v) = \alpha (u^n, v) + \alpha \Delta t (f^n, v). \quad (7.29)$$

One can approximate the unknown function u in Eq. 7.29 by $u(x) \approx \sum_{i=0}^N c_i \psi_i(x)$, where the ψ_i are the basis functions used to discretize the function space, and c_0, \dots, c_N are the unknown coefficients. The finite element method uses Lagrange polynomials as the basis function and discretizes the computational domain using a new function space \mathcal{V}_h spanned by the basis functions $\{\psi_i\}_{i \in \mathcal{I}_s}$, in which \mathcal{I}_s is defined as $\mathcal{I}_s = \{0, \dots, N\}$, where N denotes the degrees of freedom in the computational mesh. The computational mesh discretizes the space into a finite number of elements, in each of which the ψ_i is non-zero inside the i th element and zero everywhere else. In this study, 1st order Lagrange polynomials were used as the basis functions to define the finite element space.

For 1D elements, a 1st order Lagrange polynomial for the i th element with the width of h can be written as:

$$\psi_i(x) = \begin{cases} 0 & x < x_{i-1} \\ (x - x_{i-1}) / h & x_{i-1} \leq x < x_i \\ 1 - (x - x_i) / h & x_i \leq x < x_{i+1} \\ 0 & x \geq x_{i+1} \end{cases}. \quad (7.30)$$

A similar approach can be applied to define the basis function space in 2D and 3D spaces.

In order to derive a linear system of equations for obtaining the unknown coefficients c_j , we define

$$u = \sum_{j=0}^N c_j \psi_j(\mathbf{x}), \quad u^n = \sum_{j=0}^N c_j^n \psi_j(\mathbf{x}) \quad (7.31)$$

as the definition of the unknown function u and its value in the previous time step u^n . We then insert it into Eq. 7.29, which yields the following equation for each degree of freedom $i = 0, \dots, N$, where the test functions are selected as $v = \psi_i$:

$$\sum_{j=0}^N (\psi_i, \psi_j) c_j + \alpha \Delta t \sum_{j=0}^N (\nabla \psi_i, D \nabla \psi_j) c_j = \sum_{j=0}^N \alpha (\psi_i, \psi_j) c_j^n + \alpha \Delta t (f^n, \psi_i). \quad (7.32)$$

Eq. 7.32 is a linear system:

$$\sum_j A_{i,j} c_j = b_i, \quad (7.33)$$

with

$$A_{i,j} = (\psi_i, \psi_j) + \alpha \Delta t (\nabla \psi_i, D \nabla \psi_j) \quad (7.34)$$

$$b_i = \sum_{j=0}^N \alpha (\psi_i, \psi_j) c_j^n + \alpha \Delta t (f^n, \psi_i), \quad (7.35)$$

which can also be rewritten as:

$$(M + \alpha \Delta t K) c = \alpha M c_1 + \alpha \Delta t f. \quad (7.36)$$

M (which traditionally is called the mass matrix), K (which traditionally is called the stiffness matrix), f , c , and c_1 are defined as:

$$\begin{aligned} M &= \{M_{i,j}\}, \quad M_{i,j} = (\psi_i, \psi_j), \quad i, j \in \mathcal{I}_s \\ K &= \{K_{i,j}\}, \quad K_{i,j} = (\nabla \psi_i, D \nabla \psi_j), \quad i, j \in \mathcal{I}_s \\ f &= \{f_i\}, \quad f_i = (f(\mathbf{x}, t_n), \psi_i), \quad i \in \mathcal{I}_s \\ c &= \{c_i\}, \quad i \in \mathcal{I}_s \\ c_1 &= \{c_i^n\}, \quad i \in \mathcal{I}_s. \end{aligned} \quad (7.37)$$

By solving Eq. 7.33 and substituting the obtained c in Eq. 7.31, u (C_{Mg} in the example in this study) can be calculated in the current time step. As stated before, the same approach can be applied to Eq. 7.11 and Eq. 7.17 to get C_{Film} and ϕ . This procedure is repeated in each time step to compute the values of C_{Mg} , C_{Film} , and ϕ over time.

A common practice to save time for solving Eq. 7.33 for a constant time step size is to compute the left-hand side matrix (A in Eq. 7.34) once and compute only the right-hand side vector of the equation at each time iteration. But in this case, although the time step size is fixed, due to the presence of the α coefficient, the matrix changes along the time. The α coefficient is not constant and should be updated in each time step because it depends on the saturation term s (which is a function of the concentration of the film as can be seen by comparing Eq. 7.10 and Eq. 7.18). In addition to this, the diffusion coefficient is not constant (Eq. 7.12), making the second term in Eq. 7.34 non-constant even in the absence of α coefficient. Consequently, the left-hand side matrix of the Eq. 7.33 cannot be computed before the start of the main time loop, and computing it in each time step is an extra but inevitable computational task in comparison to similar efficient and high-performance finite element implementations. This contributes to a slower algorithm for solving the aforementioned PDEs.

7.3.2 Implementation and parallelization

The model was implemented in FreeFEM [86], which is an open-source PDE solver to facilitate converting the weak formulation (Eq. 7.27) to a linear system $Ax = b$ (with A from Eq. 7.34 and b from Eq. 7.35). The computational mesh was generated using Netgen [91] in the SALOME platform [92] by a set of linear tetrahedral elements, and all the other preprocessing steps were performed in FreeFEM. The mesh was adaptively refined on the material-medium interface in order to increase the accuracy of the level set model. Postprocessing of the results was carried out using Paraview [206].

Computing the diffusion solely in the medium domain causes oscillations close to the interface, and to prevent this, the mass lumping feature of FreeFEM was employed. In this technique, the desired mass matrix is handled node-wise and not element-wise. Technically speaking, this means that the state variable is stored in the mesh nodes, and although this is the natural formulation in the finite difference method, it requires artificial modification in the standard finite element formulation [207]. The mass lumping feature of FreeFEM applies a quadratic formula at the vertices of elements to make the mass matrix diagonal, which contributes positively to the convergence of the solution.

The main parallelization approach for the current study was domain decomposition, in which the mesh is split into smaller domains (can be overlapping or non-overlapping), and the global solution of the linear system is achieved by solving the problem on each smaller local mesh. What really matters in this approach is providing virtual boundary conditions to the smaller sub-domains by ghost elements, transferring neighboring sub-domain solutions [208]. As a result, a high-performance parallelism is feasible by assigning each sub-domain to one processing unit.

In computational science, preconditioning is widely used to enhance the convergence, which means instead of directly working with a linear system $Ax = b$, one can consider the preconditioned system [209]:

$$M^{-1}Ax = M^{-1}b \quad (7.38)$$

in which the M^{-1} is the preconditioner. In the current study, we considered this approach for both the domain composition and the solution of the linear system. We opted to use an overlapping Schwarz method for domain decomposition, in which the mesh is first divided into a graph of N non-overlapping meshes using METIS (or ParMETIS) [127]. Then, by defining a positive number δ , the overlapping decomposition $\{\mathcal{T}_i^\delta\}_{1 \leq i \leq N}$ can be created recursively for each sub-mesh $\{\mathcal{T}_i\}_{1 \leq i \leq N}$ by adding all adjacent elements of $\mathcal{T}_i^{\delta-1}$ to it. Then, the finite element space \mathcal{V}_h (Eq. 7.19) can be mapped to

the local space $\{\mathcal{V}_i^\delta\}_{1 \leq i \leq N}$ by considering the restrictions $\{R_i\}_{1 \leq i \leq N}$ and a local partition of unity $\{D_i\}_{1 \leq i \leq N}$ such that:

$$\sum_{j=1}^N R_j^\top D_j R_j = I_{n \times n} \quad (7.39)$$

where I and n denote identity matrix and the global number of unknowns, respectively [210].

In this study, we decomposed the mesh by using the one-level preconditioner Restricted Additive Schwarz (RAS):

$$M_{\text{RAS}}^{-1} = \sum_{i=1}^N R_i^\top D_i A_i^{-1} R_i \quad (7.40)$$

in which $\{A_i\}_{1 \leq i \leq N}$ is the local operator of the sub-matrices [210]. For this purpose, we took advantage of the HPDDM (high-performance domain decomposition methods) package interface in FreeFEM [90]. The partitioned mesh is shown in Fig. 7.3. The effect of the construction of these local sub-domains on the sparsity pattern of the global matrix is also depicted in Fig. 7.4. The global matrix is a sparse matrix according to Eq. 7.34 and the definition of the basis function ψ .

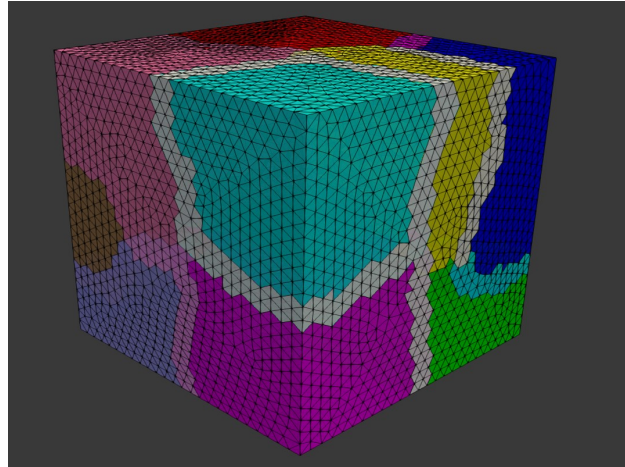


Figure 7.3: Overlapping domain decomposition in the current study. Each color shows a separate sub-domain, and the narrow lighter bands are the overlapped regions.

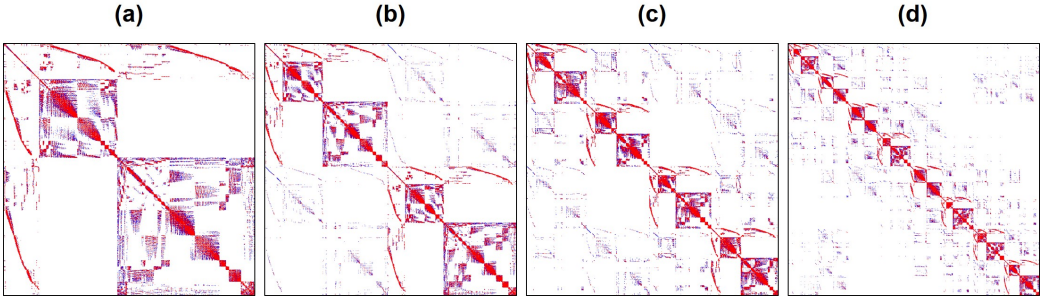


Figure 7.4: Comparison of the sparsity patterns (highlighting non-zero elements) of the global matrix A for a different number of decomposed domains
a: 1 domain b: 2 sub-domains c: 4 sub-domains d: 8 sub-domains.

Generally, two categories of methods have been used to solve a large linear system of equations on parallel machines: direct solvers (e.g. Multi-frontal Massively Parallel Sparse, MUMPS [211]) and iterative solvers (e.g. Generalized Minimal Residual Method, GMRES [88]). While direct solvers are quite robust, they suffer from the memory requirement problem on large systems. Inversely, iterative solvers are quite efficient on memory consumption, but similar to other iterative approaches, they are not very reliable in some cases [212]. Direct solvers modify the matrix by factorization (e.g. Cholesky decomposition), but an iterative solver does not manipulate the matrix and works solely using basic algebraic operations. However, for an efficient usage of iterative solvers, a proper preconditioner is crucial [212]. By evaluating and comparing the performance of the aforementioned methods for the current model, we decided to use an iterative approach using the Krylov subspaces (KSP) method, in which we preconditioned the equation using a proper preconditioner (Eq. 7.38) and then solved it with an iterative solver.

Krylov methods have been frequently used by researchers as robust iterative approaches to parallelism [213]. What matters in this regard is ensuring proper scaling of the parallelized algorithm for both the assembling of the matrices and the solution of the linear system of equations. One good solution to this challenge is taking advantage of HPC-ready mathematical libraries to achieve efficient distributed-memory parallelism through the Message Passing Interface (MPI). In the current study, we used the PETSc (Portable, Extensible Toolkit for Scientific Computation) library [89], which provides a collection of high-performance preconditioners and solvers for this purpose.

In order to yield the highest performance, a variety of different combinations of KSP types and preconditioners were evaluated, such as Conju-

gate Gradients (CG) [214], Successive Over-Relaxation (SOR) [215], block Jacobi, and Algebraic Multigrid (AMG) [128], to name a few. The performance tests results are presented in the appendix section of this chapter. The best performance for the reaction-diffusion system model was achieved using the HYPRE preconditioner [87] and the GMRES solver [88]. This was the combination used for all the performance analysis tests.

7.3.3 Level-set issues

As mentioned before, in order to track the interface of the bulk material and the surrounding fluid, an implicit signed distance function is defined as the solution of Eq. 7.17. This equation can be solved using the aforementioned finite element discretization, but in a practical implementation, there are usually a couple of problems associated with this PDE.

The first issue is defining D_{Mg}^e and $\nabla_n C_{\text{Mg}}$ on the moving interface. To ensure correct boundary conditions for Eq. 7.16, the value of C_{Mg} is set constant on the whole bulk material by using the penalty method. As a result, the implicit interface is not necessarily aligned on the computational mesh. Although this is a beneficial fact for the interface tracking, it inserts the problem of overestimation of C_{Mg} on the nodes close to the interface, which makes it difficult to calculate $\nabla_n C_{\text{Mg}}$ on these nodes correctly. The same problem exists for calculating D_{Mg}^e . To overcome this issue, the values of C_{Mg} and D_{Mg}^e are calculated at the distance h from the interface in the normal direction (towards the medium), where h is the edge size of the smallest element of the computational mesh.

The next issue is a well-known problem of the level set method: if the velocity of the interface is not constant (as in Eq. 7.13), the level set function ϕ may become distorted by having too flat or too steep gradients close to the moving front. This could cause unwanted movements of the interface. The problem becomes even worse when the distance function is advected. A solution to this issue is re-initializing the distance function in each time step (re-distancing), but this operation requires solving a new PDE. From numerical investigations, it has been observed that this operation inserts new errors in the numerical computation of the level set equation [216]. This can be resolved by improving the method of reconstruction of the distance function [216].

However, re-initialization results in another issue on a massively parallel implementation: as the mesh is partitioned into smaller sub-meshes, it is not feasible anymore to evaluate the distance to the interface globally on each sub-domain. As a result, the inverse process of domain decomposition should be taken to assemble the mesh again. This can be done by the re-

striction matrix and the partition of unity (defined in Eqs. 7.39 and 7.40), but it is rather a very inefficient procedure regarding the parallelization of the simulation and results in a long execution time in each time step.

In the current study, the distance function ϕ was initialized only once at the beginning of the simulation. The re-initialization process was unnecessary in this case because according to Eq. 7.17, the distance function is advected only in the regions where there is a gradient of the concentration of Mg ions, which means that advection is applied only on the regions close to the interface in the medium. This prevented the whole distance function of being distorted, and as a result, it was not required to re-initialize it in each time step. This also removed the need for inverting the decomposition process.

7.3.4 Simulation setup

In order to verify the performance of the developed model, a degradation experiment was reconstructed in-silico, in which the degradation of a block of Mg (with the size of $13mm \times 13mm \times 4mm$) was investigated in a simulated body fluid solution. All the experimental parameter data (used to setup the simulation), as well as the degradation rates (used to calibrate and validate the numerical model) were extracted from [36].

As can be seen in Eqs. 7.1 and 7.2, each mole removed from the Mg block corresponds to one mole of the produced hydrogen. As a result, instead of a direct measurement of mass loss, one can collect and measure the amount of produced hydrogen to monitor the degradation rate. This is a common way of reporting degradation in this type of studies [53]. In order to get this quantity out of the developed model, we used the level set model output. The total mass loss of Mg at each desired time can be calculated based on the movement of the corrosion front:

$$Mg_{lost} = \int_{\Omega_+(t)} Mg_{solid} dV - \int_{\Omega_+(0)} Mg_{solid} dV \quad (7.41)$$

where $\Omega_+(t) = \{\mathbf{x} : \phi(\mathbf{x}, t) \geq 0\}$. It is worth noting that this integration should be performed by ignoring the ghost elements generated in the mesh partitioning process, otherwise the calculated material loss will be higher than the real value. Then, the amount of formed hydrogen gas can be calculated based on the ideal gas law:

$$H_f = \frac{Mg_{lost}}{Mg_{mol}} \frac{RT}{PA} \quad (7.42)$$

in which R is the universal gas constant, P is the pressure, T is the solution temperature, A is the exposed corrosion surface area (which can be computed

using the level set function), and Mg_{mol} is the molar mass of Mg. Plotting a comparison of the predicted and experimentally obtained values of hydrogen can show the overall validity of the mathematical model because both the diffusion-reaction equations and the level set equation contribute to the prediction made by the computational model.

The geometry of the simulation experiment is depicted in Fig. 7.5. Based on this geometry, an Eulerian computational mesh was constructed by generating tetrahedral elements on the whole domain, including the Mg block and the medium. This resulted in 830,808 elements with a total of 143,719 DOFs for each PDE (Eqs. 7.10, 7.11, and 7.17), which indicates the size of matrix A in Eq. 7.34. Model parameters and material properties were obtained from [68]. The diffusion coefficient of Mg was calculated using an inverse problem setup in which a Bayesian optimization process [93] was used to run the simulation code multiple times and minimize the difference of the model output and the experimental data reported by [36]. A time step convergence study was performed to measure the sensitivity of the model to the time stepping parameter, and based on the results, the time step value was set to 0.025 hours.

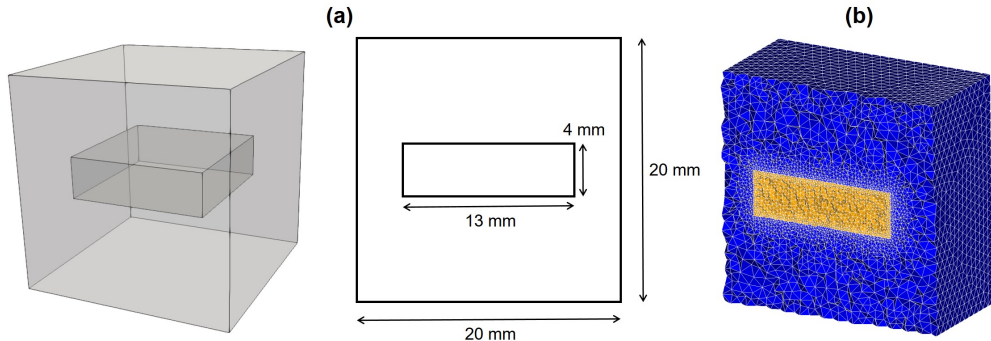


Figure 7.5: Representation of the experimental set-up simulated to perform numerical validation of the developed model and evaluate parallel performance. a) A cuboid of Mg (with the size of $13\text{mm} \times 13\text{mm} \times 4\text{mm}$) is floating inside a simulated body fluid solution to investigate the degradation process, b) a cross-section of the computational mesh, refined on the metal-medium interface to increase the interface capturing accuracy.

7.3.5 Performance analysis

To investigate the performance and scaling behavior of the implemented parallel code, we conducted a set of weak-scaling and strong-scaling tests on the

computational model. To do this, the time required to solve each PDE in each time step was measured in a simulation. This acted as a rough estimation of the time required in each time step because it ignores all the other factors contributing to speedup results such as communication costs, load imbalance, limited memory bandwidth, and parallelization-caused overhead.

Weak-scaling was evaluated by dividing the computational domain into smaller sub-domains (each of which was $\frac{1}{16}$ of the whole domain, Fig. 7.6) and conducting simulation experiments with 1, 2, 4, and 8 computational cores in a way that the number of processors corresponded to the number of employed sub-domains. In Fig. 7.6 the upper row shows different domains as an accumulation of the smaller divisions, and the lower row shows the corresponding domain decomposition for parallel computing by depicting each processing unit in a different color. In fact, it demonstrates the concept of increasing the number of MPI processing units as we increase the size of the problem.

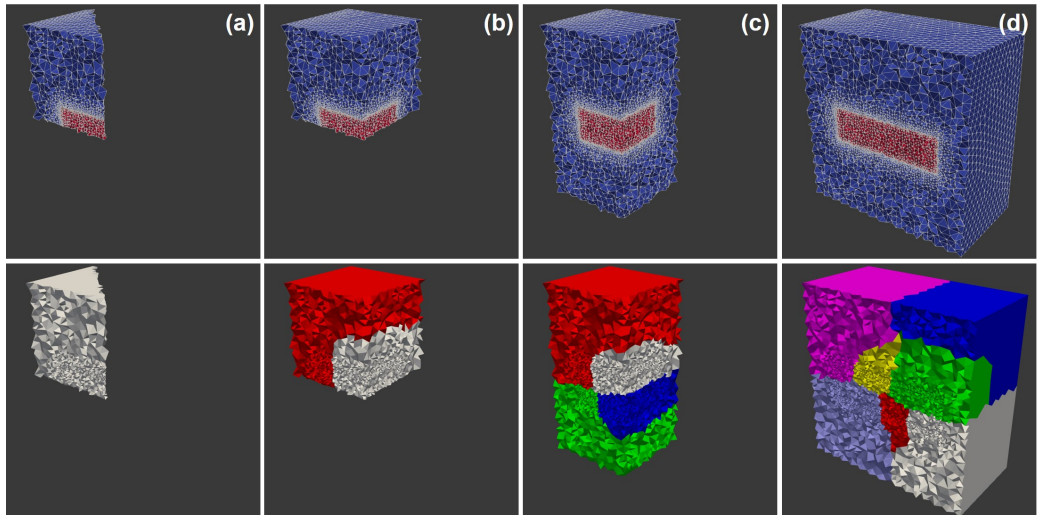


Figure 7.6: Models used for weak-scaling, in which the number of elements was doubled each time while doubling the number of computational cores. Upper row: actual computational domain in which colors show the medium (blue) and the material block (red). Lower row: domain decomposition for parallelization, colors show different decomposed mesh parts (distributed to different MPI processing units). Each column corresponds to a different simulation with a: 1 MPI unit, b: 2 MPI units, c: 4 MPI units, and d: 8 MPI units.

After calculating the speedup of each test (by comparing the differences in execution time), we can use Gustafson's law [217] to calculate the sequential

and parallelizable portion of computation in the current implementation in weak-scaling evaluation:

$$\text{Speedup} = f + (1 - f) \times N \quad (7.43)$$

where N is the total number of computational cores, f is the fraction of operations in the computation that are sequential, and as a result, $1 - f$ is the fraction of the execution time spent on the parallelizable part.

The strong-scaling evaluation was performed using the entire domain. The evaluation was done using 1, 8, 16, 40, 60, 90, 200, and 300 MPI cores. In strong-scaling, Amdahl's law [218] is used to calculate the portion of the algorithm that runs in parallel:

$$\text{Speedup} = \frac{1}{f + \frac{1-f}{N}} \quad (7.44)$$

in which the parameters are the same as Eq. 7.43.

7.3.6 Compute environment

Simulations were conducted on the VSC (Flemish Supercomputer Center) supercomputer with the availability of Intel CPUs in three different micro-architectures: Ivy Bridge, Haswell, and Skylake. Due to a better performance, the strong and weak-scaling measurements were solely performed on the Skylake nodes. On this supercomputer, we made use of 3 nodes, 36 cores each, with 576 GB of the total memory, each node holding 2 Intel Xeon Gold 6132 CPUs with a base clock speed of 2.6 GHz. The nodes in the supercomputer are connected using an InfiniBand EDR network (bandwidth 25 Gb/s). For interprocess communication, Intel's MPI implementation 2018 was used.

7.4 Results

7.4.1 Numerical simulation results

The performed numerical simulation produces the output of three main quantities: the concentration of the Mg ions in the medium (as the solution of Eq. 7.10), the concentration of the protective film (as the solution of Eq. 7.11), and the level set function values at each element (as the solution of Eq. 7.17). In addition to this, a quantitative prediction of the mass loss is also generated according to Eqs. 7.41 and 7.42.

In order to have quantitative predictions, the coefficients of Eqs. 7.10 and 7.11 (diffusion rates and reaction rates) should be calibrated using an inverse

problem. Fig. 7.7 shows the results produced by the computational model after this parameter estimation stage. A narrow layer of the protective film is formed on the surface of the Mg block, and the volume of produced hydrogen gas is compared with values obtained from experiments. Additionally, by plotting the zero iso-contour of the level set function, we can obtain the shape of the material block as it degrades during the degradation process (i.e. tracking the moving corrosion front). This is depicted by the grey surface in Fig. 7.7.

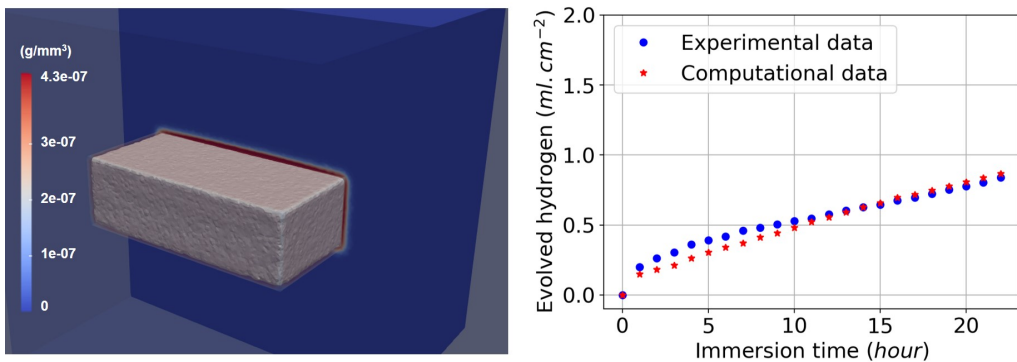


Figure 7.7: Numerical simulation result. Left: formation of a protective layer on the surface of the Mg block (red region). Right: comparison of the produced hydrogen (a surrogate for the material loss) in the computational model and the experimental data, which is a validation of the full model as both the reaction-diffusion equations and the level-set equation are involved in the computation of this quantity.

7.4.2 Weak and strong scaling results

Weak-scaling results are plotted in Fig. 7.8, in which the execution time of each time step is broken down into the time spent on each PDE. The results show good scalability of the parallel implementation.

Speedup and parallel efficiency of the weak-scaling experiment is plotted in Fig. 7.9. By fitting a curve based on the Gustafson equation (Eq. 7.43) on the obtained results (Fig. 7.9), the sequential proportion of the current implementation was calculated to be 18%, which means that 82 percent of the code can be parallelized, which is a proper but not an ideal scalability.

The strong-scaling results are plotted in Fig. 7.10, which shows a better scalability in comparison to the weak-scaling test. For a better representation, exact measured values are presented in Table 7.1.

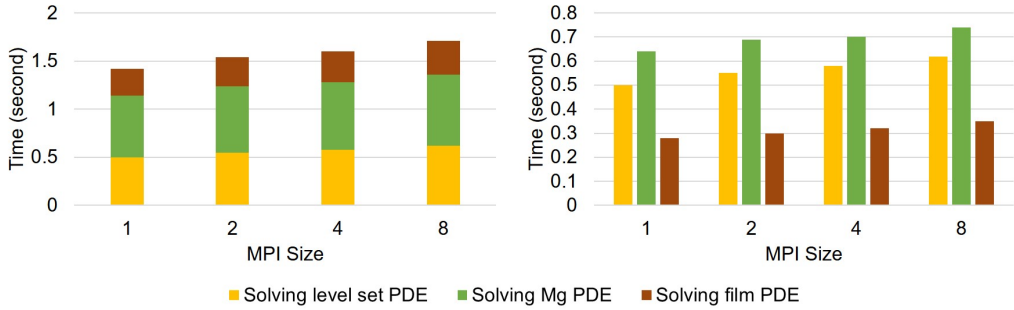


Figure 7.8: Weak-scaling test result. Results are broken down into contributions for each PDE, which are plotted cumulatively and separately in the left and right plot, respectively.

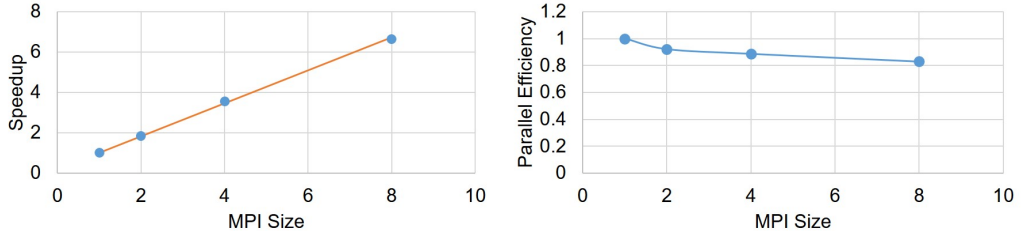


Figure 7.9: Speed-up and parallel efficiency of the weak-scaling experiment. The orange line in the left plot shows the fitted curve based on the Gustafson equation.

Similar to weak-scaling results, Fig. 7.11 demonstrates the speedup and parallel efficiency of the developed code for strong-scaling evaluation. From the results, it is obvious that increasing the number of cores leads to a better performance but a lower efficiency. By fitting Amdahl's equation (Eq. 7.44) on the obtained speedup results (Fig. 7.11), f was obtained as 0.01, which means in strong-scaling terms that 99% of the code can run in parallel.

7.5 Discussion

In this investigation, the derivation and implementation of a reaction-diffusion model with moving boundaries were presented. Such an approach finds application in many scientific and engineering problems. The target application in the current work was the degradation of a bulk metal cuboid in a liquid environment, specifically Mg in an aqueous ion solution as a representative

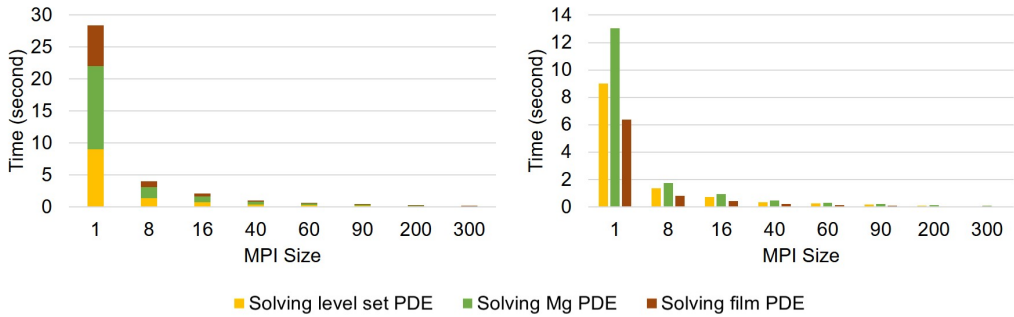


Figure 7.10: Strong-scaling test result. Results are broken down into contributions for each PDE, which are plotted cumulatively and separately in the left and right plot, respectively.

Table 7.1: Strong-scaling test result, presented by the execution time of each PDE in simulations with a different number of employed MPI cores.

| MPI Size | 1 | 8 | 16 | 40 | 60 | 90 | 200 | 300 |
|---------------|----------------|-------|------|------|------|------|------|------|
| Solution time | LS PDE | 9 | 1.39 | 0.75 | 0.36 | 0.26 | 0.19 | 0.11 |
| of each time | Mg PDE | 13.04 | 1.76 | 0.94 | 0.46 | 0.31 | 0.22 | 0.12 |
| step (s) | Film PDE | 6.38 | 0.84 | 0.45 | 0.21 | 0.14 | 0.09 | 0.05 |
| | Total time (s) | 28.42 | 3.99 | 2.14 | 1.03 | 0.71 | 0.5 | 0.28 |
| | | | | | | | | 0.07 |
| | | | | | | | | 0.09 |
| | | | | | | | | 0.04 |

for temporary medical devices. The simulations were based on the corrosion of Mg metal to Mg ions to form a film of Mg hydroxide that partially protects the metal block from further degradation except where this film is impacted by reaction with other ions in the environment (such as chloride ion). The reactive moving boundary problem was cast in the form of equations in which the change of the concentrations of the different chemical components is represented by parabolic PDEs. The coupled equations depend on several kinetic constants that have been calibrated from experiments. The moving interface between the metal bulk and the liquid phase was described by an implicit function using the level set method. The derivation led to equations that require the use of numerical techniques for which a combination of finite difference and finite element methods was implemented. As the required high accuracy on the moving interface results in an increase in computation time, parallelization was crucial for the computational model to decrease the execution time of the simulations. The results of the total execution time in each time step (Table 7.1) clearly indicate that without the paralleliza-

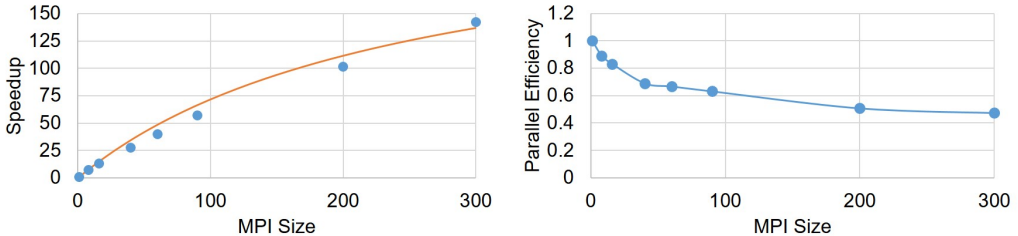


Figure 7.11: Speed-up and parallel efficiency of the strong-scaling experiment. The orange line in the left plot is the fitted equation based on the Amdahl rule.

tion, the simulation of the model is slow and as a result, less interactable for real-world simulation analyses. Considering the properly employed parallelization, the computational time has been decreased noticeably for the investigated case-study.

The output of the conducted numerical simulation demonstrates that the developed mathematical model is capable of capturing the degradation interface movement and of modeling of the underlying chemical phenomena. The predicted mass loss is in line with the experimental results, and the simulated corrosion behavior is as expected for such a system. It is worth noting that the chosen system is highly idealized as a model for medical devices. A more realistic chemical environment would contain many more species that play a role in the formation of either soluble ions or the protective film. Moreover, in real-world scenarios, corrosion occurs in a more complex way than the simplified one described in this paper, which will have a significant influence on the local concentration of ions in the regions close to the solid surface. Nevertheless, the developed framework is capable of capturing these physical and chemical phenomena in the future by simply adding the appropriate terms to the base PDEs without any major changes in the computational model. Furthermore, although it requires some changes to the parallelization approach, the addition of the fluid flow around the block is feasible by adding convective terms to form a reaction-diffusion-convection system. Such a system can be used to model relevant systems such as experimental bioreactor setups in biology and medical sciences.

The parallel algorithm was implemented using a domain decomposition method. Standard domain decomposition preconditioners, such as restricted additive Schwarz, are widely used for parallel implementation of computational models. In a parallel implementation, such preconditioners bring the benefit of relatively low communication costs [209]. Beside this, the

formed linear system of equations in each partition of the mesh was solved using Krylov methods by taking advantage of the highly-efficient preconditioners and iterative solvers of the PETSc library. According to the obtained results, the employed parallelization approach of the current study yields reasonable scaling with respect to the available computational resources (or the number of sub-domains). Out of multiple evaluations, the best performance was achieved using the preconditioner/solver combination of HYPRE/GMRES, which is in agreement with findings in more specific studies in this regard [219].

To evaluate the scaling performance of the implemented parallelism, a set of weak and strong scaling tests was conducted. In weak-scaling, the main approach is changing the problem size proportional to the change in the available computing resources. In an ideal parallelization, we expect that the speedup remains the same for all the setups because we provide double resources as we double the size of the problem. In strong-scaling, the size of the problem remains constant, but the number of computing units increases. So, in an ideal case, we should observe a double speedup as the number of computing units doubles. By fitting Gustafson's and Amdahl's laws on the scaling test results (Figs. 7.9 and 7.11), the maximum parallelizable portion of the code was calculated to be 82% and 99% for the weak-scaling and strong-scaling tests, respectively. This is a reasonable theoretical scaling for both cases. However, it should be noted that Gustafson's and Amdahl's laws are only applicable and valid for ideal parallelization cases, a fact that can be considered as the simplification made for performing the analysis made in the current research.

The obtained scaling behavior is similar to other conducted studies for diffusion or diffusion-convection systems [220, 221], in which the efficiency of the parallelization decreases with increasing the number of available computational resources. The reason behind this behavior in the current model seems to lie in the mesh partitioning process. Indeed, the mesh is partitioned into semi-equal partitions, each of which has the same number of elements, but the main computation is only carried out on the nodes located outside the degrading material block (i.e. in the medium). In other words, the computational resources assigned to the nodes inside the material bulk do not contribute significantly to the simulation. This limitation can be prevented by modifying the mesh generation process in a way that a lower number of elements be generated inside the material block, but doing this requires remeshing of the interior region as the moving interface approaches it, which imposes even more complexity to the algorithm due to the partitioned mesh. Another bottleneck of the current model, as discussed before, routed in the non-constant right-hand matrix of the linear system (Eq. 7.33), which re-

quires computing the A matrix (Eq. 7.34) in each time step and leads to a slower execution time.

One important point in this regard is that the way that the results are interpreted does not necessarily imply the true scaling behavior of the system. Indeed, it is more like a surrogate model of the system performance. The correct methodology for obtaining true scaling factors is rather starting from an analysis of the code and time used in each routine for a non-parallel run. Then, based on the fraction of routines that are possible to execute in parallel, one can get a theoretical limit for the speedup. This will be reduced by practical limitations such as load balancing and communication costs of the network. Since it is a theoretical limit, it is not fully correct to ignore those extra parts and use the execution time to invert the relation to predict the fraction of the code that is parallel. However, for a complex computational model like the one that was developed in the current study, doing such a measurement of each routine is very difficult due to the complexity of the orchestrated libraries and tools. As a result, we were limited to use the roughly approximated speedup limit to evaluate the scaling of the constructed model. Regarding the scalability results, it is worth mentioning that although having studies with thousands of MPI ranks is more common in this field, due to the limitation we faced in accessing computational resources, the maximum number of employed cores were limited to 300. The goal of the current study was to demonstrate the scalability of the developed model on massively parallel systems, and the behavior of the model in moving from 90 cores to 300 shows the consistency in the performed performance analysis. As a result, we expect to see the same scalability behavior for problems in a larger scale with a higher number of employed computing nodes.

7.6 Conclusion

In this work, a mathematical model of a reaction-diffusion system with a moving front was constructed, and the corresponding computational model was implemented using the finite element method. In order to correlate the diffusion phenomenon to the moving boundary position, high numerical accuracy is necessary at the diffusion interface, which requires a finer discretization of space near the moving front. This leads to an expensive computational model, which makes employing HPC techniques crucial in order to improve the simulation execution time. To this end, a high-performance domain decomposition approach was employed to partition the mesh and distribute the workload to available computing resources. Additionally, an efficient preconditioner/solver combination for reaction-diffusion PDEs was used to

optimize the model to be used for the high-performance simulation of large scale systems in which the movement of system boundaries is controlled by reaction-diffusion phenomena.

The investigated problem was the degradation of a magnesium block inside a solution, in which the surface of the block moves due to the reaction-diffusion phenomena in the metal-medium interface. The implemented model showed a good agreement with the experimental data in terms of the degradation rate and chemical reactions, and the parallel efficiency and linear scalability were appropriate in performance evaluation tests. For the next stage of the study, it could be interesting to evaluate the model and its performance on a much larger system and tune the resources and memory usage by testing different preconditioners and solvers.

7.A Comparing the performance of different combinations of KSP types and preconditioners

In order to yield the highest performance, a variety of different combinations of KSP types and preconditioners were evaluated, such as Conjugate Gradients (CG), Successive Over-Relaxation (SOR), block Jacobi, and Algebraic Multigrid (AMG), and Generalized Minimal Residual Method (GMRES). The tests were performed using 6 MPI cores on an Ubuntu machine with an Intel Core i7-8850H CPU (2.6 GHz of clock speed) and a total available memory of 32 GB.

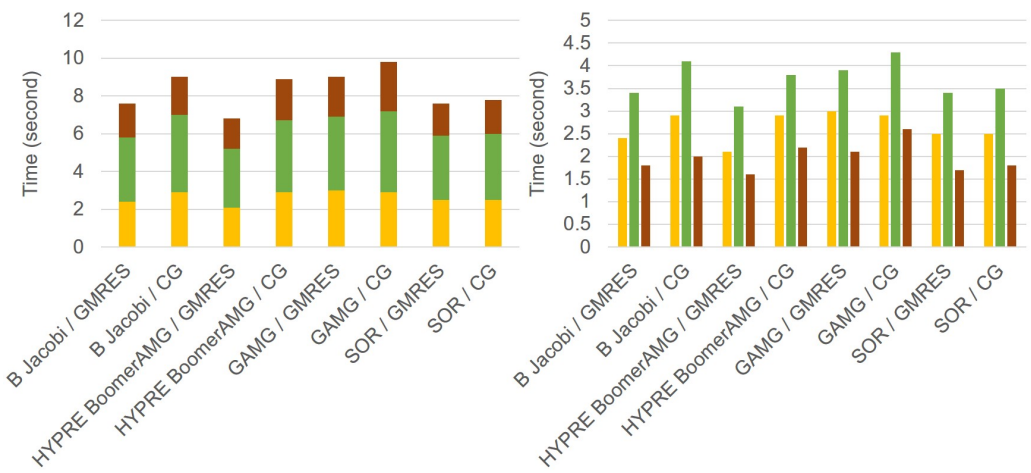


Figure 7.12: Performance test result for various combinations of preconditioners and solvers. Results are broken down into contributions for each PDE, which are plotted cumulatively and separately in the left and right plots, respectively.

Table 7.2: Performance test result for various combinations of preconditioners and solvers, presented by the execution time of each PDE.

| | | B Jacobi / GMRES | B Jacobi / CG | HYPRE / GMRES | HYPRE / CG | GAMG / GMRES | GAMG / CG | SOR / GMRES | SOR / CG |
|---|----------|------------------|---------------|---------------|------------|--------------|-----------|-------------|----------|
| Solution time of each time step (s) | LS PDE | 2.4 | 2.9 | 2.1 | 2.9 | 3.0 | 2.9 | 2.5 | 2.5 |
| | Mg PDE | 3.4 | 4.1 | 3.1 | 3.8 | 3.9 | 4.3 | 3.4 | 3.5 |
| | Film PDE | 1.8 | 2.0 | 1.6 | 2.2 | 2.1 | 2.6 | 1.7 | 1.8 |
| Total time (s) | | 7.6 | 9.0 | 6.8 | 8.9 | 9.0 | 9.8 | 7.6 | 7.8 |

Bibliography

- [1] Y. Gao, L. Wang, and Y. Fan, “Biomechanics of magnesium-based implant during tissue repair,” in *Biomechanics of Injury and Prevention*, pp. 335–361, Springer Nature Singapore, 2022.
- [2] Y. Zheng, X. Gu, and F. Witte, “Biodegradable metals,” *Materials Science and Engineering: R: Reports*, vol. 77, pp. 1–34, mar 2014.
- [3] Y. Liu, Y. Zheng, X.-H. Chen, J.-A. Yang, H. Pan, D. Chen, L. Wang, J. Zhang, D. Zhu, S. Wu, K. W. K. Yeung, R.-C. Zeng, Y. Han, and S. Guan, “Fundamental theory of biodegradable metals—definition, criteria, and design,” *Advanced Functional Materials*, vol. 29, p. 1805402, feb 2019.
- [4] H.-S. Han, S. Loffredo, I. Jun, J. Edwards, Y.-C. Kim, H.-K. Seok, F. Witte, D. Mantovani, and S. Glyn-Jones, “Current status and outlook on the clinical translation of biodegradable metals,” *Materials Today*, vol. 23, pp. 57–71, mar 2019.
- [5] D. Zhao, F. Witte, F. Lu, J. Wang, J. Li, and L. Qin, “Current status on clinical applications of magnesium-based orthopaedic implants: A review from clinical translational perspective,” *Biomaterials*, vol. 112, pp. 287–302, jan 2017.
- [6] Z. ZHEN, T. fei XI, and Y. feng ZHENG, “A review on in vitro corrosion performance test of biodegradable metallic materials,” *Transactions of Nonferrous Metals Society of China*, vol. 23, pp. 2283–2293, aug 2013.
- [7] R. Willumeit-Römer, “The interface between degradable mg and tissue,” *JOM*, vol. 71, pp. 1447–1455, feb 2019.
- [8] J. Venezuela and M. Dargusch, “The influence of alloying and fabrication techniques on the mechanical properties, biodegradability and

- biocompatibility of zinc: A comprehensive review,” *Acta Biomaterialia*, vol. 87, pp. 1–40, mar 2019.
- [9] E. Mostaed, M. Sikora-Jasinska, J. W. Drelich, and M. Vedani, “Zinc-based alloys for degradable vascular stent applications,” *Acta Biomaterialia*, vol. 71, pp. 1–23, apr 2018.
 - [10] M. Schinhammer, A. C. Hänzi, J. F. Löffler, and P. J. Uggowitzer, “Design strategy for biodegradable fe-based alloys for medical applications,” *Acta Biomaterialia*, vol. 6, pp. 1705–1713, may 2010.
 - [11] M. Esmaily, J. Svensson, S. Fajardo, N. Birbilis, G. Frankel, S. Virtanen, R. Arrabal, S. Thomas, and L. Johansson, “Fundamentals and advances in magnesium alloy corrosion,” *Progress in Materials Science*, vol. 89, pp. 92–193, aug 2017.
 - [12] B. Heublein, “Biocorrosion of magnesium alloys: a new principle in cardiovascular implant technology?,” *Heart*, vol. 89, pp. 651–656, jun 2003.
 - [13] M. P. Staiger, A. M. Pietak, J. Huadmai, and G. Dias, “Magnesium and its alloys as orthopedic biomaterials: A review,” *Biomaterials*, vol. 27, pp. 1728–1734, mar 2006.
 - [14] J. Walker, S. Shadanbaz, T. B. F. Woodfield, M. P. Staiger, and G. J. Dias, “Magnesium biomaterials for orthopedic application: A review from a biological perspective,” *Journal of Biomedical Materials Research Part B: Applied Biomaterials*, vol. 102, pp. 1316–1331, jan 2014.
 - [15] F. Cecchinato, N. A. Agha, A. H. Martinez-Sanchez, B. J. C. Luthringer, F. Feyerabend, R. Jimbo, R. Willumeit-Römer, and A. Wennerberg, “Influence of magnesium alloy degradation on undifferentiated human cells,” *PLOS ONE*, vol. 10, p. e0142117, nov 2015.
 - [16] E. Crubzy, P. Murail, L. Girard, and J.-P. Bernadou, “False teeth of the roman world,” *Nature*, vol. 391, pp. 29–29, jan 1998.
 - [17] J.-L. Wang, J.-K. Xu, C. Hopkins, D. H.-K. Chow, and L. Qin, “Biodegradable magnesium-based implants in orthopedics—a general review and perspectives,” *Advanced Science*, vol. 7, p. 1902443, feb 2020.
 - [18] B. Wegener, A. Sichler, S. Milz, C. Sprecher, K. Pieper, W. Hermanns, V. Jansson, B. Nies, B. Kieback, P. E. Müller, V. Wegener,

- and P. Quadbeck, “Development of a novel biodegradable porous iron-based implant for bone replacement,” *Scientific Reports*, vol. 10, jun 2020.
- [19] G. Gąsior, J. Szczepański, and A. Radtke, “Biodegradable iron-based materials—what was done and what more can be done?,” *Materials*, vol. 14, p. 3381, jun 2021.
 - [20] H.-S. Han, I. Jun, H.-K. Seok, K.-S. Lee, K. Lee, F. Witte, D. Mantovani, Y.-C. Kim, S. Glyn-Jones, and J. R. Edwards, “Biodegradable magnesium alloys promote angio-osteogenesis to enhance bone repair,” *Advanced Science*, vol. 7, p. 2000800, jun 2020.
 - [21] G. K. Levy, J. Goldman, and E. Aghion, “The prospects of zinc as a structural material for biodegradable implants—a review paper,” *Materials*, vol. 7, p. 402, oct 2017.
 - [22] X. Liu, J. Sun, Y. Yang, Z. Pu, and Y. Zheng, “In vitro investigation of ultra-pure zn and its mini-tube as potential bioabsorbable stent material,” *Materials Letters*, vol. 161, pp. 53–56, dec 2015.
 - [23] J. Vormann, “Magnesium: nutrition and metabolism,” *Molecular Aspects of Medicine*, vol. 24, pp. 27–37, feb 2003.
 - [24] R. J. Elin, “Magnesium metabolism in health and disease,” *Disease-a-Month*, vol. 34, pp. 166–218, apr 1988.
 - [25] F. Witte, “The history of biodegradable magnesium implants: A review,” *Acta Biomaterialia*, vol. 6, pp. 1680–1692, may 2010.
 - [26] N. Ikeo, R. Nakamura, K. Naka, T. Hashimoto, T. Yoshida, T. Urade, K. Fukushima, H. Yabuuchi, T. Fukumoto, Y. Ku, and T. Mukai, “Fabrication of a magnesium alloy with excellent ductility for biodegradable clips,” *Acta Biomaterialia*, vol. 29, pp. 468–476, jan 2016.
 - [27] R. Erbel, C. D. Mario, J. Bartunek, J. Bonnier, B. de Bruyne, F. R. Eberli, P. Erne, M. Haude, B. Heublein, M. Horrigan, C. Ilsley, D. Böse, J. Koolen, T. F. Lüscher, N. Weissman, and R. Waksman, “Temporary scaffolding of coronary arteries with bioabsorbable magnesium stents: a prospective, non-randomised multicentre trial,” *The Lancet*, vol. 369, pp. 1869–1875, jun 2007.
 - [28] Y. Sotomi, Y. Onuma, C. Collet, E. Tenekecioglu, R. Virmani, N. S. Kleiman, and P. W. Serruys, “Bioresorbable scaffold,” *Circulation Research*, vol. 120, pp. 1341–1352, apr 2017.

- [29] H. M. Garcia-Garcia, M. Haude, K. Kuku, A. Hideo-Kajita, H. Ince, A. Abizaid, R. Tölg, P. A. Lemos, C. von Birgelen, E. H. Christiansen, W. Wijns, J. Escaned, J. Dijkstra, and R. Waksman, “In vivo serial invasive imaging of the second-generation drug-eluting absorbable metal scaffold (magmaris — DREAMS 2g) in de novo coronary lesions: Insights from the BIOSOLVE-II first-in-man trial,” *International Journal of Cardiology*, vol. 255, pp. 22–28, mar 2018.
- [30] A. LAMBOTTE, “Technique et indication des prothèses dans le traitement des fractures,” *Presse med*, vol. 17, p. 321, 1909.
- [31] A. Lambotte, “L’utilisation du magnésium comme matériel perdu dans l’ostéosynthèse,” *Bull Mem Soc Nat Chir*, vol. 28, no. 3, pp. 1325–1334, 1932.
- [32] F. Witte, V. Kaese, H. Haferkamp, E. Switzer, A. Meyer-Lindenberg, C. Wirth, and H. Windhagen, “In vivo corrosion of four magnesium alloys and the associated bone response,” *Biomaterials*, vol. 26, pp. 3557–3563, jun 2005.
- [33] C. Wang, D. Mei, G. Wiese, L. Wang, M. Deng, S. V. Lamaka, and M. L. Zheludkevich, “High rate oxygen reduction reaction during corrosion of ultra-high-purity magnesium,” *npj Materials Degradation*, vol. 4, dec 2020.
- [34] S. Huang, B. Wang, X. Zhang, F. Lu, Z. Wang, S. Tian, D. Li, J. Yang, F. Cao, L. Cheng, Z. Gao, Y. Li, K. Qin, and D. Zhao, “High-purity weight-bearing magnesium screw: Translational application in the healing of femoral neck fracture,” *Biomaterials*, vol. 238, p. 119829, apr 2020.
- [35] D. Mei, S. V. Lamaka, X. Lu, and M. L. Zheludkevich, “Selecting medium for corrosion testing of bioabsorbable magnesium and other metals – a critical review,” *Corrosion Science*, vol. 171, p. 108722, jul 2020.
- [36] D. Mei, S. V. Lamaka, J. Gonzalez, F. Feyerabend, R. Willumeit-Römer, and M. L. Zheludkevich, “The role of individual components of simulated body fluid on the corrosion behavior of commercially pure mg,” *Corrosion Science*, vol. 147, pp. 81–93, feb 2019.
- [37] R.-C. Zeng, Y. Hu, S.-K. Guan, H.-Z. Cui, and E.-H. Han, “Corrosion of magnesium alloy AZ31: The influence of bicarbonate, sulphate, hy-

- drogen phosphate and dihydrogen phosphate ions in saline solution,” *Corrosion Science*, vol. 86, pp. 171–182, sep 2014.
- [38] S. Johnston, M. Dargusch, and A. Atrens, “Building towards a standardised approach to biocorrosion studies: a review of factors influencing mg corrosion in vitro pertinent to in vivo corrosion,” *Science China Materials*, vol. 61, pp. 475–500, dec 2017.
 - [39] S. V. Lamaka, J. Gonzalez, D. Mei, F. Feyerabend, R. Willumeit-Römer, and M. L. Zheludkevich, “Local pH and its evolution near mg alloy surfaces exposed to simulated body fluids,” *Advanced Materials Interfaces*, vol. 5, p. 1800169, jun 2018.
 - [40] D. Mei, S. V. Lamaka, C. Feiler, and M. L. Zheludkevich, “The effect of small-molecule bio-relevant organic components at low concentration on the corrosion of commercially pure mg and mg-0.8ca alloy: An overall perspective,” *Corrosion Science*, vol. 153, pp. 258–271, jun 2019.
 - [41] B. Hadzima, M. Mhaede, and F. Pastorek, “Electrochemical characteristics of calcium-phosphatized AZ31 magnesium alloy in 0.9 % NaCl solution,” *Journal of Materials Science: Materials in Medicine*, vol. 25, pp. 1227–1237, jan 2014.
 - [42] X. Lu, Y. Li, P. Ju, Y. Chen, J. Yang, K. Qian, T. Zhang, and F. Wang, “Unveiling the inhibition mechanism of an effective inhibitor for AZ91 mg alloy,” *Corrosion Science*, vol. 148, pp. 264–271, mar 2019.
 - [43] Y. Li, X. Lu, K. Wu, L. Yang, T. Zhang, and F. Wang, “Exploration the inhibition mechanism of sodium dodecyl sulfate on mg alloy,” *Corrosion Science*, vol. 168, p. 108559, may 2020.
 - [44] A. Atrens, G.-L. Song, M. Liu, Z. Shi, F. Cao, and M. S. Dargusch, “Review of recent developments in the field of magnesium corrosion,” *Advanced Engineering Materials*, vol. 17, pp. 400–453, jan 2015.
 - [45] C. Schille, M. Braun, H. Wendel, L. Scheideler, N. Hort, H.-P. Reichel, E. Schweizer, and J. Geis-Gerstorfer, “Corrosion of experimental magnesium alloys in blood and PBS: A gravimetric and microscopic evaluation,” *Materials Science and Engineering: B*, vol. 176, pp. 1797–1801, dec 2011.
 - [46] D. Xue, Y. Yun, Z. Tan, Z. Dong, and M. J. Schulz, “In vivo and in vitro degradation behavior of magnesium alloys as biomaterials,”

Journal of Materials Science & Technology, vol. 28, pp. 261–267, mar 2012.

- [47] Y. Xin, T. Hu, and P. K. Chu, “Degradation behaviour of pure magnesium in simulated body fluids with different concentrations of hco₃,” *Corrosion Science*, vol. 53, pp. 1522–1528, apr 2011.
- [48] S. Johnston, Z. Shi, and A. Atrens, “The influence of pH on the corrosion rate of high-purity mg, AZ91 and ZE41 in bicarbonate buffered hanks’ solution,” *Corrosion Science*, vol. 101, pp. 182–192, dec 2015.
- [49] S. Johnston, Z. Shi, J. Venezuela, C. Wen, M. S. Dargusch, and A. Atrens, “Investigating mg biocorrosion in vitro: Lessons learned and recommendations,” *JOM*, vol. 71, pp. 1406–1413, jan 2019.
- [50] M. Pogorielov, E. Husak, A. Solodivnik, and S. Zhdanov, “Magnesium-based biodegradable alloys: Degradation, application, and alloying elements,” *Interventional Medicine and Applied Science*, vol. 9, pp. 27–38, mar 2017.
- [51] J. Walker, S. Shadanbaz, N. T. Kirkland, E. Stace, T. Woodfield, M. P. Staiger, and G. J. Dias, “Magnesium alloys: Predicting in vivo corrosion with in vitro immersion testing,” *Journal of Biomedical Materials Research Part B: Applied Biomaterials*, vol. 100B, pp. 1134–1141, feb 2012.
- [52] X. Gu, Y. Zheng, Y. Cheng, S. Zhong, and T. Xi, “In vitro corrosion and biocompatibility of binary magnesium alloys,” *Biomaterials*, vol. 30, pp. 484–498, feb 2009.
- [53] N. I. Z. Abidin, B. Rolfe, H. Owen, J. Malisano, D. Martin, J. Hofstetter, P. J. Uggowitzer, and A. Atrens, “The in vivo and in vitro corrosion of high-purity magnesium and magnesium alloys WZ21 and AZ91,” *Corrosion Science*, vol. 75, pp. 354–366, oct 2013.
- [54] H. Wang and Z. Shi, “In vitro biodegradation behavior of magnesium and magnesium alloy,” *Journal of Biomedical Materials Research Part B: Applied Biomaterials*, vol. 98B, pp. 203–209, jul 2011.
- [55] W. R. Barfield, G. Colbath, J. D. DesJardins, Y. H. An, and L. A. Hartsock, “The potential of magnesium alloy use in orthopaedic surgery,” *Current Orthopaedic Practice*, vol. 23, pp. 146–150, mar 2012.

- [56] A. H. M. Sanchez, B. J. Luthringer, F. Feyerabend, and R. Willumeit, “Mg and mg alloys: How comparable are in vitro and in vivo corrosion rates? a review,” *Acta Biomaterialia*, vol. 13, pp. 16–31, feb 2015.
- [57] E. L. Boland, R. Shine, N. Kelly, C. A. Sweeney, and P. E. McHugh, “A review of material degradation modelling for the analysis and design of bioabsorbable stents,” *Annals of Biomedical Engineering*, vol. 44, pp. 341–356, aug 2015.
- [58] J. A. Sanz-Herrera and E. Reina-Romo, “Continuum modeling and simulation in bone tissue engineering,” *Applied Sciences*, vol. 9, p. 3674, sep 2019.
- [59] Y. Gao, L. Wang, X. Gu, Z. Chu, M. Guo, and Y. Fan, “A quantitative study on magnesium alloy stent biodegradation,” *Journal of Biomechanics*, vol. 74, pp. 98–105, jun 2018.
- [60] D. Liu, S. Hu, X. Yin, J. Liu, Z. Jia, and Q. Li, “Degradation mechanism of magnesium alloy stent under simulated human micro-stress environment,” *Materials Science and Engineering: C*, vol. 84, pp. 263–270, mar 2018.
- [61] E. L. Boland, J. A. Grogan, and P. E. McHugh, “Computational modelling of magnesium stent mechanical performance in a remodelling artery: Effects of multiple remodelling stimuli,” *International Journal for Numerical Methods in Biomedical Engineering*, vol. 35, aug 2019.
- [62] A.-K. Gartzke, S. Julmi, C. Klose, A.-C. Waselau, A. Meyer-Lindenberg, H. J. Maier, S. Besdo, and P. Wriggers, “A simulation model for the degradation of magnesium-based bone implants,” *Journal of the Mechanical Behavior of Biomedical Materials*, vol. 101, p. 103411, jan 2020.
- [63] D. Gastaldi, V. Sassi, L. Petrini, M. Vedani, S. Trasatti, and F. Migliavacca, “Continuum damage model for bioresorbable magnesium alloy devices — application to coronary stents,” *Journal of the Mechanical Behavior of Biomedical Materials*, vol. 4, pp. 352–365, apr 2011.
- [64] W. Shi, H. Li, K. Mitchell, C. Zhang, T. Zhu, Y. Jin, and D. Zhao, “A multi-dimensional non-uniform corrosion model for bioabsorbable metallic vascular stents,” *Acta Biomaterialia*, vol. 131, pp. 572–580, sep 2021.

- [65] S. Ahmed, J. Ward, and Y. Liu, “Numerical modelling of effects of biphasic layers of corrosion products to the degradation of magnesium metal in vitro,” *Materials*, vol. 11, p. 1, dec 2017.
- [66] J. Grogan, S. Leen, and P. McHugh, “A physical corrosion model for bioabsorbable metal stents,” *Acta Biomaterialia*, vol. 10, pp. 2313–2322, may 2014.
- [67] Z. Shen, M. Zhao, D. Bian, D. Shen, X. Zhou, J. Liu, Y. Liu, H. Guo, and Y. Zheng, “Predicting the degradation behavior of magnesium alloys with a diffusion-based theoretical model and in vitro corrosion testing,” *Journal of Materials Science & Technology*, vol. 35, pp. 1393–1402, jul 2019.
- [68] P. Bajger, J. M. A. Ashbourn, V. Manhas, Y. Guyot, K. Lietaert, and L. Geris, “Mathematical modelling of the degradation behaviour of biodegradable metals,” *Biomechanics and Modeling in Mechanobiology*, vol. 16, pp. 227–238, aug 2016.
- [69] J. Sanz-Herrera, E. Reina-Romo, and A. Boccaccini, “In silico design of magnesium implants: Macroscopic modeling,” *Journal of the Mechanical Behavior of Biomedical Materials*, vol. 79, pp. 181–188, mar 2018.
- [70] T. Albaraghtheh, R. Willumeit-Römer, and B. Zeller-Plumhoff, “In silico studies of magnesium-based implants: A review of the current stage and challenges,” *Journal of Magnesium and Alloys*, vol. 10, pp. 2968–2996, nov 2022.
- [71] Y. Chen, Z. Xu, C. Smith, and J. Sankar, “Recent advances on the development of magnesium alloys for biodegradable implants,” *Acta Biomaterialia*, vol. 10, pp. 4561–4573, nov 2014.
- [72] Y. Qin, P. Wen, H. Guo, D. Xia, Y. Zheng, L. Jauer, R. Poprawe, M. Voshage, and J. H. Schleifenbaum, “Additive manufacturing of biodegradable metals: Current research status and future perspectives,” *Acta Biomaterialia*, vol. 98, pp. 3 – 22, 2019.
- [73] U. Riaz, I. Shabib, and W. Haider, “The current trends of mg alloys in biomedical applications—a review,” *Journal of Biomedical Materials Research Part B: Applied Biomaterials*, dec 2018.
- [74] Y. Xin, K. Huo, H. Tao, G. Tang, and P. K. Chu, “Influence of aggressive ions on the degradation behavior of biomedical magnesium alloy in

physiological environment,” *Acta Biomaterialia*, vol. 4, pp. 2008–2015, nov 2008.

- [75] J. W. Wilder, C. Clemons, D. Golovaty, K. L. Kreider, G. W. Young, and R. S. Lillard, “An adaptive level set approach for modeling damage due to galvanic corrosion,” *Journal of Engineering Mathematics*, vol. 91, pp. 121–142, nov 2014.
- [76] W. Sun, G. Liu, L. Wang, T. Wu, and Y. Liu, “An arbitrary lagrangian–eulerian model for studying the influences of corrosion product deposition on bimetallic corrosion,” *Journal of Solid State Electrochemistry*, vol. 17, pp. 829–840, nov 2012.
- [77] Y. Wang, J. Pan, X. Han, C. Sinka, and L. Ding, “A phenomenological model for the degradation of biodegradable polymers,” *Biomaterials*, vol. 29, no. 23, pp. 3393–3401, 2008.
- [78] P. Grindrod, *The theory and applications of reaction-diffusion equations : patterns and waves*. Oxford University Press, 1996.
- [79] J. Crank, *Free and Moving Boundary Problems*. OUP Oxford, 1987.
- [80] S. O. Ronald Fedkiw, *Level Set Methods and Dynamic Implicit Surfaces*. Springer New York, 2002.
- [81] M. Strebl, M. Bruns, and S. Virtanen, “Editors’ choice—respirometric in situ methods for real-time monitoring of corrosion rates: Part i. atmospheric corrosion,” *Journal of The Electrochemical Society*, vol. 167, p. 021510, jan 2020.
- [82] E. L. Silva, S. V. Lamaka, D. Mei, and M. L. Zheludkevich, “The reduction of dissolved oxygen during magnesium corrosion,” *ChemistryOpen*, vol. 7, pp. 664–668, aug 2018.
- [83] P. Grathwohl, *Diffusion in Natural Porous Media: Contaminant Transport, Sorption/Desorption and Dissolution Kinetics*. Springer US, 1998.
- [84] D. Höche, “Simulation of corrosion product deposit layer growth on bare magnesium galvanically coupled to aluminum,” *Journal of The Electrochemical Society*, vol. 162, pp. C1–C11, nov 2014.
- [85] S. Scheiner and C. Hellmich, “Stable pitting corrosion of stainless steel as diffusion-controlled dissolution process with a sharp moving electrode boundary,” *Corrosion Science*, vol. 49, pp. 319–346, feb 2007.

- [86] F. Hecht, “New development in freefem++,” *J. Numer. Math.*, vol. 20, no. 3-4, pp. 251–265, 2012.
- [87] R. D. Falgout and U. M. Yang, “hypre: A library of high performance preconditioners,” in *Lecture Notes in Computer Science*, pp. 632–641, Springer Berlin Heidelberg, 2002.
- [88] Y. Saad and M. H. Schultz, “Gmres: A generalized minimal residual algorithm for solving nonsymmetric linear systems,” *SIAM Journal on Scientific and Statistical Computing*, vol. 7, no. 3, pp. 856–869, 1986.
- [89] S. Balay, S. Abhyankar, M. F. Adams, J. Brown, P. Brune, K. Buschelman, L. Dalcin, A. Dener, V. Eijkhout, W. D. Gropp, D. Karpeyev, D. Kaushik, M. G. Knepley, D. A. May, L. C. McInnes, R. T. Mills, T. Munson, K. Rupp, P. Sanan, B. F. Smith, S. Zampini, H. Zhang, and H. Zhang, “PETSc Web page.” <https://www.mcs.anl.gov/petsc>, 2019.
- [90] P. Jolivet, F. Hecht, F. Nataf, and C. Prud’homme, “Scalable domain decomposition preconditioners for heterogeneous elliptic problems,” in *Proceedings of the International Conference on High Performance Computing, Networking, Storage and Analysis, SC ’13*, (New York, NY, USA), Association for Computing Machinery, 2013.
- [91] J. Schöberl, “NETGEN an advancing front 2d/3d-mesh generator based on abstract rules,” *Computing and Visualization in Science*, vol. 1, pp. 41–52, jul 1997.
- [92] A. Ribes and C. Caremoli, “Salome platform component model for numerical simulation,” in *31st Annual International Computer Software and Applications Conference - Vol. 2 - (COMPSAC 2007)*, IEEE, jul 2007.
- [93] J. Mockus, *Bayesian Approach to Global Optimization*. Springer Netherlands, 1989.
- [94] M. Mehrian, Y. Guyot, I. Papantoniou, S. Olofsson, M. Sonnaert, R. Misener, and L. Geris, “Maximizing neotissue growth kinetics in a perfusion bioreactor: An in silico strategy using model reduction and bayesian optimization,” *Biotechnology and Bioengineering*, vol. 115, pp. 617–629, dec 2017.

- [95] S. H. Lee and J. C. Rasaiah, “Proton transfer and the mobilities of the H⁺ and OH⁻ ions from studies of a dissociating model for water,” *The Journal of Chemical Physics*, vol. 135, p. 124505, sep 2011.
- [96] J. S. H. Graham C. Hill, *Chemistry in Context - Laboratory Manual*. Oxford University Press, 2001.
- [97] M. Abdalla, A. Joplin, M. Elahinia, and H. Ibrahim, “Corrosion modeling of magnesium and its alloys for biomedical applications: Review,” *Corrosion and Materials Degradation*, vol. 1, pp. 219–248, jul 2020.
- [98] R. J. Santucci, M. E. McMahon, and J. R. Scully, “Utilization of chemical stability diagrams for improved understanding of electrochemical systems: evolution of solution chemistry towards equilibrium,” *npj Materials Degradation*, vol. 2, jan 2018.
- [99] K. B. Deshpande, “Numerical modeling of micro-galvanic corrosion,” *Electrochimica Acta*, vol. 56, pp. 1737–1745, jan 2011.
- [100] O. Dolgikh, H. Simillion, S. V. Lamaka, A. C. Bastos, H. B. Xue, M. G. Taryba, A. R. Oliveira, C. Allély, B. V. D. Bossche, K. V. D. Bergh, J. D. Strycker, and J. Deconinck, “Corrosion protection of steel cut-edges by hot-dip galvanized al(zn,mg) coatings in 1 wt% NaCl: Part II. numerical simulations,” *Materials and Corrosion*, vol. 70, pp. 780–792, jan 2019.
- [101] V. I. Sikavitsas, G. N. Bancroft, J. J. Lemoine, M. A. K. Liebschner, M. Dauner, and A. G. Mikos, “Flow perfusion enhances the calcified matrix deposition of marrow stromal cells in biodegradable nonwoven fiber mesh scaffolds,” *Annals of Biomedical Engineering*, vol. 33, pp. 63–70, jan 2005.
- [102] W. L. Grayson, D. Marolt, S. Bhumiratana, M. Fröhlich, X. E. Guo, and G. Vunjak-Novakovic, “Optimizing the medium perfusion rate in bone tissue engineering bioreactors,” *Biotechnology and Bioengineering*, vol. 108, pp. 1159–1170, dec 2010.
- [103] M. Sonnaert, I. Papantoniou, V. Bloemen, G. Kerckhofs, F. P. Luyten, and J. Schrooten, “Human periosteal-derived cell expansion in a perfusion bioreactor system: proliferation, differentiation and extracellular matrix formation,” *Journal of Tissue Engineering and Regenerative Medicine*, vol. 11, pp. 519–530, sep 2014.

- [104] M. J. Song, D. Dean, and M. L. K. Tate, “Mechanical modulation of nascent stem cell lineage commitment in tissue engineering scaffolds,” *Biomaterials*, vol. 34, pp. 5766–5775, jul 2013.
- [105] R. McCoy, C. Jungreuthmayer, and F. O'Brien, “Influence of flow rate and scaffold pore size on cell behavior during mechanical stimulation in a flow perfusion bioreactor,” *Biotechnology and Bioengineering*, vol. 109, pp. 1583–1594, jan 2012.
- [106] J. Rauh, F. Milan, K.-P. Günther, and M. Stiehler, “Bioreactor systems for bone tissue engineering,” *Tissue Engineering Part B: Reviews*, vol. 17, pp. 263–280, aug 2011.
- [107] I. Papantoniou, Y. C. Chai, F. P. Luyten, and J. Schrooten, “Process quality engineering for bioreactor-driven manufacturing of tissue-engineered constructs for bone regeneration,” *Tissue Engineering Part C: Methods*, vol. 19, pp. 596–609, aug 2013.
- [108] J. Wang, V. Giridharan, V. Shanov, Z. Xu, B. Collins, L. White, Y. Jang, J. Sankar, N. Huang, and Y. Yun, “Flow-induced corrosion behavior of absorbable magnesium-based stents,” *Acta Biomaterialia*, vol. 10, pp. 5213–5223, dec 2014.
- [109] J. Lévesque, H. Hermawan, D. Dubé, and D. Mantovani, “Design of a pseudo-physiological test bench specific to the development of biodegradable metallic biomaterials,” *Acta Biomaterialia*, vol. 4, pp. 284–295, mar 2008.
- [110] N. Li, C. Guo, Y. H. Wu, Y. F. Zheng, and L. Q. Ruan, “Comparative study on corrosion behaviour of pure mg and WE43 alloy in static, stirring and flowing hank's solution,” *Corrosion Engineering, Science and Technology*, vol. 47, pp. 346–351, aug 2012.
- [111] K. Jafarzadeh, T. Shahrabi, and A. A. Oskouei, “Novel approach using EIS to study flow accelerated pitting corrosion of AA5083-h321 aluminum–magnesium alloy in NaCl solution,” *Journal of Applied Electrochemistry*, vol. 39, pp. 1725–1731, mar 2009.
- [112] Y. Chen, S. Zhang, J. Li, Y. Song, C. Zhao, and X. Zhang, “Dynamic degradation behavior of MgZn alloy in circulating m-SBF,” *Materials Letters*, vol. 64, pp. 1996–1999, sep 2010.

- [113] F. Witte, K. Bobe, and M. Meier, “Mri based perfusion measurements in bone after implantation of biodegradable magnesium rods,” *Eur Cells Mater*, vol. 26, 01 2013.
- [114] S. Hiromoto, A. Yamamoto, N. Maruyama, H. Somekawa, and T. Mukai, “Influence of pH and flow on the polarisation behaviour of pure magnesium in borate buffer solutions,” *Corrosion Science*, vol. 50, pp. 3561–3568, dec 2008.
- [115] K. D. Efird, “Flow effects on corrosion,” in *Uhlig's Corrosion Handbook*, pp. 203–213, John Wiley & Sons, Inc., apr 2011.
- [116] L. Xu and Y. Cheng, “Effect of fluid hydrodynamics on flow-assisted corrosion of aluminum alloy in ethylene glycol–water solution studied by a microelectrode technique,” *Corrosion Science*, vol. 51, pp. 2330–2335, oct 2009.
- [117] W. M. H. Versteeg, *Introduction to Computational Fluid Dynamics*, An. Pearson Education (US), 2007.
- [118] A. Sharma, *Introduction to Computational Fluid Dynamics*. Springer International Publishing, 2022.
- [119] D. W. Hutmacher and H. Singh, “Computational fluid dynamics for improved bioreactor design and 3d culture,” *Trends in Biotechnology*, vol. 26, pp. 166–172, apr 2008.
- [120] M. S. Hossain, X. B. Chen, and D. J. Bergstrom, “Investigation of the in vitro culture process for skeletal-tissue-engineered constructs using computational fluid dynamics and experimental methods,” *Journal of Biomechanical Engineering*, vol. 134, nov 2012.
- [121] A. R. Patrachari, J. T. Podichetty, and S. V. Madihally, “Application of computational fluid dynamics in tissue engineering,” *Journal of Bioscience and Bioengineering*, vol. 114, pp. 123–132, aug 2012.
- [122] T. J. Chung, *Computational Fluid Dynamics*. Cambridge University Press, 2014.
- [123] A. Quarteroni, “Navier-stokes equations,” in *Numerical Models for Differential Problems*, pp. 429–482, Springer Milan, 2014.
- [124] V. Girault and P.-A. Raviart, *Finite Element Approximation of the Navier-Stokes Equations*. Springer Berlin Heidelberg, 1979.

- [125] H. Elman, D. Silvester, and A. Wathen, *Finite Elements and Fast Iterative Solvers with Applications in Incompressible Fluid Dynamics*. Oxford University PressOxford, jun 2014.
- [126] F. de Vuyst, “Numerical modeling of transport problems using freefem++ software – with examples in biology, CFD, traffic flow and energy transfer.” Lecture, Sept. 2013.
- [127] G. Karypis and V. Kumar, “A fast and high quality multilevel scheme for partitioning irregular graphs,” *SIAM J. Sci. Comput.*, vol. 20, p. 359–392, Dec. 1998.
- [128] S. F. McCormick, *Multigrid methods*. SIAM, 1987.
- [129] Y. Guyot, I. Papantoniou, F. P. Luyten, and L. Geris, “Coupling curvature-dependent and shear stress-stimulated neotissue growth in dynamic bioreactor cultures: a 3d computational model of a complete scaffold,” *Biomechanics and Modeling in Mechanobiology*, vol. 15, pp. 169–180, jan 2016.
- [130] H. G. Weller, G. Tabor, H. Jasak, and C. Fureby, “A tensorial approach to computational continuum mechanics using object-oriented techniques,” *Computers in Physics*, vol. 12, no. 6, p. 620, 1998.
- [131] M. Barzegari, D. Mei, S. V. Lamaka, and L. Geris, “Computational modeling of degradation process of biodegradable magnesium biomaterials,” *Corrosion Science*, vol. 190, p. 109674, 2021.
- [132] G. Chourdakis, K. Davis, B. Rodenberg, M. Schulte, F. Simonis, B. Uekermann, G. Abrams, H. Bungartz, L. Cheung Yau, I. Desai, K. Eder, R. Hertrich, F. Lindner, A. Rusch, D. Sashko, D. Schneider, A. Totounferoush, D. Volland, P. Vollmer, and O. Koseomur, “pre-CICE v2: A sustainable and user-friendly coupling library [version 1; peer review: 2 approved],” *Open Research Europe*, vol. 2, no. 51, 2022.
- [133] L.-N. Zhang, Z.-T. Hou, X. Ye, Z.-B. Xu, X.-L. Bai, and P. Shang, “The effect of selected alloying element additions on properties of mg-based alloy as bioimplants: A literature review,” *Frontiers of Materials Science*, vol. 7, pp. 227–236, jul 2013.
- [134] X. Li, X. Liu, S. Wu, K. Yeung, Y. Zheng, and P. K. Chu, “Design of magnesium alloys with controllable degradation for biomedical implants: From bulk to surface,” *Acta Biomaterialia*, vol. 45, pp. 2–30, nov 2016.

- [135] A. Atrens, Z. Shi, S. U. Mehreen, S. Johnston, G.-L. Song, X. Chen, and F. Pan, “Review of mg alloy corrosion rates,” *Journal of Magnesium and Alloys*, vol. 8, pp. 989–998, dec 2020.
- [136] N. Kirkland, N. Birbilis, and M. Staiger, “Assessing the corrosion of biodegradable magnesium implants: A critical review of current methodologies and their limitations,” *Acta Biomaterialia*, vol. 8, pp. 925–936, mar 2012.
- [137] N. A. Agha, F. Feyerabend, B. Mihailova, S. Heidrich, U. Bismayer, and R. Willumeit-Römer, “Magnesium degradation influenced by buffering salts in concentrations typical of in vitro and in vivo models,” *Materials Science and Engineering: C*, vol. 58, pp. 817–825, jan 2016.
- [138] L.-Y. Cui, Y. Hu, R.-C. Zeng, Y.-X. Yang, D.-D. Sun, S.-Q. Li, F. Zhang, and E.-H. Han, “New insights into the effect of tris-HCl and tris on corrosion of magnesium alloy in presence of bicarbonate, sulfate, hydrogen phosphate and dihydrogen phosphate ions,” *Journal of Materials Science & Technology*, vol. 33, pp. 971–986, sep 2017.
- [139] M. B. Kannan, H. Khakbaz, and A. Yamamoto, “Understanding the influence of HEPES buffer concentration on the biodegradation of pure magnesium: An electrochemical study,” *Materials Chemistry and Physics*, vol. 197, pp. 47–56, aug 2017.
- [140] Y. Song, D. Shan, R. Chen, F. Zhang, and E.-H. Han, “Biodegradable behaviors of AZ31 magnesium alloy in simulated body fluid,” *Materials Science and Engineering: C*, vol. 29, pp. 1039–1045, apr 2009.
- [141] P. Jiang, C. Blawert, N. Scharnagl, and M. L. Zheludkevich, “Influence of water purity on the corrosion behavior of mg0.5znx (x=ca, ge) alloys,” *Corrosion Science*, vol. 153, pp. 62–73, jun 2019.
- [142] D. Mei, C. Wang, S. V. Lamaka, and M. L. Zheludkevich, “Clarifying the influence of albumin on the initial stages of magnesium corrosion in hank’s balanced salt solution,” *Journal of Magnesium and Alloys*, vol. 9, pp. 805–817, may 2021.
- [143] D. Höche, “Simulation of corrosion product deposit layer growth on bare magnesium galvanically coupled to aluminum,” *Journal of The Electrochemical Society*, vol. 162, no. 1, pp. C1–C11, 2014.

- [144] B. Zeller-Plumhoff, T. AlBaraghtheh, D. Höche, and R. Willumeit-Römer, “Computational modelling of magnesium degradation in simulated body fluid under physiological conditions,” *Journal of Magnesium and Alloys*, vol. 10, pp. 965–978, apr 2022.
- [145] B. Zeller-Plumhoff, M. Gile, M. Priebe, H. Slominska, B. Boll, B. Wiese, T. Würger, R. Willumeit-Römer, and R. H. Meißner, “Exploring key ionic interactions for magnesium degradation in simulated body fluid – a data-driven approach,” *Corrosion Science*, vol. 182, p. 109272, apr 2021.
- [146] J. Gonzalez, S. V. Lamaka, D. Mei, N. Scharnagl, F. Feyerabend, M. L. Zheludkevich, and R. Willumeit-Römer, “Mg biodegradation mechanism deduced from the local surface environment under simulated physiological conditions,” *Advanced Healthcare Materials*, vol. 10, p. 2100053, may 2021.
- [147] N. Ingri, W. Kakolowicz, L. G. Sillén, and B. Warnqvist, “High-speed computers as a supplement to graphical methods—v1haltafall, a general program for calculating the composition of equilibrium mixtures,” *Talanta*, vol. 14, pp. 1261–1286, nov 1967.
- [148] B. Warnqvist, “The HALTAFALL program-some corrections, and comments on recent experience,” *Talanta*, vol. 18, pp. 457–458, apr 1971.
- [149] G. Eriksson, “An algorithm for the computation of aqueous multi-component, multiphase equilibria,” *Analytica Chimica Acta*, vol. 112, pp. 375–383, dec 1979.
- [150] C. Wang, C. Song, D. Mei, L. Wang, W. Wang, T. Wu, D. Snihirova, M. L. Zheludkevich, and S. V. Lamaka, “Low interfacial pH discloses the favorable biodegradability of several mg alloys,” *Corrosion Science*, vol. 197, p. 110059, apr 2022.
- [151] M. Barzegari and L. Geris, “Highly scalable numerical simulation of coupled reaction–diffusion systems with moving interfaces,” *The International Journal of High Performance Computing Applications*, vol. 36, no. 2, pp. 198–213, 2022.
- [152] D. Mareci, G. Bolat, J. Izquierdo, C. Crimu, C. Munteanu, I. Antoniac, and R. Souto, “Electrochemical characteristics of bioresorbable binary MgCa alloys in ringer's solution: Revealing the impact of local pH distributions during in-vitro dissolution,” *Materials Science and Engineering: C*, vol. 60, pp. 402–410, mar 2016.

- [153] S. Gnedenkov, S. Sinebryukhov, V. Egorkin, D. Mashtalyar, I. Vyaliy, K. Nadaraia, I. Imshinetskiy, A. Nikitin, E. Subbotin, and A. Gnedenkov, “Magnesium fabricated using additive technology: Specificity of corrosion and protection,” *Journal of Alloys and Compounds*, vol. 808, p. 151629, nov 2019.
- [154] U. M. Tefashe, P. Dauphin-Ducharme, M. Danaie, Z. P. Cano, J. R. Kish, G. A. Botton, and J. Mauzeroll, “Localized corrosion behavior of AZ31b magnesium alloy with an electrodeposited poly(3,4-ethylenedioxythiophene) coating,” *Journal of The Electrochemical Society*, vol. 162, no. 10, pp. C536–C544, 2015.
- [155] S. Lamaka, G. Knörnschild, D. Snihirova, M. Taryba, M. Zheludkevich, and M. Ferreira, “Complex anticorrosion coating for ZK30 magnesium alloy,” *Electrochimica Acta*, vol. 55, pp. 131–141, dec 2009.
- [156] C. M. Bidan, K. P. Kommareddy, M. Rumpler, P. Kollmannsberger, Y. J. M. Bréchet, P. Fratzl, and J. W. C. Dunlop, “How linear tension converts to curvature: Geometric control of bone tissue growth,” *PLoS ONE*, vol. 7, p. e36336, may 2012.
- [157] C. M. Bidan, K. P. Kommareddy, M. Rumpler, P. Kollmannsberger, P. Fratzl, and J. W. C. Dunlop, “Geometry as a factor for tissue growth: Towards shape optimization of tissue engineering scaffolds,” *Advanced Healthcare Materials*, vol. 2, pp. 186–194, nov 2012.
- [158] M. Rumpler, A. Woesz, J. W. Dunlop, J. T. van Dongen, and P. Fratzl, “The effect of geometry on three-dimensional tissue growth,” *Journal of The Royal Society Interface*, vol. 5, pp. 1173–1180, mar 2008.
- [159] Y. Sun and C. Beckermann, “Sharp interface tracking using the phase-field equation,” *Journal of Computational Physics*, vol. 220, pp. 626–653, jan 2007.
- [160] S. Osher and J. A. Sethian, “Fronts propagating with curvature-dependent speed: Algorithms based on hamilton-jacobi formulations,” *Journal of Computational Physics*, vol. 79, pp. 12–49, nov 1988.
- [161] A. M. Andrew, “Level set methods and fast marching methods: Evolving interfaces in computational geometry, fluid mechanics, computer vision, and materials science, by j.a. sethian, cambridge university press, cambridge, uk, 2nd edn. 1999 (first published 1996 as level set methods) xviii + 420 pp., isbn (paperback) 0-521-64557-3, (hardback) 0-521-64204-3 (pbk, £18.95),” *Robotica*, vol. 18, p. 89–92, jan 2000.

- [162] W. J. Rider and D. B. Kothe, “Reconstructing volume tracking,” *Journal of Computational Physics*, vol. 141, pp. 112–152, apr 1998.
- [163] W. J. Boettinger, J. A. Warren, C. Beckermann, and A. Karma, “Phase-field simulation of solidification,” *Annual Review of Materials Research*, vol. 32, pp. 163–194, aug 2002.
- [164] I. Bellemans, N. Moelans, and K. Verbeken, “Phase-field modelling in extractive metallurgy,” *Critical Reviews in Solid State and Materials Sciences*, vol. 43, pp. 417–454, dec 2017.
- [165] D. M. Anderson, G. B. McFadden, and A. A. Wheeler, “DIFFUSE-INTERFACE METHODS IN FLUID MECHANICS,” *Annual Review of Fluid Mechanics*, vol. 30, pp. 139–165, jan 1998.
- [166] A. Karma and W.-J. Rappel, “Quantitative phase-field modeling of dendritic growth in two and three dimensions,” *Physical Review E*, vol. 57, pp. 4323–4349, apr 1998.
- [167] L.-Q. Chen, “Phase-field models for microstructure evolution,” *Annual Review of Materials Research*, vol. 32, pp. 113–140, aug 2002.
- [168] L.-Q. Chen and W. Yang, “Computer simulation of the domain dynamics of a quenched system with a large number of nonconserved order parameters: The grain-growth kinetics,” *Physical Review B*, vol. 50, pp. 15752–15756, dec 1994.
- [169] H. Henry and H. Levine, “Dynamic instabilities of fracture under biaxial strain using a phase field model,” *Physical Review Letters*, vol. 93, sep 2004.
- [170] R. Spatschek, E. Brener, and A. Karma, “Phase field modeling of crack propagation,” *Philosophical Magazine*, vol. 91, pp. 75–95, jan 2011.
- [171] D. N. Bhate, A. Kumar, and A. F. Bower, “Diffuse interface model for electromigration and stress voiding,” *Journal of Applied Physics*, vol. 87, pp. 1712–1721, feb 2000.
- [172] W. Mai, S. Soghrati, and R. G. Buchheit, “A phase field model for simulating the pitting corrosion,” *Corrosion Science*, vol. 110, pp. 157–166, sep 2016.
- [173] C. Lin, H. Ruan, and S.-Q. Shi, “Phase field study of mechanico-electrochemical corrosion,” *Electrochimica Acta*, vol. 310, pp. 240–255, jul 2019.

- [174] A. Imanian and M. Amiri, “Phase field modeling of galvanic corrosion,” 2018.
- [175] C. Lin and H. Ruan, “Multi-phase-field modeling of localized corrosion involving galvanic pitting and mechano-electrochemical coupling,” *Corrosion Science*, vol. 177, p. 108900, dec 2020.
- [176] T. Q. Ansari, Z. Xiao, S. Hu, Y. Li, J.-L. Luo, and S.-Q. Shi, “Phase-field model of pitting corrosion kinetics in metallic materials,” *npj Computational Materials*, vol. 4, jul 2018.
- [177] C. Tsuyuki, A. Yamanaka, and Y. Ogimoto, “Phase-field modeling for pH-dependent general and pitting corrosion of iron,” *Scientific Reports*, vol. 8, aug 2018.
- [178] A. F. Chadwick, J. A. Stewart, R. A. Enrique, S. Du, and K. Thornton, “Numerical modeling of localized corrosion using phase-field and smoothed boundary methods,” *Journal of The Electrochemical Society*, vol. 165, no. 10, pp. C633–C646, 2018.
- [179] D. Jeong and J. Kim, “Phase-field model and its splitting numerical scheme for tissue growth,” *Applied Numerical Mathematics*, vol. 117, pp. 22–35, jul 2017.
- [180] H. G. Lee, J. Park, S. Yoon, C. Lee, and J. Kim, “Mathematical model and numerical simulation for tissue growth on bioscaffolds,” *Applied Sciences*, vol. 9, p. 4058, sep 2019.
- [181] C. Beckermann, H.-J. Diepers, I. Steinbach, A. Karma, and X. Tong, “Modeling melt convection in phase-field simulations of solidification,” *Journal of Computational Physics*, vol. 154, pp. 468–496, sep 1999.
- [182] J. Shen, , and X. Y. and, “Numerical approximations of allen-cahn and cahn-hilliard equations,” *Discrete & Continuous Dynamical Systems - A*, vol. 28, no. 4, pp. 1669–1691, 2010.
- [183] H. Abboud, C. A. Koseifi, and J.-P. Chehab, “A stabilized bi-grid method for allen-cahn equation in finite elements,” *Computational and Applied Mathematics*, vol. 38, mar 2019.
- [184] C. M. Elliott, “The cahn-hilliard model for the kinetics of phase separation,” in *Mathematical Models for Phase Change Problems*, pp. 35–73, Birkhäuser Basel, 1989.

- [185] Y. Guyot, I. Papantoniou, Y. C. Chai, S. V. Bael, J. Schrooten, and L. Geris, “A computational model for cell/ECM growth on 3d surfaces using the level set method: a bone tissue engineering case study,” *Biomechanics and Modeling in Mechanobiology*, vol. 13, pp. 1361–1371, apr 2014.
- [186] I. Papantoniou, M. Sonnaert, L. Geris, F. P. Luyten, J. Schrooten, and G. Kerckhofs, “Three-dimensional characterization of tissue-engineered constructs by contrast-enhanced nanofocus computed tomography,” *Tissue Engineering Part C: Methods*, vol. 20, pp. 177–187, mar 2014.
- [187] D. V. hede, B. Liang, S. Anania, M. Barzegari, B. Verlée, G. Nolens, J. Pirson, L. Geris, and F. Lambert, “3d-printed synthetic hydroxyapatite scaffold with in silico optimized macrostructure enhances bone formation in vivo,” *Advanced Functional Materials*, vol. 32, p. 2105002, oct 2021.
- [188] E. M. Darling and F. Guilak, “A neural network model for cell classification based on single-cell biomechanical properties,” *Tissue Engineering Part A*, vol. 14, pp. 1507–1515, sep 2008.
- [189] M. A. Alias and P. R. Buenzli, “Modeling the effect of curvature on the collective behavior of cells growing new tissue,” *Biophysical Journal*, vol. 112, pp. 193–204, jan 2017.
- [190] M. Rubert, J. R. Vetsch, I. Lehtoviita, M. Sommer, F. Zhao, A. R. Studart, R. Müller, and S. Hofmann, “Scaffold pore geometry guides gene regulation and bone-like tissue formation in dynamic cultures,” *Tissue Engineering Part A*, vol. 27, pp. 1192–1204, sep 2021.
- [191] J. P. Long, S. J. Hollister, and S. A. Goldstein, “A paradigm for the development and evaluation of novel implant topologies for bone fixation: In vivo evaluation,” *Journal of Biomechanics*, vol. 45, pp. 2651–2657, oct 2012.
- [192] D. Luo, Q. Rong, and Q. Chen, “Finite-element design and optimization of a three-dimensional tetrahedral porous titanium scaffold for the reconstruction of mandibular defects,” *Medical Engineering & Physics*, vol. 47, pp. 176–183, sep 2017.
- [193] X. Luo, B. Yang, L. Sheng, J. Chen, H. Li, L. Xie, G. Chen, M. Yu, W. Guo, and W. Tian, “CAD based design sensitivity analysis and shape optimization of scaffolds for bio-root regeneration in swine,” *Biomaterials*, vol. 57, pp. 59–72, jul 2015.

- [194] A. Moure and H. Gomez, “Phase-field modeling of individual and collective cell migration,” *Archives of Computational Methods in Engineering*, vol. 28, pp. 311–344, dec 2019.
- [195] A. Moure, *Phase-field modeling and isogeometric analysis of cell crawling*. PhD thesis, Universidade da Coruna, 2017.
- [196] D. P. Byrne, D. Lacroix, J. A. Planell, D. J. Kelly, and P. J. Prendergast, “Simulation of tissue differentiation in a scaffold as a function of porosity, young's modulus and dissolution rate: Application of mechanobiological models in tissue engineering,” *Biomaterials*, vol. 28, pp. 5544–5554, dec 2007.
- [197] A. Carlier, L. Geris, K. Bentley, G. Carmeliet, P. Carmeliet, and H. V. Oosterwyck, “MOSAIC: A multiscale model of osteogenesis and sprouting angiogenesis with lateral inhibition of endothelial cells,” *PLoS Computational Biology*, vol. 8, p. e1002724, oct 2012.
- [198] A. Carlier, G. A. Skvortsov, F. Hafezi, E. Ferraris, J. Patterson, B. Koç, and H. V. Oosterwyck, “Computational model-informed design and bioprinting of cell-patterned constructs for bone tissue engineering,” *Biofabrication*, vol. 8, p. 025009, may 2016.
- [199] A. S. Vagbharathi and S. Gopalakrishnan, “An extended finite-element model coupled with level set method for analysis of growth of corrosion pits in metallic structures,” *Proceedings of the Royal Society A: Mathematical, Physical and Engineering Sciences*, vol. 470, p. 20140001, aug 2014.
- [200] R. Duddu, “Numerical modeling of corrosion pit propagation using the combined extended finite element and level set method,” *Computational Mechanics*, vol. 54, pp. 613–627, apr 2014.
- [201] Z. Xu, H. Huang, X. Li, and P. Meakin, “Phase field and level set methods for modeling solute precipitation and/or dissolution,” *Computer Physics Communications*, vol. 183, pp. 15–19, jan 2012.
- [202] W. Chen and E. D. Schutter, “Parallel STEPS: Large scale stochastic spatial reaction-diffusion simulation with high performance computers,” *Frontiers in Neuroinformatics*, vol. 11, feb 2017.
- [203] S. N. Arjunan, A. Miyauchi, K. Iwamoto, and K. Takahashi, “pSpatioocyte: a high-performance simulator for intracellular reaction-diffusion systems,” *BMC Bioinformatics*, vol. 21, jan 2020.

- [204] M. J. Hallock, J. E. Stone, E. Roberts, C. Fry, and Z. Luthey-Schulten, “Simulation of reaction diffusion processes over biologically relevant size and time scales using multi-GPU workstations,” *Parallel Computing*, vol. 40, pp. 86–99, may 2014.
- [205] B. E. Kendall, C. J. Briggs, W. W. Murdoch, P. Turchin, S. P. Ellner, E. McCauley, R. M. Nisbet, and S. N. Wood, “WHY DO POPULATIONS CYCLE? a SYNTHESIS OF STATISTICAL AND MECHANISTIC MODELING APPROACHES,” *Ecology*, vol. 80, pp. 1789–1805, sep 1999.
- [206] J. Ahrens, B. Geveci, and C. Law, “Paraview: An end-user tool for large data visualization,” *The visualization handbook*, vol. 717, 2005.
- [207] E. Wendland and H. Schulz, “Numerical experiments on mass lumping for the advection-diffusion equation,” *Pesquisa e Tecnologia Minerva*, vol. 2, pp. 227–233, 01 2005.
- [208] M. Badri, P. Jolivet, B. Rousseau, and Y. Favenne, “High performance computation of radiative transfer equation using the finite element method,” *Journal of Computational Physics*, vol. 360, pp. 74–92, may 2018.
- [209] H. A. Daas, L. Grigori, P. Jolivet, and P.-H. Tournier, “A multilevel schwarz preconditioner based on a hierarchy of robust coarse spaces,” 2019.
- [210] V. Dolean, P. Jolivet, and F. Nataf, *An Introduction to Domain Decomposition Methods*. Philadelphia, PA: Society for Industrial and Applied Mathematics, 2015.
- [211] P. R. Amestoy, I. S. Duff, J. Koster, and J.-Y. L’Excellent, “A fully asynchronous multifrontal solver using distributed dynamic scheduling,” *SIAM Journal on Matrix Analysis and Applications*, vol. 23, no. 1, pp. 15–41, 2001.
- [212] Y. Saad, *Iterative Methods for Sparse Linear Systems*. Society for Industrial and Applied Mathematics, jan 2003.
- [213] I. C. F. Ipsen and C. D. Meyer, “The idea behind krylov methods,” *The American Mathematical Monthly*, vol. 105, pp. 889–899, dec 1998.
- [214] M. R. Hestenes, E. Stiefel, *et al.*, “Methods of conjugate gradients for solving linear systems,” *Journal of research of the National Bureau of Standards*, vol. 49, no. 6, pp. 409–436, 1952.

- [215] G. J. Habetler and E. L. Wachspress, “Symmetric successive overrelaxation in solving diffusion difference equations,” *Mathematics of Computation*, pp. 356–362, 1961.
- [216] G. Russo and P. Smereka, “A remark on computing distance functions,” *Journal of Computational Physics*, vol. 163, pp. 51–67, sep 2000.
- [217] J. L. Gustafson, “Reevaluating amdahl’s law,” *Communications of the ACM*, vol. 31, pp. 532–533, may 1988.
- [218] G. M. Amdahl, “Validity of the single processor approach to achieving large scale computing capabilities,” in *Proceedings of the April 18-20, 1967, spring joint computer conference on - AFIPS’ 67 (Spring)*, ACM Press, 1967.
- [219] A. Ghai, C. Lu, and X. Jiao, “A comparison of preconditioned krylov subspace methods for large-scale nonsymmetric linear systems,” *Numerical Linear Algebra with Applications*, vol. 26, p. e2215, oct 2018.
- [220] A. M. Hassan and M. El-Shenawee, “Parallel implementation of the diffusion–drift algorithm for modeling the electrophysiological activity of breast tumors,” *Journal of Parallel and Distributed Computing*, vol. 71, pp. 1011–1023, jul 2011.
- [221] C. Rettinger, C. Godenschwager, S. Eibl, T. Preclik, T. Schruff, R. Frings, and U. Rüde, “Fully resolved simulations of dune formation in riverbeds,” in *High Performance Computing* (J. M. Kunkel, R. Yokota, P. Balaji, and D. Keyes, eds.), (Cham), pp. 3–21, Springer International Publishing, 2017.